

I. Quantum-Mechanical Chemical Exchange

II. NMR of Semiconductors

Thesis by

Narayanan Damodaran Kurur

In Partial Fulfillment of the Requirements

for the Degree of

Doctor of Philosophy

California Institute of Technology

Pasadena, California

1992

(Submitted March 27, 1992)

## Acknowledgements

The successful completion of this dissertation was aided in no small measure by the help I received from a number of people. First and foremost, I should thank the members of the Weitekamp group who have contributed immeasurably, scientifically and otherwise, during my stay at Caltech. In particular, I benefited immensely from the collaborations with both Steve Buratto and Dan Jones. Dr. Herman Cho was always willing to clear my many misconceptions regarding my work. Paul Carson, John Marohn, and Pedro Pizarro deserve a special word of thanks for meticulously proofreading this thesis.

The work presented here would not have been possible if not for my thesis adviser Professor Dan Weitekamp. He has been extremely supportive, has shown undeserving patience with me, and has often pointed me in the right direction.

A word of thanks to the Zewail group who accepted me as a social member and exposed me to big Wednesdays, beach trips, strawberry donuts, etc.

Thanks are also due to my roommates at various times: Jashojiban Banik, Jack Breen, Balu Nadiga, Glenn Soberman, Jim Spotts, and Gautam Vasisht. In particular, I would like to take this opportunity to wish Jack the very best as he gets ready to start his new job.

Last, but not the least, let me thank my family for supporting me every step of the way.

## Abstract

### Part I. Quantum-Mechanical Chemical Exchange

The requirement that the total wavefunction of a system be antisymmetric to the exchange of identical fermions manifests itself as a scalar coupling between the spin angular momenta. In a class of transition metal trihydrides, this effect is observed as multiplet structure in the liquid state NMR spectrum due to proton tunnelling. Numerical fits to the temperature dependence of these couplings are described as the ensemble averaged tunnel splitting over thermally occupied rovibrational states. The accepted concept of stochastic average of the coupling is questioned on theoretical grounds and an alternative prescription given which differs significantly in its numerical predictions. It is also shown how the fluctuations of the tunnel splitting due to dissipative coupling to the lattice contribute to the chemical rate processes that incoherently exchange nuclei between different sites and the coherent exchange effect. A master equation procedure for evaluating such rates numerically is presented.

### Part II. NMR of Semiconductors

NMR is an inherently low-sensitive technique. Moreover, unless special procedures are employed the structural information obtainable from an NMR line in the solid-state is also limited. Both these problems are addressed here. A method is proposed for the high-resolution solid-state NMR of nuclei around paramagnetic defects which uses multiple-pulse techniques to selectively average spin couplings and extract structural information. It is shown by numerical simulations how the method could resolve a long-standing con-

troversy on the assignment of hyperfine tensors to silicon sites around a phosphorous dopant. Experimental results on a novel time-domain optical nuclear magnetic resonance method are obtained on gallium arsenide. Comparison with an earlier continuous-wave variant of the technique show improved absolute sensitivity and relative sensitivity to low-abundance sites near an optically relevant defect.

# Contents

<b>Acknowledgements</b>	<b>ii</b>
<b>Abstract</b>	<b>iii</b>
<b>I Quantum-Mechanical Chemical Exchange</b>	<b>1</b>
<b>Chapter 1 Introduction</b>	<b>2</b>
1.1 Outline . . . . .	2
<b>Chapter 2 Transition Metal Trihydrides, Exchange, and Tunnelling: An Overview</b>	<b>4</b>
2.1 Transition Metal Trihydrides . . . . .	4
2.2 The Symmetrisation Postulate and Exchange . . . . .	9
2.3 Quantum-Mechanical Tunnelling . . . . .	15
2.4 References . . . . .	20
<b>Chapter 3 Scalar Coupling in Transition Metal Trihydrides</b>	<b>24</b>
3.1 The Hamiltonian . . . . .	25
3.2 Average Tunnel Splitting . . . . .	28
3.3 Spatial Models . . . . .	30
3.4 Determination of Tunnel Splitting . . . . .	32
3.5 Fitting Procedure . . . . .	34
3.6 Fits to Experimental Data . . . . .	35

3.7	Comparison with Other Approaches . . . . .	39
3.8	New Averaging Procedure . . . . .	41
3.9	Trihydride $\rightleftharpoons$ Dihydrogen Complex Equilibrium . . . . .	43
3.10	Summary . . . . .	45
3.11	References . . . . .	48
<b>Chapter 4 Lineshapes in Transition Metal Trihydrides</b>		<b>50</b>
4.1	The System . . . . .	51
4.2	Relaxation Due to Fluctuating Scalar Coupling . . . . .	53
4.3	Master Equation . . . . .	56
4.4	Discussion . . . . .	59
4.5	Conclusions . . . . .	64
4.6	References . . . . .	65
<b>II NMR of Semiconductors</b>		<b>67</b>
<b>Chapter 5 Introduction</b>		<b>68</b>
5.1	Outline . . . . .	68
<b>Chapter 6 Resolution-Enhanced Electron Nuclear Double Resonance</b>		<b>70</b>
6.1	Electron Nuclear Double Resonance . . . . .	71
6.2	Resolution-Enhanced ENDOR (RE-ENDOR) . . . . .	74
6.3	Isolating Couplings . . . . .	80
6.4	Results and Discussion . . . . .	81
6.5	Numerical Calculations . . . . .	85
6.6	Conclusions . . . . .	88
6.7	References . . . . .	91

<b>Chapter 7</b>	<b>Fourier Transform Time Sequenced Optical Nuclear Magnetic Resonance: Preliminary Studies</b>	<b>93</b>
7.1	Optically Detected NMR in III-V Semiconductors . . . . .	94
7.2	Steady-State ODNMR . . . . .	99
7.3	Time-Sequenced Optical NMR Experiment . . . . .	102
7.4	Time-Domain TSONMR . . . . .	104
7.5	Conclusions . . . . .	116
7.6	References . . . . .	119
<b>Appendix A</b>	<b>Second-Order Effects in Electron Nuclear Double Resonance</b>	<b>122</b>
A.1	Essentials of Coherent Averaging Theory . . . . .	123
A.2	Outline of the Calculation . . . . .	124
A.3	References . . . . .	130
<b>Appendix B</b>	<b>Noise in the Optical NMR Instrument Detection Circuit</b>	<b>131</b>
B.1	The Equivalent Circuit . . . . .	131
B.2	Noise Measurements . . . . .	132
B.3	Calculated Noise . . . . .	134
B.4	References . . . . .	137
<b>Appendix C</b>	<b>Simulation of Multiple Pulse NMR Experiments</b>	<b>138</b>
C.1	Introduction . . . . .	139
C.2	Program Specifics . . . . .	140
C.3	References . . . . .	144
<b>Appendix D</b>	<b>Solution of One-Dimensional Schrödinger Equations</b>	<b>145</b>
D.1	Algorithm for the Linear Case . . . . .	146
D.2	Periodic Potential . . . . .	149
D.3	References . . . . .	150

## List of Figures

2.1	Two coupled spins undergoing two site exchange . . . . .	14
2.2	Energy levels of a symmetric double-well . . . . .	18
3.1	Theoretical fits of published $J(T)$ data I . . . . .	36
3.2	Theoretical fits of published $J(T)$ data II . . . . .	37
3.3	Trends in the average exchange coupling for the hindered rotor and double-well . . . . .	42
3.4	Trihydride $\rightleftharpoons$ Dihydrogen complex equilibria I . . . . .	44
3.5	Trihydride $\rightleftharpoons$ Dihydrogen complex equilibria II . . . . .	46
4.1	Temperature dependent lineshapes observed in $\text{Cp}^*\text{RuH}_3\text{P}(\text{iPr})_3$ . . . . .	60
4.2	Fit to the experimentally observed chemical exchange rate and the $J$ -coupling in $\text{Cp}^*\text{RuH}_3\text{P}(\text{iPr})_3$ . . . . .	63
6.1	Energy levels for ENDOR . . . . .	72
6.2	RE-ENDOR timing diagram and evolution period sequences . . . . .	76
6.3	Unit cell of silicon . . . . .	83
6.4	RE-ENDOR spectrum of D line in silicon . . . . .	87
6.5	Rf Power dependence of the homonuclear decoupling sequences . . . . .	89
7.1	GaAs band structure and optical selection rules . . . . .	95
7.2	Experimental setup for optically detected NMR . . . . .	98
7.3	Hanle effect detection . . . . .	100

7.4	Timing diagram and vector picture for time- sequenced optical NMR . . .	103
7.5	Optically detected transient nutations . . . . .	107
7.6	Optically detected two-pulse FID . . . . .	109
7.7	Comparison of steady-state ODNMR and Fourier Transform TSONMR. .	110
7.8	CW $T_1$ measurements for $^{71}\text{Ga}$ . . . . .	113
7.9	Linewidth for the CW, FT, and FT with nuclear polarisation and spin diffusion periods. . . . .	115
7.10	Spin-echo amplitudes for $^{71}\text{Ga}$ . . . . .	117

**Part I**

**Quantum-Mechanical Chemical Exchange**

## Chapter 1

# Introduction

The symmetrisation postulate of quantum mechanics restricts the physically allowed states for a system of identical particles. In fermions this restriction results in the “exchange effect” which is a coupling between the spins when two or more particles trade places. It has long been implicated in the NMR of solid  $^3\text{He}$  and low temperature methyl groups where the small mass of the particles results in a measurable probability of ground state tunnelling in coordinates which exchange particle positions.

It has now been convincingly shown that in a large class of transition metal polyhydrides, anomalous liquid-state NMR properties arise from exchange coupling due to proton tunnelling. The research presented in this part of the dissertation is an attempt to provide a unified quantitative description of the static and dynamic spectroscopic properties of these complexes.

### 1.1 Outline

In Chapter 2 the concepts that form the foundation for this part of the dissertation are presented. This chapter starts with a brief discussion of transition metal polyhydrides and their spectroscopic properties. The evidence that these compounds exhibit exchange tunnelling is presented. Also introduced in this chapter are the symmetrisation postulate and the exchange effect. The extraction of kinetic parameters of chemical exchange from temperature dependent NMR spectra is highlighted. A discussion of quantum-mechanical tunnelling concludes the chapter.

The magnitude of the scalar coupling seen in transition metal trihydrides and its strong dependence on temperature are the focal points of Chapter 3. An averaging of the tunnel splitting over a number of rovibrational states provides the exchange contribution to the measured coupling. The traditional averaging procedure is called into question on theoretical grounds and an alternative stochastic average is presented briefly. If proven experimentally to be correct, it results in a profound revision of previous interpretations which has only barely begun. With either averaging procedure, the temperature dependence of the coupling constants follows from the temperature dependence of the Boltzmann weights in a sum over rovibrational states. The procedure adopted here for numerical examples is to reduce the problem to the case of two particles tunnelling in one dimension and to solve the resultant one-dimensional Schrödinger equation numerically for its eigenvalues. This reduction makes getting a solution to the problem of two particles tunnelling tractable numerically and still manages to retain the essential physics.

The last chapter in this Part is dedicated to understanding the dynamic aspects of the trihydride problem. The intention of this study was to understand the temperature dependent lineshapes in these transition metal trihydrides using the spatial model presented in Chapter 3 and avoiding the use of the usual phenomenological concepts of chemical exchange. The dynamics in this model arise as a result of fluctuations in the exchange coupling due to rovibrational relaxation. This differs qualitatively from previous conceptions of the connection between tunnelling and chemical exchange. It can be shown by a Redfield analysis that in this model the chemical exchange rate is the low-frequency Fourier component of the autocorrelation function of the  $J$  coupling. In this chapter a master equation method is presented for determining the autocorrelation function given a model of the rovibrational population dynamics.

## Chapter 2

# Transition Metal Trihydrides, Exchange, and Tunnelling: An Overview

This chapter begins with a discussion of some of the anomalous NMR properties of a class of transition metal polyhydrides that instigated the investigation reported in this part of the dissertation. The experiments and the arguments are presented that led to the present rationale that the peculiar NMR behaviour of these compounds is a result of “exchange tunnelling.” The rest of the chapter is therefore devoted to introducing the exchange effect and quantum-mechanical tunnelling.

### 2.1 Transition Metal Trihydrides

The activation of hydrogen by metal centers is important in catalysis from both commercial and scientific standpoints[1] and has led to the study of the structure and reactivity of transition metal polyhydride complexes. Another reason for the interest in these complexes is their high reactivity toward hydrocarbons, making them good precursors for C-H activation reactions.[2]

Although this part of the dissertation is concerned with the quantum aspects of what have been considered to be classical trihydrides, a brief historical perspective of “non-classical” polyhydrides is presented here for completeness. In 1980, Kubas[3] isolated a dihydrogen complex (notice that complexes containing intact  $H_2$  are referred to as dihydrogen complexes and are distinct from those that contain two H ligands, the dihydrides)

of molybdenum of the form  $\text{Mo}(\text{CO})_3(\text{PR}_3)_2\text{H}_2$  where the H-H bond was intact. The solid-state structure of the dihydrogen molybdenum compound was determined by neutron diffraction and revealed that the hydrogen exists as intact dihydrogen and that the H-H bond is longer and weaker than in free  $\text{H}_2$ . Since then a number of dihydrogen complexes and polyhydrides containing both dihydrogen and hydride as ligands have been isolated.[4] In all these compounds, the  $\text{H}_2$  is "sidebound" ( $\eta^2 - \text{H}_2$ ) and behaves as a weak donor ligand. The dihydrogen can undergo hindered rotation (similar to that seen in methyl groups) as has been revealed from inelastic neutron scattering studies.[5, 6, 7] Recently, by measuring the temperature dependence of the spin lattice relaxation time,  $T_1$ , some of the purported classical dihydrides have been reinterpreted as "nonclassical" dihydrogen complexes.[1, 8] Since the  $T_1$  is often dominated by dipole-dipole contributions (a strongly distance dependent quantity) the  $T_1$  of the dihydrogen complexes is shorter than in the corresponding classical dihydrides. NMR studies have revealed that in some cases the dihydrogen complex is in equilibrium with the classical dihydride.[9, 10]

The interesting properties exhibited by the dihydrogen complexes prompted a molecular orbital study by Burdett and coworkers[11, 12] that was aimed at determining the relative electronic stability of metal-polyhydrogen and -polyhydride complexes. Their study pointed to a number of electronic considerations that may be important to stabilising polyhydrogen ligands when coordinated to transition metals. In all the cases a competition between the polyhydride and the polyhydrogen complexes was observed with the polyhydrogen units existing in either the open or closed forms. Isolation of a coordinated  $\text{H}_3$  moiety was, according to them, an important step towards the understanding of polyhydrogen transition metal complexes.

Almost simultaneously with this theoretical study of Burdett and coworkers, the first report of an isolable ruthenium complex containing the  $\text{H}_3$  moiety,  $(\text{C}_5\text{Me}_5)\text{RuPMe}_3\text{H}_3$ , appeared [13, 14, 15, 16, 17] which exhibited some anomalous NMR properties. Attempts

were made to explain, albeit unsuccessfully, the unusual NMR spectra as due to indirect scalar couplings resulting from bonds between the protons.[15, 18, 19] However, it was recently shown by Jones *et al.*[20] and independently by Zilm *et al.* [21] that these properties could be unequivocally attributed to exchange coupling due to proton tunnelling.

Since then a number of trihydrides of other metals have also been isolated [22, 23, 24] which exhibit similar behaviour. The study reported in this dissertation was aimed at trying to understand the anomalous NMR properties of these trihydrides which are discussed next. The details regarding the synthesis, electronic structure, reactivity etc. are not critical to this dissertation and can be found in a number of publications. [16, 17, 22, 23, 24]

In this discussion attention is focussed on the liquid-state NMR spectrum of these complexes assigned to the hydride protons since they show some extraordinary properties. The three protons form an  $AB_2$  spin system with anomalously large  $J$  coupling between the  $A$  and  $B$  spins which increases rapidly with temperature. A sampling of the compounds that show these interesting properties can be found in Table 2.1. The next chapter is concerned with quantitatively explaining the size of the coupling and its temperature dependence, while the last chapter in this part will be concerned with the lineshapes seen in these systems.

The first noteworthy property is the magnitude of the scalar coupling, which ranges from 10's to 100's of Hz. Table 2.1 shows the variation in the  $J$  coupling as a function of the temperature for the compounds where this data is available in the literature. In one compound,  $(\eta - C_5H_5)Ir(MPTB)H_3$ , for example, a  $J_{AB}$  as high as 1500Hz has been observed. That these values are abnormal is exemplified when contrasted with the  $J$  coupling in free  $H_2$ , which is known to be  $\approx 280$ Hz. (This value is obtained by scaling the  $J$  coupling measured in HD by the ratio of the magnetogyric ratios of proton and deuteron). If the operative mechanism responsible for the  $J$  coupling remained the usual

Table 2.1: Some transition metal trihydrides that show interesting NMR properties.

Compound	Temperature	$J$ Coupling	Reference
$(\eta - C_5Me_5)Ru(P^iPr_3)H_3$	168–203	57–131	[16]
$(\eta - C_5Me_5)Ru(PCy_3)H_3$	178–193	61.7–93.5	[16]
$(\eta - C_5H_5)Ir(PMe_3)H_3$	176–196	96–135	[22]
$(\eta - C_5H_5)Ir(PPh_3)H_3$	176–196	260–397	[22]
$(\eta - C_5H_5)Ir(PCy_3)H_3$	176–196	61–77	[22]
$(\eta - C_5H_5)Ir(P^iPr_3)H_3$	176–196	63.5–75	[22]
$(\eta - C_5H_5)Ir(PMe_2Ph)H_3$	176–196	161–237	[22]
$(\eta - C_5H_5)Ir(POPh_3)H_3$	176–196	358–526	[22]
$(\eta - C_5H_5)Ir(MPTB)H_3$	176–196	972–1565	[22]
$(\eta - C_5H_5)Ir(AsPh_3)H_3$	176–196	376–570	[22]
$(\eta - C_5H_5)Ir(SbPh_3)H_3$	176–196	147–196	[22]
$(\eta - C_5H_5)_2Nb(PCy_3)H_3$	243–303	3–13	[23]
$(\eta - C_6H_6)Os(PCy_3)H_3^+$	163–173	70–89	[24]
$(\eta - C_6H_6)Os(PPh_3)H_3^+$	153–173	219–374	[24]
$(\eta - C_6H_6)Os(MPTB)H_3^+$	153–173	186–368	[24]

electron-mediated indirect through-bond coupling, then the observation of anomalously large  $J$  couplings could only be rationalised by invoking an unusual electronic structure for the complex.[15, 18, 16, 19] This model fails to give even a qualitative explanation for the temperature dependence of the coupling. In this model the observed temperature dependence of the  $J$  coupling could only occur as a result of an equilibrium with other structures. This would require that the chemical shifts of these species also show a temperature dependence, in contradiction of the data.[14, 15, 18, 21, 25, 26, 27] These observations hence point to an unusual mechanism for the origin of this anomalous scalar

coupling.

Isotopic substitution experiments provide more evidence against the case that the results are simply an extreme case of electron-mediated coupling. Any such model for the anomalous  $J$  coupling would predict a  $J_{HD}$  coupling when one of the protons is substituted by deuterium to be

$$J_{HD} \approx \frac{\gamma_D}{\gamma_H} J_{HH}. \quad (2.1)$$

In practice, isotopic substitution leads to vanishingly small  $J_{AB}$  couplings.[14, 19, 21] Based on the above mentioned evidence Jones *et al.* [20, 28] concluded that a scalar coupling mechanism similar to that operative in the quantum crystals  $^3\text{He}$  and  $\text{H}_2$  or in rotating methyl groups at low temperatures must be operative in this case. In these cases the nuclei are known to be “exchange coupled” as a result of tunnelling. The same explanation of anomalous  $J$  couplings in these transition metal trihydrides was also arrived at independently by Zilm and coworkers.[21, 29, 30]

The discussion thus far has only shown that exchange tunnelling could be the operative  $J$  coupling mechanism in the compounds of interest. In the trihydrides, cyclic exchange of the three protons, similar to methyl groups undergoing rotational tunnelling, is also possible. This process, if in effect, would contribute equally to all the scalar couplings, but  $J_{BB}$  would be unobservable due to the magnetic equivalence of the two  $B$  protons. That the exchange is pairwise and not cyclic was deduced [20] from an interpretation of two isotopic substitution experiments of the Yale group.[22] If cyclic exchange were important, substitution of one of the  $B$  spins by deuterium would lead to an  $ABX$  system, with an associated reduction in the measured coupling. On the contrary, upon performing this experiment, a slightly increased  $J_{AB}$  coupling is observed which indicates a predominance of pairwise exchange. The predominance of pairwise exchange was confirmed in another experiment where the compound  $[(\text{C}_5\text{H}_5)\text{IrLH}_3]^+$  was synthesised with a chiral ligand  $L$ . This results in a reduction of the prevailing symmetry and transforms the  $AB_2$  system to

an  $ABC$  spin system. In this compound, while  $J_{AB}$  and  $J_{AC}$  are large and temperature dependent,  $J_{BC}$  is small and shows no temperature dependence. If cyclic exchange were indeed present,  $J_{BC}$  would also be strongly temperature dependent.

The interpretation of the isotopic labelling experiments mentioned thus far has unequivocally confirmed the mechanism for the scalar coupling in the trihydrides to be due to pairwise exchange tunnelling. The sections that follow therefore introduce the symmetrisation postulate, which is responsible for quantum-mechanical tunnelling appearing as an NMR scalar coupling.

## 2.2 The Symmetrisation Postulate and Exchange

### 2.2.1 Symmetrisation Postulate of Quantum Mechanics

According to the symmetrisation postulate of quantum mechanics, the states of a system are symmetric with respect to pairwise exchange of bosons and antisymmetric with respect to exchange of fermions. Particles with integer spin are called bosons; those with half integer spin are fermions. As opposed to other symmetry operations, which lead to optional simplifications, the symmetrisation postulate has to be rigorously imposed. States that have the wrong symmetry must be excluded. This is done in electronic structure calculations, for example, by using Slater determinants as wavefunctions. Most NMR phenomena, however, can be successfully understood without the use of the symmetrisation postulate since the spatial wavefunctions corresponding to the different spin sites are essentially nonoverlapping. In this case the fiction of associating particular particle labels with particular site labels succeeds.

The symmetrisation postulate has been applied in unrelated work in this laboratory to develop new NMR techniques that serve as unique high sensitivity probes for structure and reactivity. The common feature in these techniques is the use of the spin order present in parahydrogen due to the symmetrisation postulate to create nonequilibrium nuclear

spin order. More details about these techniques can be found in a recent thesis.[31]

### 2.2.2 Exchange Effect

The lifting of the  $2^N$ -fold degeneracy, due to  $N$  identical spin-1/2 particles with spatial overlap, is called the “exchange effect.” This phenomenon has been detected in low-temperature solids like  $^3\text{He}$  and  $\text{H}_2$  [34, 35, 36] where the resonance line has more of the characteristics of a liquid than of a solid. This is due to the large zero-point motion that these particles undergo which has the effect of switching the positions of the atoms on neighbouring lattice points.

Consider the case of  $N$  identical particles assigned to  $N$  different sites. The  $N!$  possible permutations can be considered as cavities in the  $3N$ -dimensional configuration space. The exchange can then be viewed as the tunnelling event through the ducts which connects these cavities.[37] The derivation involves calculating the energy splitting in a two-state system formed by one configuration of particles and the permuted version of that configuration. If the wavefunction corresponding to one configuration is  $\Psi_0$ , then the wavefunction of the permuted system is  $P^R\Psi_0$  where  $P^R$  is the operator that permutes two particles. The eigenfunctions are then given by the symmetric and antisymmetric linear combinations of these two wavefunctions, i. e.,

$$\Psi_{\pm} = \frac{1}{\sqrt{2}}(\Psi_0 \pm P^R\Psi_0). \quad (2.2)$$

Defining the exchange operator corresponding to the permutation type  $P^R$  as

$$\bar{P}^R = (P^R + P^{R\dagger}), \quad (2.3)$$

where  $P^{R\dagger}$  is the inverse permutation. With the two state approximation this is formalized by the relations

$$P^R P^R \Psi_0 = 0 \quad (2.4)$$

$$P^{R\dagger} \Psi_0 = 0 \quad (2.5)$$

$$P^{R\dagger} P^R \Psi_0 = \Psi_0 \quad (2.6)$$

it can be seen that

$$\bar{P}^R \Psi_{\pm} = \pm \Psi_{\pm}. \quad (2.7)$$

If  $J(P)$  is the shift in the energy from the non-exchanging system, then  $2J(P)$  is the energy separation between the symmetric ( $E_+$ ) and antisymmetric ( $E_-$ ) states, i. e.,

$$2J(P) = E_+ - E_-.$$

The general form of the effective exchange Hamiltonian is then given as a sum over all permutation types  $P$  and has the form

$$H_{\text{exchange}} = - \sum_P J(P) \bar{P}^R, \quad (2.8)$$

where the negative sign is a result of the fact that the spatially symmetric nodeless wavefunction has the lowest energy. For consistency with the usual NMR conventions, this tunnel splitting will be represented as  $-J^e$  in the rest of this dissertation rather than  $2J$  as is done in the  $^3\text{He}$  literature. For two particles, the exchange Hamiltonian reduces to one term.

Dirac[32] first pointed out that, due to the symmetrisation postulate requiring the total wavefunction to be antisymmetric under an odd permutation of spin and space for a system of identical fermions, the exchange Hamiltonian can be expressed in a form where it acts only on the spin variables. This implies that any permutation consisting of an interchange of electron or nuclear coordinates can be expressed as an algebraic function of the spin. A more general mathematical representation of this statement is

$$\bar{P}^R = (-1)^p P^\sigma, \quad (2.9)$$

where  $P^\sigma$  is the spin permutation operator and  $p$  is the parity of the exchange. Dirac, and later Van Vleck [33], also showed that the spin permutation operator,  $P^\sigma$ , is

$$P^\sigma = \frac{1}{2} + 2\mathbf{S}_1 \cdot \mathbf{S}_2, \quad (2.10)$$

where the  $S$ 's are the spin angular momenta of the two particles that are permuted. Equation (2.10) shows that two indistinguishable particles behave as though there were a direct coupling between them, because the exclusion principle requires one type of spatial solution when the spins are parallel and another when the spins are antiparallel. This direct coupling has the form of a scalar product of the spin angular momentum.

### 2.2.3 Chemical Exchange

In the transition metal trihydrides there is evidence for both resolved tunnel splittings and chemical exchange. In the usual NMR terminology, chemical exchange, refers to any reversible process that interconverts "molecular configurations" on the time scale of the NMR experiment. A more precise operational definition will be given in Chapter 4 in terms of the relaxation superoperator. In this respect, it is different from the quantum-mechanical exchange discussed in the last subsection. The usual notion of chemical exchange is mentioned here to contrast it with quantum treatment developed in Chapter 4 for systems, like the transition metal trihydrides, where both resolved tunnelling splittings and chemical exchange are evident in their lineshapes and the usual notion of molecular configurations must be replaced by properly antisymmetrised delocalised states.

NMR spectroscopy has been used extensively in the study of certain types of dynamic equilibria involving chemical processes, such as internal rotations, chemical reactions, bond isomerisations, etc.[38, 39, 40] All of these processes involve exchange of nuclei between distinct sites, causing characteristic changes in the magnetic resonance spectrum. The NMR spectrum depends critically on the rate of the process causing the site exchange. An example of the observed effect is shown in a computer generated set of spectra in Figure 2.1. This is an example of an  $AB$  spin system (parameters are given in the caption) undergoing mutual exchange; i. e., the two magnetically inequivalent sites involved are interchanged. Two extremes can be readily distinguished in this example. When the exchange rate is slower than the NMR time scale, as is the case in the lowest spectrum

in the stack, then the NMR spectrum obtained is a superposition of the sub-spectra due to the different species present. At the other extreme (top of the stacked plot) is the case when the exchange rate is faster than the NMR time scale, the fast exchange limit. In this regime the observed spectrum can be considered as arising from one species whose NMR parameters are the weighted average of the individual species. The usual prescription for calculating such averages has come under close scrutiny as discussed in Section 3.2.

The first theoretical treatment of dynamic NMR was formulated by Gutowsky, McCall and Slichter [41] and was only applicable to non-coupled spins. It was based on the McConnell equations,[42] which are classical Bloch equations, modified to describe the exchange. For coupled spin systems a more sophisticated quantum-mechanical treatment involving the use of the density matrix formulation is required.[43, 44, 45, 46] The density matrix approach to treating dynamic NMR has been presented in a form suitable for computer calculations (used in calculating the spectra in Figure 2.1).[47]

One of the advantages of NMR is that kinetic information can be obtained from studies of chemical equilibrium.[49] If the examination is restricted to coalescence data, then simplified expressions relating the rate constant at the coalescence temperature to the chemical shift difference and the coupling constant may be used to obtain kinetic data. This method is, however, prone to error and is only applicable to exchange between equally populated sites in an uncoupled system or to an  $AB$  system in which the nuclei undergo mutual exchange between the  $A$  and  $B$  environments. In principle, the NMR lineshapes provide kinetic information on the site exchange processes. This usually involves the use of computer programs, [48] based on one of the methods briefly mentioned earlier, to fit the observed lineshapes. Variation of the lifetimes, and hence of the lineshapes, can be obtained by changing the pH, temperature, catalyst concentrations, etc., leading to more reliable kinetic parameters. The NMR-derived rates are interpreted in terms of energy barriers to the chemical exchange process by the use of the Arrhenius

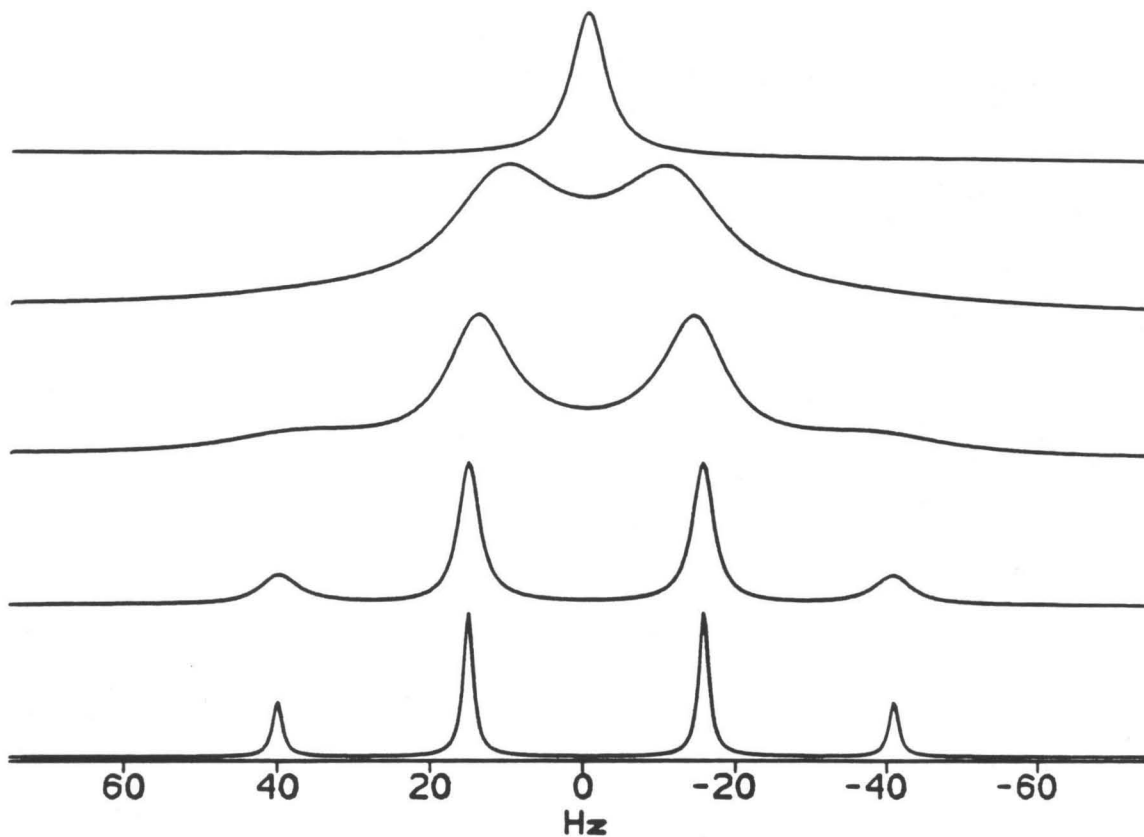


**Figure 2.1:** Computer generated spectra of an  $AB$  system undergoing two site mutual exchange.  $(\nu_A - \nu_B) = 50$  Hz,  $J_{AB} = 25$  Hz. The rate constants are 0.0, 10.0, 50.0, 100.0, and 1000.0 Hz from the bottom to the top of the stack. Spectra were calculated with a computer program [47] that employs density matrix methods.

equation

$$k_e = A \exp\left(-\frac{E_a}{RT}\right). \quad (2.11)$$

Barriers in the approximate range of 20 to 100 kJ/mol can be studied by NMR methods. It is also customary to discuss reactions in terms of transition state theory of reaction rates as summarised by the Eyring equation:

$$k_e = \frac{kT}{h} \exp\left(-\frac{\Delta H^\ddagger}{RT}\right) \exp\left(\frac{\Delta S^\ddagger}{R}\right), \quad (2.12)$$

where  $k$  and  $h$  are, respectively, the Boltzmann and Planck's constant and  $\Delta H^\ddagger$  and  $\Delta S^\ddagger$  are the enthalpy and entropy of activation, which give the difference of the appropriate thermodynamic functions between the initial and the transition state. A plot of  $\ln(k_e/T)$  vs.  $1/T$  yields values for both  $\Delta H^\ddagger$  and  $\Delta S^\ddagger$ .

In the literature on site exchange effects, concepts such as average residence times and molecular configurations are frequently encountered. These concepts do not have a rigorous quantum-mechanical basis. A theory [50] for treating such systems self-consistently will be presented in Chapter 4.

### 2.3 Quantum-Mechanical Tunnelling

Tunnelling [51, 52, 53, 54, 55] is an inherently quantum-mechanical phenomenon. It involves propagation of a particle or a system from one classically accessible region to another through a classically inaccessible region. Interest in tunnelling *per se* has increased in recent years due to its many new applications, especially in the fields of semiconductor heterostructures, quantum well devices, and scanning tunnelling microscopy. The applicability of quantum concepts to macroscopic systems is also of considerable interest. Thus the effect of dissipation, a characteristic of macroscopic systems, on tunnelling has an added significance. In this regard the tunnelling of magnetic flux in superconducting quantum interference devices (SQUID)[56] has been intensively studied.

There are mainly three kinds of barrier tunnelling problems that one usually encounters. They are free-free, bound-free, and bound-bound tunnelling, where the bound and free indicate whether or not potential energy minima are present on either side of the barrier. In this dissertation we will only concern ourselves with bound-bound tunnelling and use one-dimensional models for explicit calculations. The usual justification for the use of one-dimensional models is that most of the concepts can be qualitatively understood with such models. The other reason is the relative ease with which numerical computations on a one-dimensional model can be performed compared to computation for a multi-dimensional case.

A two level system serves as an example to demonstrate some of the general concepts of tunnelling. Consider two states corresponding to ground states of systems infinitely separated, with Hamiltonians  $\mathcal{H}_I$  and  $\mathcal{H}_{II}$ , respectively, with the two levels of equal energy  $E_0$  (this condition can be easily relaxed). The Hamiltonian and the energy for this system are

$$\mathcal{H} = \mathcal{H}_I + \mathcal{H}_{II} \quad (2.13)$$

$$E = E_0 + E_0. \quad (2.14)$$

If the two systems are now brought together the Hamiltonian of the system is

$$\mathcal{H} = \mathcal{H}_I + \mathcal{H}_{II} + \mathcal{H}_{\text{int}}, \quad (2.15)$$

where the last term arises as a result of interaction between the two systems. This Hamiltonian can be represented in the separated system basis and has the form

$$\begin{pmatrix} E_0 & T \\ T & E_0 \end{pmatrix}$$

where T is given by

$$\langle \psi_I | \mathcal{H}_{\text{int}} | \psi_{II} \rangle = T = \langle \psi_{II} | \mathcal{H}_{\text{int}} | \psi_I \rangle. \quad (2.16)$$

The wavefunctions of the two systems that interact are denoted by  $\psi_I$  and  $\psi_{II}$  respectively. The eigenvalues of the Hamiltonian are  $E_0 \pm T$  with the eigenfunctions being  $\frac{1}{\sqrt{2}}(\psi_I \mp \psi_{II})$ .

This simple analysis shows that degenerate levels split into two as a result of tunnelling. This splitting is called the “tunnel splitting.” The eigenfunctions are symmetric or antisymmetric linear combinations of the wavefunctions in each well. For one-dimensional linear problems in the WKB approximation, the  $T$  in the Hamiltonian matrix can be related to the transmission amplitude

$$T = \exp\left(-\frac{1}{\hbar} \int_{x_1}^{x_2} \sqrt{2m(V(x) - E)} dx\right), \quad (2.17)$$

where  $x_1$  and  $x_2$  are the classical turning points.<sup>1</sup>

The above analysis was restricted to two degenerate levels but can be extended to treat the more general case of many levels. The features are presented in Figure 2.2, which is the energy level diagram of a symmetric double-well system. Similar potentials are used extensively in Chapter 3 and in other examples of chemistry and spectroscopy. For example, tunnel splittings are observed in the rotational spectrum of ammonia as a result of umbrella inversion; the two wells in this case would correspond to the two equilibrium positions of the plane formed by the three hydrogens with respect to the nitrogen. For any symmetric double well the eigenvalues cluster in pairs like the pairs of the two level system considered above. The eigenfunctions in each doublet also behave in a similar fashion to the two-level case with one being a symmetric function and the other an antisymmetric function. The tunnel splittings increase with increasing rovibrational quantum number. This is rationalised qualitatively on the grounds that as one goes up the barrier, tunnelling increases since the effective barrier height and width decreases.

In the two-level case the tunnel splitting also determines the temporal evolution of

---

<sup>1</sup>“Every child knows that the amplitude for transmission obeys the WKB formula”-S. Coleman in *The Whys of Subnuclear Physics*, ed. A. Zichichi, New York: Plenum, 1979

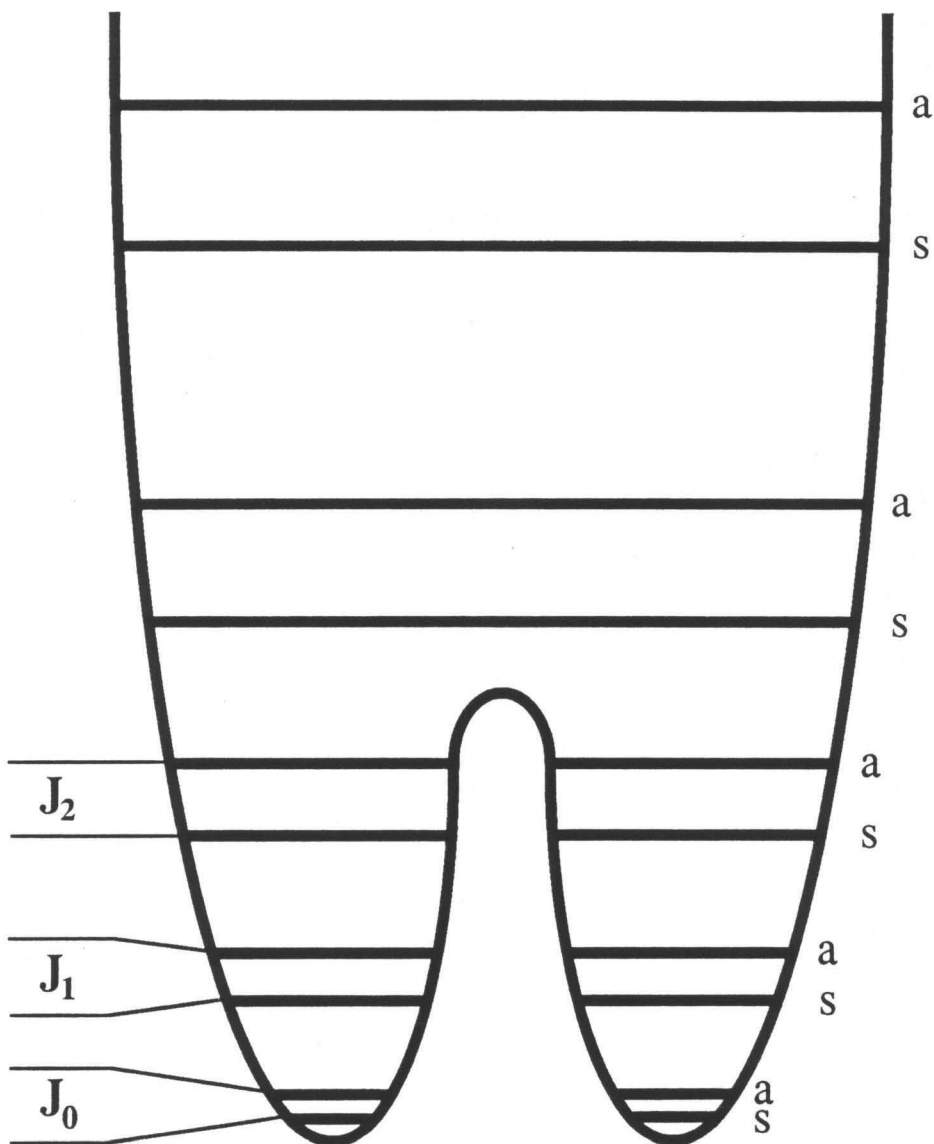


**Figure 2.2: Energy levels of a symmetric double-well.** The spatial eigenstates are either symmetric (s) or antisymmetric (a) with respect to exchange. The average energy of the  $n$ th rovibrational doublet is  $E_n$ , while  $J_n$  is the  $n$ th tunnel splitting. The  $J_n$ 's increase with increasing vibrational quantum number.

a system created in a non-stationary state. For example, an initial condition that is a wavepacket localised in one of the wells (this is a non-stationary state since neither  $\psi_I$  nor  $\psi_{II}$  is an eigenstate of  $\mathcal{H}_{\text{int}}$ ) oscillates sinusoidally between the two wells.

In principle, the solution of the Schrödinger equation subject to the appropriate boundary conditions yields complete information about the tunnelling. An exact solution, however, is rarely possible. Moreover, perturbative methods invariably fail to treat tunnelling accurately since the absolute value of the wave function changes through many orders of magnitude on going from the classically accessible region to the inaccessible region. This is one of the main reasons for the interest in tunnelling from a fundamental standpoint, particularly in quantum field theory, and for the development of semiclassical methods akin to either WKB method or to the path integral description of quantum mechanics.[57]

This thesis is concerned with the case where the tunnel splittings are resolvable in the NMR spectrum, but there are other systems where this not the case. When the tunnel splittings are not resolved, the temperature dependent NMR lineshapes still contain information about the tunnelling. The kinetic parameters are extracted from the temperature dependent lineshapes using methods briefly discussed in the section on exchange. If the Arrhenius plot of  $\ln k$  vs.  $1/T$  for the measured rate constants shows a deviation from linearity then it is usually interpreted qualitatively as a sign of tunnelling. An extreme case, sometimes seen at low temperatures, is when the rate constants are nonzero and temperature independent which is a sure sign of tunnelling.

In conclusion, this chapter briefly discussed the properties of the transition metal trihydrides that prompted the investigation reported in Part I of this thesis. Concepts like quantum-mechanical exchange, quantum-mechanical tunnelling, and chemical exchange that form the framework of the work reported in the following two chapters were also introduced.

## 2.4 References

- [1] R. H. Crabtree, D. G. Hamilton, *Adv. Organomet. Chem.*, **28**, 299 (1988)
- [2] R. H. Crabtree, *Chem. Rev.*, **85**, 245 (1985)
- [3] G. J. Kubas, *J. Chem. Soc. Chem. Commun.*, 61 (1980)
- [4] G. J. Kubas, *Acc. Chem. Res.*, **21**, 120 (1988)
- [5] J. Eckert, G. J. Kubas, A. J. Dianoux, *J. Chem. Phys.*, **88**, 466 (1988)
- [6] J. Eckert, G. J. Kubas, J. H. Hall, P. J. Hay, C. M. Boyle, *J. Am. Chem. Soc.*, **112**, 2324 (1990)
- [7] L. S. van der Sluys, J. Eckert, O. Eisenstein, J. H. Hall, J. C. Huffman, S. A. Jackson, T. F. Koetzle, G. J. Kubas, P. J. Vergamini, K. G. Caulton, *J. Am. Chem. Soc.*, **112**, 4831 (1990)
- [8] D. G. Hamilton, R. H. Crabtree, *J. Am. Chem. Soc.*, **110**, 4126 (1988)
- [9] G. J. Kubas, R. R. Ryan, B. I. Swanson, P. J. Vergamini, H. J. Wasserman, *J. Am. Chem. Soc.*, **106**, 451 (1984)
- [10] X-L. Luo, R. H. Crabtree, *J. Am. Chem. Soc.*, **112**, 6912 (1990)
- [11] J. K. Burdett, J. R. Phillips, M. R. Pourian, M. Poliakoff, J. J. Turner, R. Upmacis, *Inorg. Chem.*, **26**, 3054 (1987)
- [12] J. K. Burdett, M. R. Pourian, *Organometallics*, **6**, 1685 (1987)
- [13] R. A. Paciello, J. E. Bercaw, Abstracts of papers, 191st national meeting of the American Chemical Society, INOR 82, New York (1986)
- [14] R. A. Paciello, Ph.D. Thesis, California Institute of Technology, Pasadena (1987)

- [15] T. Arliguie, B. Chaudret, J. Devillers, R. Poilblanc, C. R. Seances Acad. Sci. Ser. 2, **305**, 1523 (1987)
- [16] T. Arliguie, C. Border, B. Chaudret, J. Devillers, R. Poilblanc, *Organometallics*, **8**, 1308 (1989)
- [17] T. Arliguie, B. Chaudret, F. A. Jalon, A. Otero, J. A. Lopez, F. J. Lahoz, *Organometallics*, **10**, 1888 (1991)
- [18] A. Antinolo, B. Chaudret, G. Commenges, M. Fajardo, F. Jalon, R. H. Morris, A. Otero, T. C. Schweltzer, *J. Chem. Soc. Chem. Commun.*, 1210 (1988)
- [19] D. M. Heinekey, N. G. Payne, G. C. Schulte, *J. Am. Chem. Soc.*, **110**, 2303 (1988)
- [20] D. H. Jones, J. A. Labinger, D. P. Weitekamp, *J. Am. Chem. Soc.*, **111**, 3087 (1989)
- [21] K. W. Zilm, D. M. Heinekey, J. M. Millar, N. G. Payne, P. G. Demou, *J. Am. Chem. Soc.*, **111**, 3088 (1989)
- [22] D. M. Heinekey, J. M. Millar, T. F. Koetzle, N. G. Payne, K. W. Zilm, *J. Am. Chem. Soc.*, **112**, 909 (1990)
- [23] D. M. Heinekey, *J. Am. Chem. Soc.*, **113**, 6074 (1991)
- [24] D. M. Heinekey, T. G. P. Harper, *Organometallics*, **10**, 2891 (1991)
- [25] J. A. Labinger in *Comprehensive Organometallic Chemistry*, ed. G. Wilkinson, F. G. A. Stone, E. W. Abel, Vol. 3 (Oxford: Pergamon Press, 1982)
- [26] T. M. Gilbert, R. G. Bergman, *J. Am. Chem. Soc.*, **107**, 3502 (1985)
- [27] M. D. Curtis, L. G. Bell, W. M. Butler, *Organometallics*, **4**, 701 (1985)
- [28] C. R. Bowers, D. H. Jones, N. D. Kurur, M. G. Pravica, J. A. Labinger, D. P. Weitekamp, *Adv. Magn. Reson.*, **14**, 269 (1990)

- [29] K. W. Zilm, D. M. Heinekey, J. M. Millar, N. G. Payne, S. P. Neshyba, J. C. Duchamp, J. Szczyrba, *J. Am. Chem. Soc.*, **112**, 920 (1990)
- [30] K. W. Zilm, J. M. Millar, *Adv. Magn. Reson.*, **15**, 163 (1990)
- [31] C. R. Bowers, Ph. D. Thesis, California Institute of Technology, Pasadena (1991)
- [32] P. A. M. Dirac, *The Principles of Quantum Mechanics* (London: Oxford University Press, 1958)
- [33] J. H. Van Vleck, *The Theory of Electric and Magnetic Susceptibilities* (London: Oxford University Press, 1932)
- [34] M. C. Cross, D. D. Osheroff, *Phys. Today.*, **40**(2), 35 (1987)
- [35] M. C. Cross, *Jap. Jour. App. Phys.*, **26**, suppl. 26-3, 1855 (1987)
- [36] N. S. Sullivan, *Bull. Magn. Reson.*, **11**, 86 (1987)
- [37] D. J. Thouless, *Proc. Phys. Soc.*, **86**, 893 (1965)
- [38] L. M. Jackman, F. A. Cotton, ed., *Dynamic Nuclear Magnetic Resonance Spectroscopy* (New York: Academic Press, 1975)
- [39] J. I. Kaplan, *NMR of Chemically Exchanging Systems* (New York: Academic Press, 1980)
- [40] J. Sandström, *Dynamic NMR Spectroscopy* (London: Academic Press, 1982)
- [41] H. S. Gutowsky, D. M. McCall, C. P. Slichter, *J. Chem. Phys.*, **21**, 279 (1953)
- [42] H. M. McConnell, *J. Chem. Phys.*, **28**, 430 (1958)
- [43] G. Binsch, *J. Am. Chem. Soc.*, **91**, 1304 (1969)
- [44] D. A. Kleier, G. Binsch, *J. Magn. Reson.*, **3**, 146 (1970)

- [45] G. Binsch in *Dynamic Nuclear Magnetic Resonance Spectroscopy*, ed. L. M. Jackman, F. A. Cotton (New York: Academic Press, 1975)
- [46] G. Binsch, H. Kessler, *Angew. Chem. Int. Ed. Engl.*, **19**, 411 (1980)
- [47] D. S. Stephenson, G. Binsch, *J. Magn. Reson.*, **32**, 145 (1978)
- [48] D. S. Stephenson, G. Binsch, QCPE Program No. 365, Quantum Chemistry Program Exchange, Indiana University, Bloomington (1978)
- [49] I. O. Sutherland, *Annu. Rep. NMR Spectrosc.*, **4**, 71 (1971)
- [50] N. D. Kurur, D. H. Jones, D. P. Weitekamp, *Proceedings of the 25th Ampere Congress on Magnetic Resonance and Related Phenomena (Stuttgart 1990)*, ed. M. Mehring, J. U. von Schutz, H. C. Wolf (New York: Springer-Verlag, 1990), p. 182
- [51] R. P. Bell, *The Tunnel Effect in Chemistry* (London: Chapman and Hall, 1980)
- [52] V. I. Goldanskii, L. I. Trakhtenberg, V. N. Fleurov, *Tunnelling Phenomena in Chemical Physics* (New York: Gordon and Breach, 1989)
- [53] C. B. Duke, *Tunnelling in Solids* (New York: Academic Press, 1969)
- [54] B. Chance, D. C. Devault, H. Frauenfelder, R. A. Marcus, J. R. Schrieffer, N. Sutin, *Tunnelling in Biological Systems* (New York: Academic Press, 1979)
- [55] D. K. Roy, *Quantum Mechanical Tunnelling and its Applications* (Singapore: World Scientific, 1986)
- [56] A. J. Leggett, S. Chakravarty, A. T. Dorsey, M. P. A. Fisher, A. Garg, W. Zwerger, *Rev. Mod. Phys.*, **59**, 1 (1987)
- [57] M. Razavy, A. Pimpale, *Phys. Rep.*, **168**, 305 (1988)

## Chapter 3

# Scalar Coupling in Transition Metal Trihydrides

The symmetrisation postulate of quantum mechanics comes into play when the coordinates of two or more identical particles are permuted in a system where tunnelling exchange can occur. This results in a nonmagnetic scalar coupling between the particles. This coupling, the exchange coupling, is now known to be present in a number of transition metal trihydrides and accounts for the interesting NMR properties of these compounds. The results of a computational study undertaken to semiquantitatively understand the magnitude of the exchange coupling and its temperature dependence in the transition metal trihydrides are presented in this chapter.

The calculation of the exchange coupling involves solving a quantum-mechanical model that allows for the exchange of the nuclei of interest. Here, attention is restricted to the three hydrogens of the trihydride which show the interesting NMR properties. A complete solution of the problem would require the solution of a multi-dimensional Schrödinger equation, which is computationally demanding. The approach adopted here is, therefore, to solve the Schrödinger equation for a one-dimensional potential which retains the characteristics of the original problem, but is computationally tractable. The approximations involved in reducing the multi-dimensional problem to a one-dimensional one are first presented. The results summarised in Chapter 2 showed that the  $AB_2$  spin system formed by the three protons in the transition metal trihydrides undergoes more pair exchange than cyclic exchange. This implies that solving for the two particle  $AB$  subsystem is adequate for an understanding of the three particle case. The second ap-

proximation involves restricting the two particles to exchange positions in one dimension. The severity of the approximation restricting the particles to one-dimensional motion is difficult to evaluate quantitatively, but the most likely effect is that, given a barrier height, the tunnelling contribution is underestimated. This is, for example, seen in the case of two interacting one-dimensional harmonic oscillators where the ground state tunnelling splitting is half of that seen in the corresponding three dimensional case.[1] Indistinguishability of the two configurations obtained by switching the positions of the two protons requires that the potential for proton motion have identical values at coordinates related by the exchange of proton labels. The symmetry does not imply that the two proton sites are chemically equivalent, but that the energy of the molecule is the same when the two protons exchange places. An example of a potential that satisfies this criterion is the symmetric double well of Figure 2.2. The specific models that fall into this category and that have been solved during the course of this study are discussed later.

A number of objections can be raised to the use of separable one-dimensional potentials in this problem. The foremost among them is the relation, if any, of such simplified models to the multidimensional Schrödinger equation of the molecules. Even though one-dimensional analogues of multidimensional problems in physics are less structured and less colourful than the real world, they are easier to solve and are surprisingly informative. Moreover, they usually serve as a first step towards the final goal, a complete solution of the problem. This was the rationalisation for embarking on a solution of the one-dimensional spatial problem.

### 3.1 The Hamiltonian

The exchange operator was shown in Chapter 2 to have the form

$$\mathcal{H}_{\text{exchange}} = J^e \left( \frac{1}{4} + \mathbf{I}_A \cdot \mathbf{I}_B \right), \quad (3.1)$$

where  $J^e$  is the splitting between the symmetric and antisymmetric spatial states

$$J^e = E^a - E^s.$$

The  $\frac{1}{4}J^e$  term only acts to shift the energy of all levels by the same amount. The spin eigenfunctions for two coupled protons are

$$|1_-\rangle = |\beta\beta\rangle \quad (3.2)$$

$$|1_+\rangle = |\alpha\alpha\rangle \quad (3.3)$$

$$|0_+\rangle = \frac{1}{\sqrt{2}}(|\alpha\beta\rangle + |\beta\alpha\rangle) \quad (3.4)$$

$$|0_-\rangle = \frac{1}{\sqrt{2}}(|\alpha\beta\rangle - |\beta\alpha\rangle). \quad (3.5)$$

The kets  $|\alpha\rangle$  and  $|\beta\rangle$  denote the spin-up and spin-down states respectively. The first three states constitute the triplet or symmetric states while the last one is the singlet or antisymmetric state. In terms of these states, the exchange Hamiltonian can be rewritten as

$$\mathcal{H}_{\text{exchange}} = \frac{J^e}{2}(|0_+\rangle\langle 0_+| + |1_+\rangle\langle 1_+| + |1_-\rangle\langle 1_-| - |0_-\rangle\langle 0_-|). \quad (3.6)$$

For a symmetric one-dimensional well, it was shown in Chapter 2 that the eigenvalues cluster in pairs with spatial eigenfunctions that are either symmetric (gerade) or antisymmetric (ungerade) with respect to exchange of the particle labels. If the successive pairs of levels are indexed by  $n$  then the Hamiltonian for each  $n$  has the form

$$\mathcal{H}_{\text{exchange}}(n) = J_{AB}^e(n)\left(\frac{1}{4} + \mathbf{I}_A \cdot \mathbf{I}_B\right), \quad (3.7)$$

where  $J_{AB}^e(n)$  is the tunnel splitting of the  $n$ th rovibrational state. In the rest of this chapter  $J_{AB}^e(n)$  will be represented by  $J_n$ . If  $|s_n\rangle$  and  $|a_n\rangle$  represent the  $n$ th symmetric and antisymmetric spatial states respectively and  $E_n$  is the average energy of a doublet, given by

$$E_n = \frac{E_n^s + E_n^a}{2},$$

then the Hamiltonian can be rewritten as

$$\begin{aligned} \mathcal{H}_{zf} = & \sum_n \left( E_n - \frac{J_n}{2} \right) (|s_n\rangle\langle s_n|)(|0_-\rangle\langle 0_-|) \\ & + \left( E_n + \frac{J_n}{2} \right) (|a_n\rangle\langle a_n|)(|0_+\rangle\langle 0_+| + |1_+\rangle\langle 1_+| + |1_-\rangle\langle 1_-|). \end{aligned} \quad (3.8)$$

The two spins are assumed to be equivalent so far, since no chemical shift has been included in the Hamiltonian. This is justified since it is experimentally observed that the exchange couplings are field independent. Hence, the chemical shift of the two protons will continue to be ignored for the rest of the chapter. All the spatial calculations reported in this chapter can thus be done as if the system were in zero magnetic field, which implies that the spin states can be excluded from the analysis and the Hamiltonian can be written as

$$\mathcal{H}_{zf} = \sum_n \left( E_n - \frac{J_n}{2} \right) |s_n\rangle\langle s_n| + \left( E_n + \frac{J_n}{2} \right) |a_n\rangle\langle a_n| \quad (3.9)$$

$$= \sum_n E_n (|s_n\rangle\langle s_n| + |a_n\rangle\langle a_n|) + \frac{J_n}{2} (|a_n\rangle\langle a_n| - |s_n\rangle\langle s_n|). \quad (3.10)$$

The presence of the chemical shift is, however, important for the measurement of exchange couplings as spectral splittings in liquids. In its absence, the  $J$ -coupling Hamiltonian commutes with the Zeeman terms of the Hamiltonian and does not appear in the spectrum.[2, 3] The presence of the chemical shift also differentiates this system from the low temperature solids where exchange coupling has been observed by virtue of not commuting with direct dipolar couplings.

The chemical shifts can, if necessary, be modelled with a spatial Schrödinger equation by adding an appropriate ungerade potential making the well slightly asymmetric in a spin dependent manner. The effect of this term in the potential can then be viewed as a perturbation which connects eigenstates of the symmetric potential of opposite symmetry.

### 3.2 Average Tunnel Splitting

The tunnel splitting measured in an NMR experiment at a finite temperature is an ensemble average, since the phonon mediated change in  $n$  is much faster than the NMR timescale. These fast processes do not involve any change of spin state. A similar situation is also present in the case of methyl groups undergoing rotational tunnelling. In the methyl group literature an intuitively reasonable, but unjustified, expression for the average exchange coupling first employed by Powles and Gutowsky[4] is used routinely. In this model the average exchange coupling is given by

$$\bar{J}(T) = \frac{1}{Z} \sum_n J_n \exp(-\beta E_n) \quad (3.11)$$

$$= \sum_n J_n p_n. \quad (3.12)$$

Here  $J_n$  and  $p_n$  are the tunnel splitting and the population of the  $n$ th rovibrational level while  $E_n$  is the average energy of the  $n$ th doublet. The partition function  $Z$  is given by

$$Z = \sum_n \exp(-\beta E_n).$$

Because the  $E_n$  are not eigenvalues of the Hamiltonian, this cannot be a precise statistical mechanical average. Stejskal and Gutowsky [5] expressed similar doubts in 1958, but offered no alternative. This leaves us in the surprising position of needing to derive a proper expression for a quantity that has been considered to be understood for over three decades.

A logical way of remedying the insufficiency in this averaging procedure is by explicitly considering the population of every state rather than the average energy of a doublet. This leads to the following expression for the ensemble averaged exchange coupling:

$$\bar{J}(T) = \frac{1}{Z_s} \sum_n E_n^s \exp(-\beta E_n^s) - \frac{1}{Z_a} \sum_n E_n^a \exp(-\beta E_n^a), \quad (3.13)$$

where  $E_n^s = (E_n - J_n)$  are legitimate eigenvalues and  $Z_s$  and  $Z_a$  are the partition functions

for the symmetric and antisymmetric states respectively. They are defined as

$$Z_s = \sum_n \exp(-\beta E_n^s) \quad (3.14)$$

$$Z_a = \sum_n \exp(-\beta(E_n^a)). \quad (3.15)$$

The symmetric and antisymmetric ladders are in separate equilibrium with the lattice and lattice fluctuations need not couple states of different symmetry. The equation 3.13 can be simplified and written as

$$\bar{J}(T) = \sum_n p_n^s E_n^s - p_n^a E_n^a \quad (3.16)$$

$$= \langle E_s \rangle - \langle E_a \rangle. \quad (3.17)$$

Rewriting equation 3.16 in a form containing the average energy of a doublet and the tunnel splitting produces

$$\bar{J}(T) = \sum_n (p_n^s - p_n^a) E_n - (p_n^s + p_n^a) \frac{J_n}{2} \quad (3.18)$$

$$= A(T) + B(T). \quad (3.19)$$

This rearrangement of  $\bar{J}(T)$  makes comparison with equation 3.12 straightforward. The second term  $B(T)$  in eq. 3.19 is in practice identical to equation 3.12, while the first term is a new term.

With the ingredients discussed at length in the previous section, one is in a position to calculate the magnitude and the temperature dependence of the scalar coupling in the transition metal trihydrides. The recipe involves choosing a spatial model that exhibits tunnelling and solving for its eigenvalues. From a knowledge of the eigenvalues, the ensemble averaged exchange coupling can be calculated by either of the two different averaging processes equation 3.12 or equation 3.13 mentioned above. The temperature dependence in the coupling then arises from the changing Boltzmann weights of the excited doublets. The potential parameters are varied until the calculated temperature dependence of the  $J$  coupling matches that measured experimentally. It is found that

the two averaging procedures give qualitatively different answers thus possibly vitiating the significance of earlier numerical fits all of which used equation 3.12. We now briefly turn our attention to the spatial models that were studied here and the methods that were used to determine the tunnel splitting.

### 3.3 Spatial Models

The potentials that were investigated can be broadly classified into two categories: the double-well anharmonic oscillator and the hindered rotor. Two different models were studied in the former case. The tunnelling coordinate in this case is the line joining the two nuclei, while in the latter the protons are constrained to move on a circle and the tunnelling coordinate corresponds to the angular displacement about the rotor coordinate. In the double well case the two particles could, in principle, pass through one another, but as already discussed this is only one of the many complaints that could be made about applying a one-dimensional Schrödinger equation to a molecule.

#### 3.3.1 Linear Double Well

The double-well anharmonic oscillator potential is of the form

$$V(x) = -ax^2 + bx^4. \quad (3.20)$$

A number of studies were also performed with the following potential

$$V(x) = ax^2 + b \exp(-cx^2). \quad (3.21)$$

The salient features of both these potentials are provided in Table. 3.1. The spatial Schrödinger equation that is solved is

$$\left( -\frac{\hbar^2}{2\mu} \frac{d^2}{dx^2} + V(x) \right) \Psi(x) = E\Psi(x), \quad (3.22)$$

where  $\mu$  is the reduced mass. All the tunnel splittings  $J_n$  are positive for a linear one-dimensional Schrödinger equation.

**Table 3.1: Parameters for linear double well.** Physically interesting parameters of the two linear double well potentials.

	Anharmonic oscillator	Oscillator + Gaussian
Well separation	$\sqrt{\frac{2a}{b}}$	$2\sqrt{\frac{1}{c} \ln \frac{bc}{a}}$
Barrier Height	$\frac{a^2}{4b}$	$b - \frac{a}{c} (\ln \frac{bc}{a} + 1)$
FWHM	$\sqrt{\frac{a\sqrt{2}}{b}(\sqrt{2} - 1)}$	No analytical expression

### 3.3.2 Hindered Rotor

The Schrödinger equation for a hindered rotor is

$$\left( -\frac{\hbar^2}{2I} \frac{d^2}{d\theta^2} + V(\theta) \right) \Psi(\theta) = E\Psi(\theta), \quad (3.23)$$

where  $I = \mu r^2$  is the moment of inertia and  $V(\theta)$  is the hindering potential. The potential has the functional form

$$V(\theta) = \frac{V_0}{2} \cos 2\theta, \quad (3.24)$$

where  $V_0$  is the barrier height. The similarity of this Schrödinger equation to the Mathieu equation in its canonical form

$$\frac{d^2 y}{dx^2} + (\lambda - 2q \cos 2x)y = 0 \quad (3.25)$$

is apparent. [6] The solutions of this equation obey periodic boundary conditions given by

$$y(0) = y(\pi) = 0 \quad \text{and} \quad y'(0) = y'(\pi) = 0. \quad (3.26)$$

The Mathieu equation has one important characteristic that differentiates it from the linear double-well Schrödinger equations. The tunnel splittings alternate in sign, i. e.,  $J_{2n} > 0$  while  $J_{2n-1} < 0$ .

### 3.4 Determination of Tunnel Splitting

A wide variety of methods have been used in the literature to determine the tunnel splitting. Two related methods involving eigenvalues and eigenfunctions found by diagonalisation are discussed here. The matrix method used in most of the calculations is discussed in greater length in Appendix D.

#### 3.4.1 Eigenvalue Method

A number of methods exist to obtain the eigenvalues numerically; the method adopted here is an implementation of an algorithm due to Harris, Engerholm, and Gwinn (HEG).[7] It is a matrix method and involves diagonalising the Hamiltonian determined in a suitable basis. The harmonic oscillator basis was used for the two linear potentials, while the Mathieu equation was solved in the free rotor basis. The method was chosen mainly because of the ease of implementation. The tunnel splitting is easily calculated from the energy-ordered eigenvalues obtained by the diagonalisation as

$$J_n = E_{2n+1} - E_{2n}; \quad n = 0, 1, \dots \quad (3.27)$$

More details of this method can be found in Appendix D.

#### 3.4.2 Basic Gap Formula

The eigenvalue method to determine the tunnel splitting should be contrasted with an eigenfunction formula for the eigenvalue gap between states of opposite symmetry that is sometimes called the basic gap formula and is based on a simple integration by parts method.[8]

Let  $\psi_i$  and  $\psi_j$  be two states satisfying the same Schrödinger equation

$$\left[ -\frac{1}{2}\nabla^2 + V(\mathbf{x}) - E_a \right] \psi_a(\mathbf{x}) = 0; \quad a = i, j. \quad (3.28)$$

Here  $E_i$  and  $E_j$  are the energies or eigenvalues of the two states. Multiplication of the Schrödinger equation satisfied by  $\psi_i$  with  $\psi_j$  and subtraction from the corresponding equation for  $\psi_j$  multiplied by  $\psi_i$  results in

$$\frac{1}{2}(\psi_i \nabla^2 \psi_j - \psi_j \nabla^2 \psi_i) = (E_i - E_j) \psi_i \psi_j. \quad (3.29)$$

Integration of this expression over the domain  $D$  on which the two wavefunctions are solutions and rearrangement gives

$$E_i - E_j = \frac{\int_D (\psi_i \nabla^2 \psi_j - \psi_j \nabla^2 \psi_i) dV}{2 \int_D \psi_i \psi_j dV}. \quad (3.30)$$

The numerator can be simplified by the use of Green's second identity

$$\int_D (u \nabla^2 v - v \nabla^2 u) dV = \int_S \hat{\mathbf{n}} \cdot (u \nabla v - v \nabla u) dS, \quad (3.31)$$

leading to the following formula for the energy gap

$$E_i - E_j = \frac{\int_S \hat{\mathbf{n}} \cdot (\psi_i \nabla \psi_j - \psi_j \nabla \psi_i) dS}{2 \int_D \psi_i \psi_j dV}. \quad (3.32)$$

$S$  is the closed surface enclosing the domain  $D$  and  $\hat{\mathbf{n}}$  is the unit outward normal.

In one dimension this expression has the simple form

$$E_i - E_j = \frac{(\psi_i \psi_j' - \psi_j \psi_i')|_0^\infty}{2 \int_0^\infty \psi_i \psi_j dx}. \quad (3.33)$$

A comparison of the tunnel splittings obtained by the matrix method and the basic gap formula was made for the Mathieu equation. The basic gap formula was extended to treat the periodic boundary conditions that the solutions of the Mathieu equation satisfy. The eigenfunctions required for the determination of the tunnel splitting by the basic gap formula were calculated by the HEG method as linear combinations of free rotor states. For the same number of basis states, the accuracy achieved with the basic gap formula was consistently worse relative to the literature values [9] that were obtained by the matrix method.

### 3.5 Fitting Procedure

The fits to the observed experimental data was obtained[10] for the harmonic oscillator with a Gaussian perturbation using the Powles and Gutowsky or “old” averaging procedure (equation 3.12). The results of these studies are presented first. Fits have not been obtained to the observed experimental data with the refined or “new” averaging procedure. However, the trends observed in the exchange coupling with this averaging procedure show some consistent and important differences from the old averaging procedure and these are presented by way of model calculations. Before the results of the calculations are discussed, it is necessary to clarify the choice of the parameters held constant during all the calculations.

The exchange coupling was shown to have a form similar to the magnetic scalar coupling. In such systems the  $J$  coupling that is measured is hence a sum of the exchange and indirect, or magnetic, contributions and is given by

$$J(T) = \bar{J}(T) + J^i, \quad (3.34)$$

where  $J^i$  is the usual indirect/magnetic electron mediated coupling and does not show any drastic temperature dependence.  $\bar{J}$  is the average exchange contribution. One important point to keep in mind is that usually little is known about the sign of the  $J$  coupling, being obtainable only from double resonance[11] or more sophisticated NMR experiments.[12] The relative signs of the two contributions in equation 3.34 are important in determining the observed magnitude of the  $J$  coupling. For lack of better evidence the sign of the  $J$  coupling in all the transition metal trihydrides was assumed to be the same as that measured in the dihydride  $\text{RhH}_2\text{Cl}(\text{PPh}_3)_2$ . In experiments performed in this laboratory,[12] the absolute sign of the proton-proton coupling in this rhodium dihydride was found to be negative. The magnitude of the indirect coupling in the trihydrides can, however be obtained, although only indirectly, by scaling the coupling measured in the tritiated isotopomer by the ratio  $\gamma_H/\gamma_T$  (0.94). Unfortunately, these measurements have

been made on only one tritiated compound,  $[\text{IrH}_2\text{TCp}(\text{AsPh}_3)]^+$ , [13] and due to lack of additional evidence, the same value has been used for all the compounds. An interesting observation in this regard is the fact that the values measured for the coupling constant with the tritium in the *A* and *B* positions are different: 29 and 24 Hz, respectively. The reason for this difference is not known, but has been speculated to be a subtle mass effect on the electronic wavefunctions. Thus the indirect coupling in all the transition metal trihydrides has been assumed to be  $-25$  Hz.

The Schrödinger equations were all solved with the reduced mass,  $\mu$ , of two protons (0.5 amu). In  $[\text{IrCp}(\text{PMe}_3)\text{H}_3]\text{BF}_4$  the proton-proton bondlength was determined by neutron diffraction to be  $1.7 \text{ \AA}$ . [13] The proton-proton bondlength was fixed at this value in all the calculations.

### 3.6 Fits to Experimental Data

The potential involving a harmonic oscillator converted into a double well by a Gaussian barrier was used with the old averaging procedure to fit the experimental  $J(T)$  data. This potential is not locally symmetric about each of the minima; for the potential parameters that led to fits, the potential is steeper on the inside wall of each well at half the barrier height than on the outside wall at the same height. The fitting parameter minimised was the sum of the squares of the deviations between experimental data and theoretical predictions. The search for the parameters that led to a fit of the experimental data was performed using a simplex algorithm. The root-mean-square deviation ranges from 3.3 to 7.7 Hz per data point for the different molecules. The fits are nearly as good as the data, if one assumes that the scatter in the data away from a smooth curve is a measure of experimental uncertainty in line position and temperature. The resulting fits for representative data sets are shown in Figures 3.1 and 3.2. The parameters obtained from the fitting procedure described are barrier widths and heights. The barrier heights

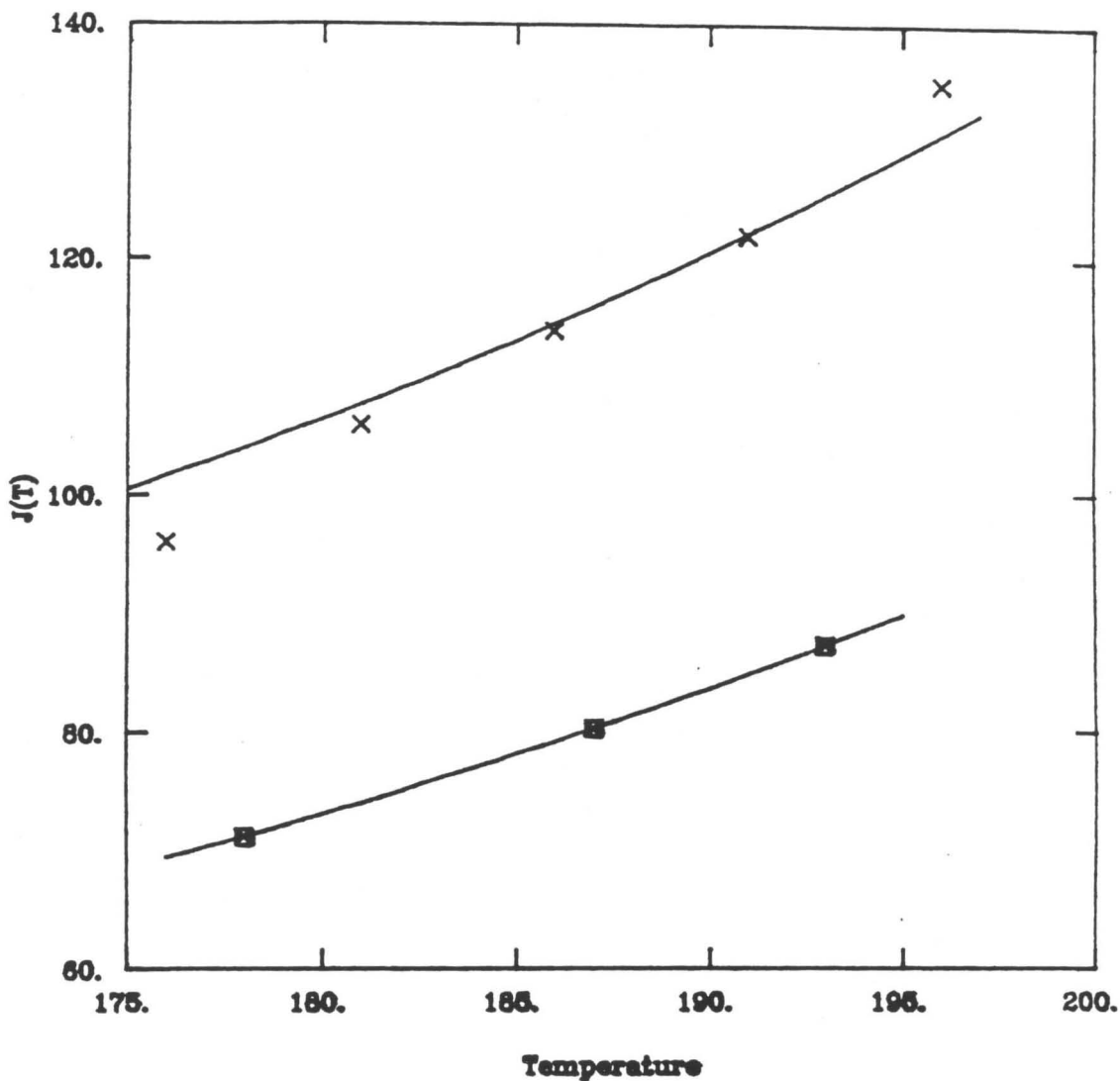
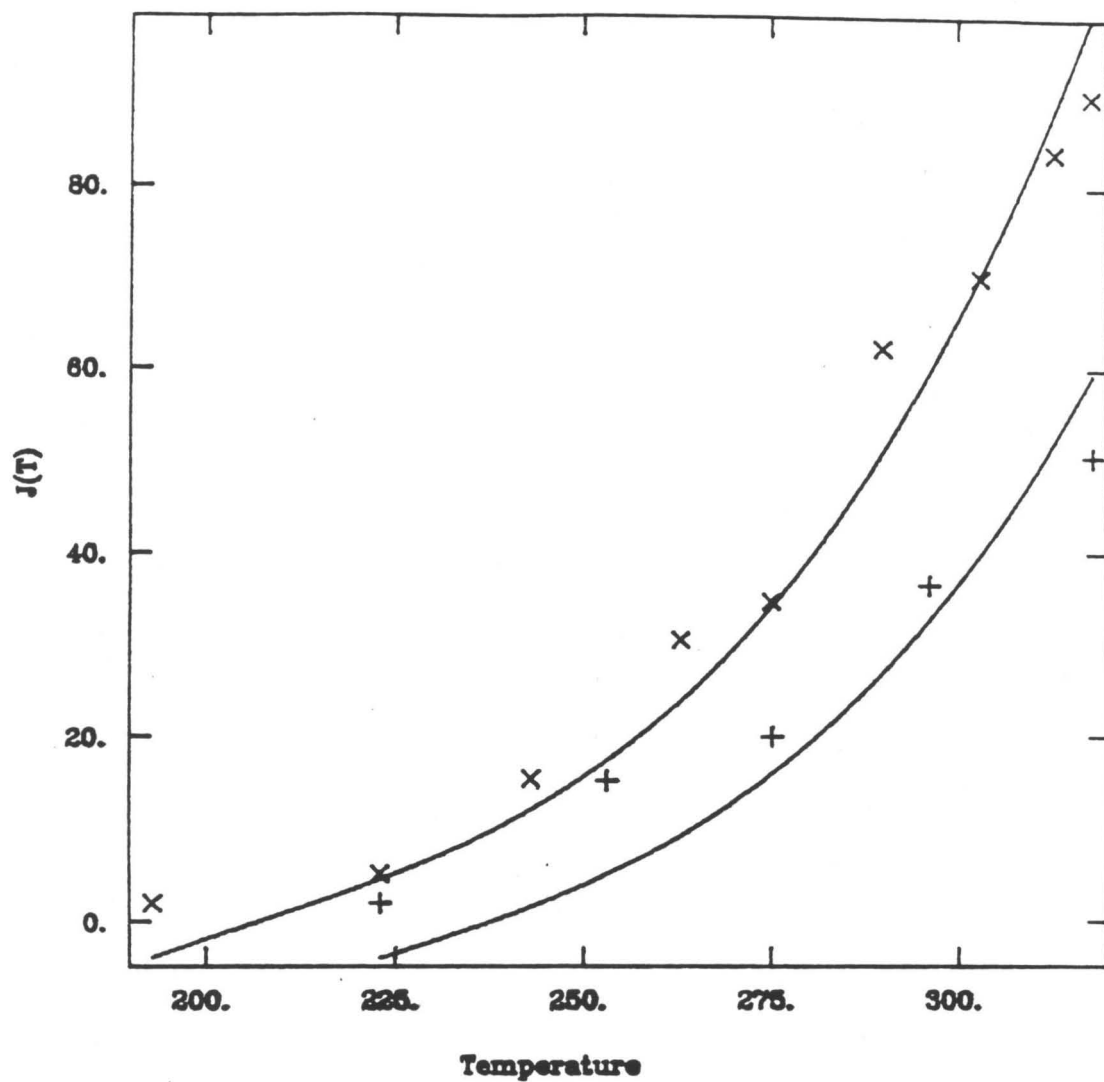


Figure 3.1: Fits to the experimentally measured  $J(T)$  data I. a)  $[\text{IrH}_3\text{Cp}(\text{PMe}_3)]^+$  represented by  $\times$  (Data from [14]) and b)  $\text{RuH}_3\text{Cp}^*(\text{PCy}_3)$  represented by  $\boxtimes$  (Data from [15]). Solid lines represent the fits in both cases. See text for fitting procedure and Table 3.2 for parameters.



**Figure 3.2: Fits to the experimentally measured  $J(T)$  data II.** a)  $\text{NbH}_3[\text{C}_5\text{H}_3(\text{SiMe}_3)_2]_2$  represented by  $\times$  (Data from [15]) and b)  $\text{NbH}_3(\text{C}_5\text{H}_4\text{SiMe}_3)_2$  represented by  $+$  (Data from [15]). Solid lines represent the fits in both cases. See text for fitting procedure and Table 3.2 for parameters.

are higher by factors of 1.5 to 2.5 than have been suggested on the basis of the standard formulation of chemical exchange and this might be viewed as a success of the present model. It is hardly surprising that transition state theory leads to underestimates of barrier height, since it neglects the possibility that states with large tunnel splitting below the barrier can serve the same role as the hypothetical transition state complex. It is worth noting that for various molecules, 5 to 6 pairs of spatial states contribute at least 1% to the calculated coupling at the highest temperature. These pairs have values of  $J_n$  increasing monotonically from 10 to  $10^7$  Hz. The highest such pairs have energies  $E_n$  from 23 to 45% of the barrier height.

**Table 3.2: Barrier height and width of potential that gave the best fit.**

Compound	Barrier Height kJ/mol	FWHM Å
$\text{NbH}_3[\text{C}_5\text{H}_3(\text{SiMe}_3)_2]_2$	98.8	1.34
$\text{IrH}_3\text{Cp}(\text{PMe}_3)^+$	79.4	1.51
$\text{NbH}_3(\text{C}_5\text{H}_4\text{SiMe}_3)_2$	101.5	1.33
$\text{RuH}_3\text{Cp}^*(\text{PCy}_3)$	85.2	1.39

The barrier widths of 1.33–1.51 Å in the relative coordinate can be viewed as angular widths of 24°–27° in atomic angular displacement, if one imagines the tunnelling coordinates as an arc at the metal-proton distance of 1.6 Å measured by neutron diffraction of  $\text{H}_2\text{Ir}(\text{SiEt}_3)_2(\text{C}_5\text{Me}_5)$ . [16] The energies associated with a change of unity in the vibrational quantum number are found to be 450–500  $\text{cm}^{-1}$ . These are below the range of 700–900  $\text{cm}^{-1}$  that has been observed for terminal hydride bends and wags in other metal hydrides. [17] Vibrational spectra and inelastic neutron scattering for these low-frequency modes are not presently available for the molecules that show exchange coupling, although such data, together with structural and  $J(T)$  results, will likely be critical to the

construction of a multidimensional model.

During the parameter search, the least-squares fits showed marked dependence on small changes in either the barrier height or the barrier width. Limitations of computer time currently make an exhaustive search of parameter space impractical. There is no doubt that the problem is underdetermined by the presently available data. While the full range of the bond lengths over which the data could be fit is not known, it is evident that the parameters can compensate for one another. This raises the question of uniqueness of the solutions; the present fits should not be taken as independent evidence for the bond length. The method of fitting with fixed distance was found to be reliable in the sense that starting the simplex procedure at different initial points led to either the same minimum or a local minimum with a much less satisfactory fit to the data.

Other calculations were performed to address the issue of isotope effects. A doubling of the effective mass without a change in the potential for  $\text{NbH}_3[\text{C}_5\text{H}_3(\text{SiMe}_3)_2]_2$ , as would ideally occur in the perdeuterated analog, decreases  $\bar{J}(318\text{K})$  from 120 to 0.1 Hz, an undetectably small value.

### 3.7 Comparison with Other Approaches

It would be desirable to confirm with a less idealised model that the results obtained with the separable one-dimensional tunnelling coordinate are qualitatively correct. A multidimensional approach, for example, using a suitable basis set and matrix methods, has not been attempted. Landesman,[18] in the context of solid  $^3\text{He}$ , has made an analytical calculation for the low-temperature limit of the exchange coupling of two identical particles interacting with each other and with two harmonic wells fixed in the lattice. The accuracy of this calculation as a solution to the given model is unknown; the approximations made are analogous to the Heitler–London treatment of the electronic wavefunction of  $\text{H}_2$ . The two-particle wavefunctions are not calculated, but are assumed to be the

symmetric and antisymmetric linear combinations of the product of the ground states of one-particle oscillators multiplied by a window function that sets the probability to zero within a certain interparticle distance. The parameters are this cutoff distance, the harmonic frequency, and the distance between the minima. These parameters simultaneously determine the overlap of the one-particle states and the barrier shape, which thus has discontinuities at the points between the minima where the probability is set to zero and which has the rather arbitrary property that the barrier height increases quadratically with internuclear distance. One objection[19] is that the highly constrained form of the trial wavefunction is not likely to simultaneously give the correct wavefunction both near the potential minima and under the barrier.

The Landesman model with hard-sphere repulsion has recently been applied to the NMR of anomalous hydrides.[20, 21] Additional difficulties are encountered here since the model has no anisotropy nor the topology of two protons bound to a common metal centre. More importantly, the accuracy with which it is solved is undeterminable. The same criticism applies to the extension to finite temperature,[21] where it is claimed that the relationship between the one-particle root-mean-square displacement and the exchange coupling found by Landesman for his ground state model applies also at any temperature. With the cutoff parameter fixed at  $1 \text{ \AA}$  the distance between minima and the harmonic frequency are varied. Good fits to  $J(T)$  are found.

Both the extended Landesman model and the one-dimensional tunnelling coordinate model succeed in fitting available data with parameters that are reasonable. The exactly solved model presented here uses potential barrier heights and vibrational splittings similar to those found with the alternative model. Both models have the property that all tunnel splittings are positive. Considering the differences in the models and the simplicity of both of them relative to a real molecule, comparisons between them are of limited significance, only highlighting the need for more realistic, but accurately solvable,

multidimensional models.

### 3.8 New Averaging Procedure

The temperature dependence of the ensemble averaged exchange coupling calculated by the new averaging procedure is drastically different from that of the old averaging procedure. An example of this calculation is presented in Figure 3.3 for both the hindered rotor and the anharmonic double-well oscillator. The calculations were performed in both cases for the case of a 2 amu reduced mass separated by 1 Å and a barrier height of 6.45 kJ/mol. For this particular choice of potential parameters the average exchange coupling is bigger than that seen in the trihydrides but the trends, however, are unlikely to change. The solid line in both graphs represents the exchange coupling calculated by the new averaging procedure (equation 3.13 or 3.16). The dashed line represents the contribution from the  $B(T)$  term which is similar in form to the old average term (equation 3.12), while the dotted line is the contribution to the new average from the  $A(T)$  term involving the average energy of the pair. This last contribution can be negative in the case of the double-well oscillator, although the sum  $\bar{J}(T)$  is still positive.

The hindered rotor and the double-well oscillator also behave qualitatively differently. The initial slope of  $J(T)$  is negative for the former and positive for the latter. In each case an extremum is reached and the slope reverses, a feature not present in the old averages, which are monotonic functions of  $T$ . The hindered rotor shows a pronounced maximum with almost no coupling at high temperature. This last fact can be rationalised to result from the tunnel splittings alternating in sign.

Optimisation of the potential parameters to obtain fits to the experimental  $J(T)$  with the new average are not yet available. With the qualitatively different behaviour exhibited by the two potential forms it would be hardly surprising if the potential parameters that led to the best fit differed drastically from that obtained with the old averaging procedure.

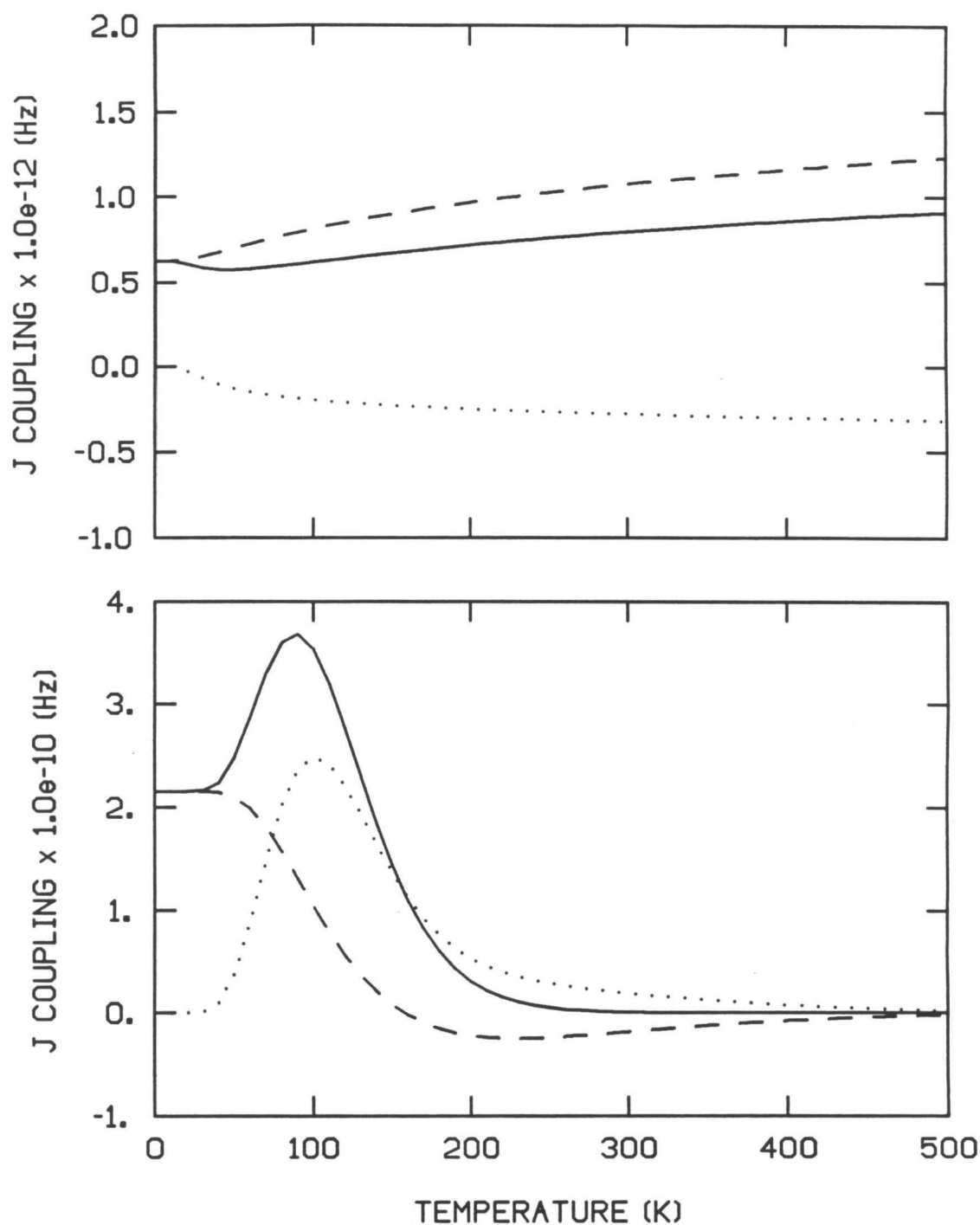
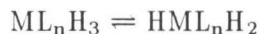


Figure 3.3: Average exchange coupling calculated with the averaging procedure of equation 3.13 or 3.16. *Top*: Double-well anharmonic oscillator. *Bottom*: Hindered rotor. Results are for a reduced mass of 2 amu and a barrier height of 6.45 kJ/mol. Solid, dotted and dashed lines correspond respectively to  $\bar{J}(T)$ ,  $A(T)$  and  $B(T)$  of equation 3.19.

### 3.9 Trihydride $\rightleftharpoons$ Dihydrogen Complex Equilibrium

A classical trihydride ground state in equilibrium with an excited electronic state containing dihydrogen and represented by



has been suggested [22] as an alternative model to explain the NMR properties of the trihydrides, but no quantitative work has been done. The  $H_2$  unit in other dihydrogen complexes is known from inelastic scattering spectroscopy to undergo hindered rotation. In this section preliminary calculations are performed for models of this type. The case where the tunnelling dihydrogen entity is situated  $500\text{ cm}^{-1}$  higher in energy than a ground classical trihydride state with no tunnelling is presented in Figure 3.4. The tunnelling of the dihydrogen in the excited electronic state was modelled by each of the spatial models already discussed and the average exchange coupling was computed as prescribed by the new averaging procedure (equation 3.13 or 3.16). The hindered rotor and the double-well oscillator show qualitatively different behaviour from one another and from the models discussed in the previous sections. In contrast to the models in the previous sections the average exchange coupling is zero at  $T = 0$  and only becomes finite when the thermal energy is sufficient to populate the excited tunnelling state. While the double-well oscillator predicts a monotonic increase in the average exchange coupling as a function of temperature, the hindered rotor exhibits a maximum and reduces to zero at higher temperatures. Moreover, although both models predict a positive average exchange coupling, the contributions from the two terms in equation 3.19 show widely different behaviour. The term  $B(T)$  (the term similar to the old average) is always positive in the double-well oscillator, while in the hindered rotor it is more often negative than positive.

The energy separation between the non-tunnelling trihydride ground-state and the dihydrogen is an extra parameter that can be varied in this model. To determine the

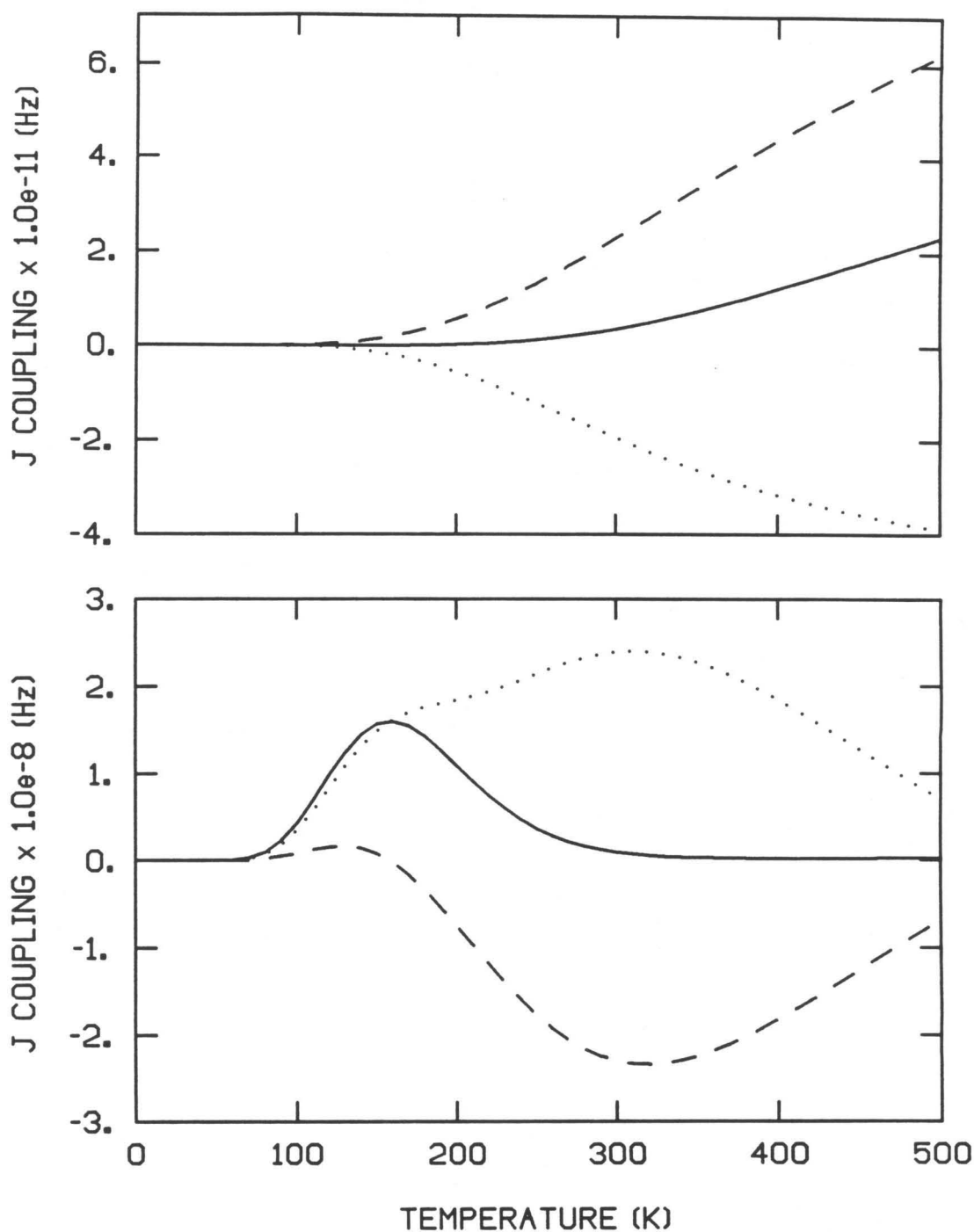


Figure 3.4: Average exchange coupling for the Trihydride  $\rightleftharpoons$  Dihydrogen complex equilibria I. Tunnelling of the dihydrogen in the excited state is modelled as a double-well anharmonic oscillator (top) and as a hindered rotor (bottom). Results are for a reduced mass of 2 amu and a barrier height of 6.45 kJ/mol and with the excited state located  $500\text{ cm}^{-1}$  from the ground state trihydride. Solid, dotted and dashed lines correspond respectively to  $\bar{J}(T)$ ,  $A(T)$  and  $B(T)$  of equation 3.19.

dependence of the average exchange coupling on this parameter the calculation was performed with the tunnelling state  $2000\text{ cm}^{-1}$  from the ground state and the results are presented in Figure 3.5. For this case, the average exchange coupling predicted by both the double-well and the hindered rotor is insignificant over the temperature range investigated. It is, however, important to note that the results predicted by the two averaging processes are drastically different. While the old averaging procedure (equation 3.12 or  $B(T)$  in equation 3.19 and represented by the dashed line in Figure 3.5) would predict a non-zero average exchange coupling the new averaging procedure (equation 3.13 and represented by the solid line in Figure 3.5) would predict an insignificant average exchange coupling due to the  $A(T)$  and  $B(T)$  terms in equation 3.19 being almost equal in magnitude but opposite in sign.

It would be interesting to vary both the energy separation between the ground state with no tunnelling and the excited tunnelling state as well as the barrier height on the excited potential energy surface in an effort to obtain fits to the observed  $J(T)$  data. The results with this model also emphasise the need for data over a wide range of temperatures as it is undoubtedly the case that multiple fits could be obtained to existing data.

### 3.10 Summary

In this chapter the resolved tunnel splittings that have been observed as spectral splittings in the NMR of transition metal trihydrides were explained by solving a Schrödinger equation which involved proton motion in a temperature independent potential with an average tunnelling coordinate. The couplings measured by NMR were rationalised as arising from ensemble averaging of the tunnel splittings from phonon mediated transitions between the vibrational manifolds, which also accounted for the temperature dependence of the measured couplings. The experimentally observed  $J(T)$  were fit consistently well from an optimisation of the potential parameters. The parameters that were obtained

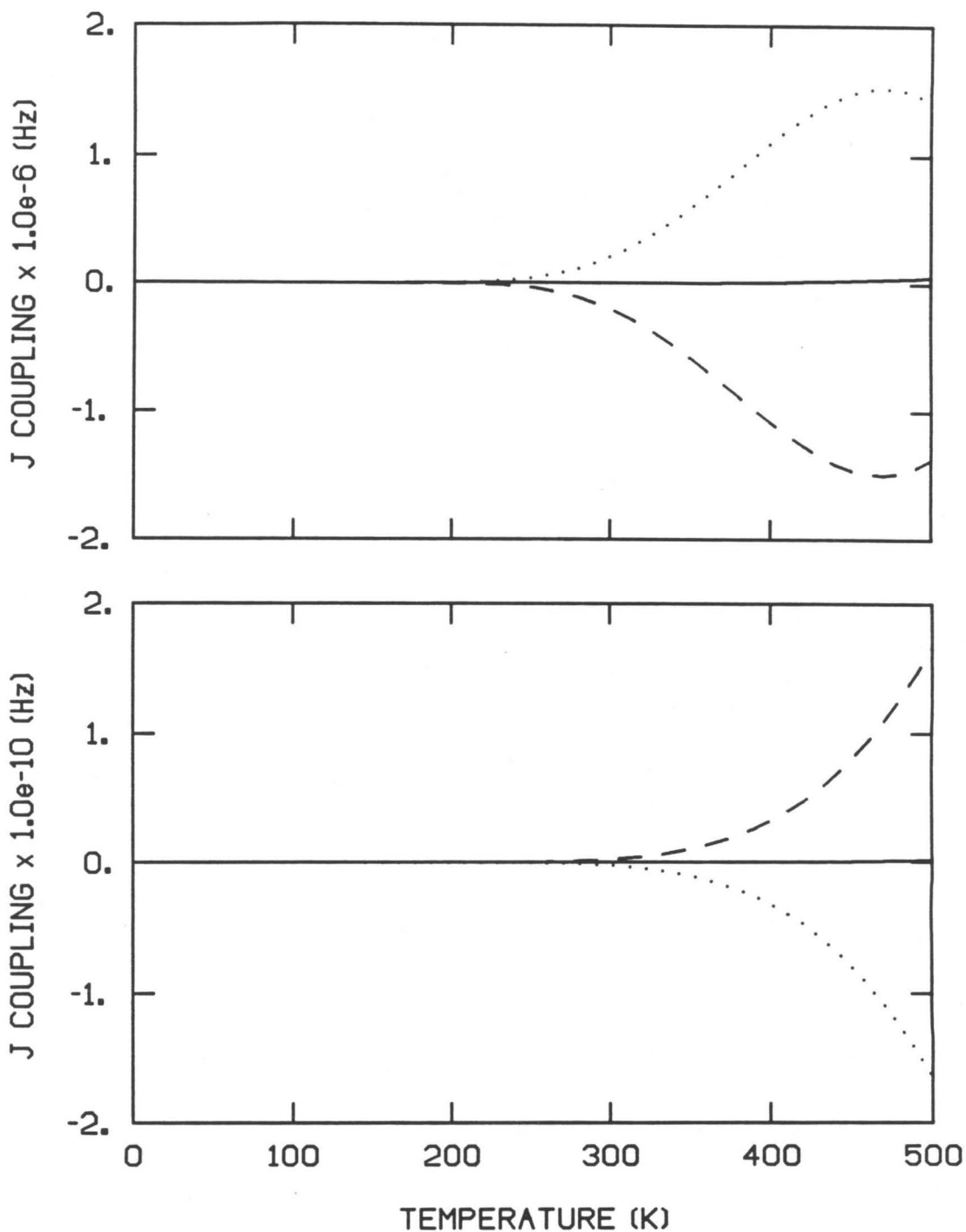


**Figure 3.5: Average exchange coupling for the Trihydride  $\rightleftharpoons$  Dihydrogen complex equilibria II.** Tunnelling of the dihydrogen in the excited state is modelled as a double-well anharmonic oscillator (top) and hindered rotor (bottom). Results are for a reduced mass of 2 amu and a barrier height of 6.45 kJ/mol with the excited state located  $2000\text{ cm}^{-1}$  from the ground state trihydride. Solid, dotted and dashed lines correspond respectively to  $\bar{J}(T)$ ,  $A(T)$  and  $B(T)$  of equation 3.19.

from such an analysis were consistently greater than that calculated from transition state theory. As a recent offshoot of this investigation it was realised that the averaging procedure used in the literature in the study of such systems has never been derived and is suspect. A new averaging procedure to overcome this problem was developed and found to give a qualitatively different relationships between  $J(T)$  and the underlying ladder of eigenstates.

### 3.11 References

- [1] W. A. Phillips in *Amorphous Solids: Low Temperature Properties*, ed. W. A. Phillips, (Berlin: Springer-Verlag, 1981)
- [2] A. Abragam, *Principles of Nuclear Magnetism* (Oxford: Oxford University Press, 1961)
- [3] H. S. Gutowsky, D. W. McCall, C. P. Slichter, *J. Chem. Phys.*, **21**, 279 (1953)
- [4] J. G. Powles, H. S. Gutowsky, *J. Chem. Phys.*, **23**, 1692 (1955)
- [5] E. O. Stejskal, H. S. Gutowsky, *J. Chem. Phys.*, **28**, 388 (1958)
- [6] M. Abramowitz, I. Stegun, *Handbook of Mathematical Functions* (New York: Dover, 1965)
- [7] D. O. Harris, G. G. Engerholm, W. D. Gwinn, *J. Chem. Phys.*, **43**, 1515 (1963)
- [8] E. M. Harrell, *Int. J. Quantum Chem.*, **21**, 199 (1982)
- [9] National Bureau of Standards, *Tables Relating to Mathieu Functions* (Washington D. C.: U. S. Government Printing Office, 1967)
- [10] C. R. Bowers, D. H. Jones, N. D. Kurur, M. G. Pravica, J. A. Labinger, D. P. Weitekamp, *Adv. Magn. Reson.*, **14**, 269 (1990)
- [11] W. McFarlane, D. S. Rycroft, *Annu. Repts. NMR Spectrosc.*, **9**, 320 (1979)
- [12] C. R. Bowers, D. P. Weitekamp, *J. Am. Chem. Soc.*, **109**, 5541 (1987)
- [13] D. M. Heinekey, J. M. Millar, T. F. Koetzle, N. G. Payne, K. W. Zilm, *J. Am. Chem. Soc.*, **112**, 910 (1990)
- [14] D. M. Heinekey, N. G. Payne, G. C. Schulte, *J. Am. Chem. Soc.*, **110**, 2303 (1988)

- [15] A. Antinolo, B. Chaudret, G. Commenges, M. Fajardo, F. Jalon, R. H. Morris, A. Otero, C. T. Schweltzer, *J. Chem. Soc., Chem. Commun.*, 210 (1988)
- [16] J. S. Ricci, T. F. Koetzle, M.-J. Fernandez, P. M. Maitlis, J. C. Green, *J. Organomet. Chem.*, **299**, 383 (1986)
- [17] G. J. Kubas, *Acc. Chem. Res.*, **21**, 120 (1988)
- [18] A. Landesman, *Ann. Phys.(Leipzig)*[8] **1**, 53 (1973-1974)
- [19] A. Abragam, M. Goldman *Nuclear Magnetism: Order and Disorder* (Oxford: Oxford University Press, 1981)
- [20] K. W. Zilm, S. P. Neshyba, J. C. Duchamp, D. M. Heinekey, J. M. Millar, T. F. Koetzle, N. G. Payne, *J. Am. Chem. Soc.*, **112**, 920 (1990)
- [21] K. W. Zilm, J. M. Millar, *Adv. Magn. Reson.*, **15**, 163 (1990)
- [22] T. Arliguie, C. Border, B. Chaudret, J. Devillers, R. Poilblanc, *Organometallics*, **8**, 1308 (1989)

## Chapter 4

# Lineshapes in Transition Metal Trihydrides

Temperature dependent lineshapes in NMR are usually attributed to chemical exchange processes. The standard analysis of such processes, briefly outlined in Chapter 2, typically involves the classical concept of molecular configuration and uses transition state theory to describe the rate of interconversion of such species. Such a classical analysis cannot self-consistently treat systems where the NMR lineshapes reflect both quantum and classical behaviour. In this chapter, a method is discussed that resolves this paradoxical situation by treating both the spin and the spatial degrees of freedom quantum-mechanically. Chemical exchange may then be described as arising from the coupling of the bound states of such systems to a thermal bath.

The effect of dissipation on quantum-mechanical tunnelling has been studied actively in the past few years because of its applicability to many systems of interest in both chemistry and condensed matter physics.[1] Most of the analysis has, however, been restricted to the case of the two lowest levels in a slightly asymmetric double-well (one level in each well) interacting with a lattice which is usually modelled as a set of harmonic oscillators. In a smaller number of recent papers, the ladder of tunnelling states [2, 3, 4, 5, 6, 7, 8] described in Chapter 3 has been considered in determining describing one-particle tunnelling characteristics in a number of systems. An ensemble averaging of the tunnel splitting over the excited tunnelling states was invoked in Chapter 3 to explain the magnitude and the temperature dependence of the scalar coupling in transition metal trihydrides. In this chapter the spectroscopic manifestations of the fluctuations in the

tunnel splittings due to stochastic coupling to a lattice are investigated. A Redfield [9, 10] relaxation analysis shows that the two-particle mutual chemical exchange rate can be identified as the low-frequency spectral density of the autocorrelation function of the fluctuations.[11] The fluctuations in the tunnel splittings arise as a result of rovibrational relaxation, which is modelled by a master equation.

Although the analysis presented here was aimed at understanding the temperature dependence of the lineshapes in transition metal trihydrides, the method is applicable to other similar systems where the NMR spectra reveal both resolved tunnel splittings and chemical exchange. More importantly, the method can be considered to be a quantum-mechanical derivation of mutual chemical exchange.

## 4.1 The System

The zero-field Hamiltonian for two particles in a double-well introduced in Chapter 3 (equation 3.8) extended to include the chemical shift interaction has the form

$$\begin{aligned}
\mathcal{H}_s = & \sum_n \left( E_n - \frac{J_n}{2} \right) (|s_n\rangle\langle s_n|)(|0_-\rangle\langle 0_-|) \\
& + \left( E_n + \frac{J_n}{2} \right) (|a_n\rangle\langle a_n|)(|0_+\rangle\langle 0_+| + |1_+\rangle\langle 1_+| + |1_-\rangle\langle 1_-|) \\
& + \omega_{0n}(|a_n\rangle\langle a_n|)(|1_+\rangle\langle 1_+| - |1_-\rangle\langle 1_-|) \\
& + \frac{\delta_n}{2} [(|a_n\rangle\langle s_n|)(|0_+\rangle\langle 0_-|) + (|s_n\rangle\langle a_n|)(|0_-\rangle\langle 0_+|)], \tag{4.1}
\end{aligned}$$

where the third term is the average Zeeman interaction of the spin pair and the last is the chemical shift difference.

A complete analysis of the coupling of this system to the lattice would involve solving a density matrix for the  $4N$  states (since there are 4 spin states for each  $n$ ) where  $N$  is the number of rovibrational manifolds. The time-scale separation of the spin-independent rovibrational relaxation processes ( $\approx$  picoseconds) and the spin-lattice processes ( $\approx$  seconds), however, suggests a factorisation of the space and spin degrees of freedom. Intro-

ducing a projection operator defined by

$$\begin{aligned}
 |n\rangle\langle n| &= |s_n\rangle\langle s_n|(|0_-\rangle\langle 0_-|) \\
 &+ |a_n\rangle\langle a_n|(|0_+\rangle\langle 0_+| + |1_+\rangle\langle 1_+| + |1_-\rangle\langle 1_-|),
 \end{aligned}
 \tag{4.2}$$

and spin angular momentum operators  $\mathbf{I}_A$  and  $\mathbf{I}_B$  for the sites  $A$  and  $B$ , in which spins 1 and 2 would be located in the classical limit of localised nuclei, the Hamiltonian can be rewritten as

$$\mathcal{H}_s = \sum_n |n\rangle\langle n| \left[ E_n + J_n \mathbf{I}_A \cdot \mathbf{I}_B + \omega_{0n}(I_{zA} + I_{zB}) + \frac{\delta_n}{2}(I_{zA} - I_{zB}) \right].
 \tag{4.3}$$

The point of replacing equation 4.1 by 4.3 is to show how one goes from a description of the Hamiltonian in terms of properly antisymmetrised states to the form in terms of labelled sites which is universal in the NMR literature. The legitimacy of this substitution is discussed later in the chapter. An additional simplification is possible in the case of the transition metal trihydrides, since the chemical shifts are independent of the rovibrational quantum number, i.e.,  $\omega_{0n} = \omega_0$  and  $\delta_n = \delta$ . For the trihydrides, the Hamiltonian reduces to

$$\mathcal{H}_s = \omega_A I_{zA} + \omega_B I_{zB} + \sum_n |n\rangle\langle n| (E_n + J_n \mathbf{I}_A \cdot \mathbf{I}_B),
 \tag{4.4}$$

where  $\omega_A = \omega_0 + \frac{\delta}{2}$ ,  $\omega_B = \omega_0 - \frac{\delta}{2}$  and use has been made of the identity

$$\sum_n |n\rangle\langle n| = 1.$$

If the operators  $|n\rangle\langle n|$  are viewed as number operators for molecular “configurations,” the Hamiltonian 4.3, augmented by a master equation describing rates between configurations, would describe a problem formally equivalent to  $N$ -site chemical exchange. Here, the  $|n\rangle\langle n|$  are defined by equation 4.2 in terms of the properly antisymmetrised states of the total Hamiltonian. The population of the “states”  $|n\rangle$  fluctuates due to rovibrational relaxation, in turn modulating the ensemble averaged tunnel splitting, which is the NMR observable. This “ $N$ -site” model is unnecessarily complex for the systems of interest

where the rovibrational relaxation is far more rapid than any other time evolution. Thus its effects are derived by what is essentially a second order time-dependent perturbation theory (Bloch-Wangsness-Redfield theory [9, 10, 12, 13]) appropriate for a weak and rapid random perturbation. Specifically, it is shown in this way that the fluctuating scalar coupling can cause transverse relaxation characterised by a chemical exchange rate that is obtained from the autocorrelation of the fluctuation.

## 4.2 Relaxation Due to Fluctuating Scalar Coupling

For a system governed by the Hamiltonian

$$\mathcal{H} = \mathcal{H}_0 + \mathcal{H}_r(t), \quad (4.5)$$

where  $\mathcal{H}_0$  is the average Hamiltonian and the random fluctuations are represented by  $\mathcal{H}_r(t)$ , the equation of motion for the density matrix,[9, 10, 12, 13]  $\rho$ , to second order in the perturbation is given as

$$\frac{d\rho(t)}{dt} = [\rho, \mathcal{H}_0] - \int_0^\infty [\mathcal{H}_r(t), [\mathcal{H}_r(t - \tau), \rho(t) - \rho^0]] d\tau. \quad (4.6)$$

For numerical evaluation, it is desirable to transform the equation of motion of the density operator into a matrix form. This may be done either by selecting a complete set of basis functions and evaluating the matrix elements of the relevant operators in this basis, or by selecting a complete set of basis operators and representing the relevant operators as vectors in this basis operator or superoperator representation. The analysis here was performed in the superoperator representation. In this representation the equation of motion of the density operator has the form

$$\frac{d\rho(t)}{dt} = (\Gamma - i\Lambda)\rho, \quad (4.7)$$

where  $\Gamma$  is the relaxation superoperator and the Liouvillian  $\Lambda$  describes the unitary evolution. Solution of this equation with the appropriate initial condition determines

$\rho(t)$ , from which the time domain signal is calculated as

$$S(t) = \text{Tr}\{\rho(t)I_+\}. \quad (4.8)$$

A matrix representation of equation 4.7 can be found for any orthonormal operator basis  $\{Q_j\}$ . The unitary evolution and relaxation matrices are given as[13]

$$\Lambda_{jk} = -\text{Tr}\{[Q_j, Q_k^\dagger]\mathcal{H}_0\} \quad (4.9)$$

$$\Gamma_{jk} = \int_0^\infty \text{Tr}\{[Q_j, \mathcal{H}_r(t)][Q_k^\dagger, \mathcal{H}_r(t-\tau)]\} \quad (4.10)$$

The Hamiltonian of interest is given by

$$\mathcal{H}_0 = \omega_A I_{zA} + \omega_B I_{zB} + \bar{J} \mathbf{I}_A \cdot \mathbf{I}_B \quad (4.11)$$

$$\mathcal{H}_r(t) = \delta J(t) \mathbf{I}_A \cdot \mathbf{I}_B, \quad (4.12)$$

where  $\delta J(t) = J(t) - \bar{J}$ . The  $\Gamma$  matrix for this  $\mathcal{H}_r(t)$  is given as

$$\Gamma_{jk} = \text{Tr}\{[Q_j, \mathbf{I}_A \cdot \mathbf{I}_B][Q_k^\dagger, \mathbf{I}_A \cdot \mathbf{I}_B]\} \int_0^\infty (\langle J(0)J(t) \rangle - \bar{J}^2) d\tau. \quad (4.13)$$

The integral on the right hand side of this expression is the spectral density of the perturbation at zero frequency, and the angular brackets represent the ensemble-average autocorrelation function of the fluctuating scalar coupling. For a perturbation that is a scalar spin operator, only the spectral density at zero frequency enters. Moreover, since the perturbations have rovibrational correlation times short on the NMR timescale, this spectral density would be essentially constant over the (audio) range of frequencies appearing in the rotating frame energy level scheme. By comparing equation 4.13 with the phenomenological treatment of chemical exchange (Chapter 2), the chemical exchange rate  $k_J$  is identified as

$$k_J = \int_0^\infty (\langle J(0)J(t) \rangle - \bar{J}^2) d\tau. \quad (4.14)$$

For a system composed of two spins-1/2, the operator space is spanned by sixteen ( $2^{2N_s}$ ,  $N_s = 2$ ) basis vectors. Of these, eight correspond to magnetic dipole allowed

single quantum operators. The problem factors further by whether  $\Delta m = +1$  or  $-1$ . The calculations were performed for the  $\Delta m = +1$  transition. The  $\Delta m = -1$  case leads to identical results. The singlet-triplet basis discussed in Chapter 3 (equation 3.5) was used in all the calculations. The results are, however, independent of the choice of basis; which was checked by repeating the calculations in the simple product basis. The  $\Gamma$  and  $\Lambda$  matrices further factor in either basis into two  $2 \times 2$  blocks, one involving transitions with state  $|1_-\rangle$  and the other involving  $|1_+\rangle$ . The two matrices in the singlet-triplet basis are

$$(\Gamma - i\Lambda)_1 = \begin{array}{c} |1_-\rangle\langle 0_+| \quad |1_-\rangle\langle 0_-| \\ |0_+\rangle\langle 1_-| \left( \begin{array}{cc} -i\frac{(\nu_A + \nu_B)}{2} & -i\frac{(\nu_A - \nu_B)}{2} \\ -i\frac{(\nu_A - \nu_B)}{2} & -\frac{k_J}{2} - iJ - i\frac{(\nu_A + \nu_B)}{2} \end{array} \right) \\ |0_-\rangle\langle 1_-| \end{array} \quad (4.15)$$

and

$$(\Gamma - i\Lambda)_2 = \begin{array}{c} |0_+\rangle\langle 1_+| \quad |0_-\rangle\langle 1_+| \\ |1_+\rangle\langle 0_+| \left( \begin{array}{cc} -i\frac{(\nu_A + \nu_B)}{2} & i\frac{(\nu_A - \nu_B)}{2} \\ i\frac{(\nu_A - \nu_B)}{2} & -\frac{k_J}{2} + iJ - i\frac{(\nu_A + \nu_B)}{2} \end{array} \right) \\ |1_+\rangle\langle 0_-| \end{array}. \quad (4.16)$$

The signal for the initial condition  $I_x$  (corresponding to a  $(\frac{\pi}{2})_y$  preparation pulse) is obtained from these matrices by solving for the eigenvalues and eigenvectors, and is found to be

$$\begin{aligned} S(t) = & \frac{1}{4} \left[ \frac{\frac{c}{2} + sq}{sq} \exp\left(-\frac{(c + 2ia)}{2} + sq\right) t \right] \\ & - \frac{1}{4} \left[ \frac{\frac{c}{2} - sq}{sq} \exp\left(-\frac{(c + 2ia)}{2} - sq\right) t \right] \\ & + \frac{1}{4} \left[ \frac{\frac{c^*}{2} + sq^*}{sq^*} \exp\left(-\frac{(c^* + 2ia)}{2} + sq^*\right) t \right] \\ & - \frac{1}{4} \left[ \frac{\frac{c^*}{2} - sq^*}{sq^*} \exp\left(-\frac{(c^* + 2ia)}{2} - sq^*\right) t \right] \end{aligned} \quad (4.17)$$

where the following definitions have been used

$$\begin{aligned} c &= \frac{k_J}{2} + iJ \\ c^* &= \frac{k_J}{2} - iJ \end{aligned}$$

$$\begin{aligned}
sq &= \sqrt{c^2 - \left(\frac{\nu_A - \nu_B}{2}\right)^2} \\
sq^* &= \sqrt{c^{*2} - \left(\frac{\nu_A - \nu_B}{2}\right)^2} \\
a &= \frac{(\nu_A + \nu_B)}{2}.
\end{aligned}$$

The chemical exchange rate in the expression for the signal is given by equation 4.14; in the next section, a microscopic procedure for the calculation of  $k_J$  is outlined.

The calculation embodied between equation 4.11 and equation 4.14 appears to be a straightforward application of Redfield theory, and it is thus surprising that it is apparently not in the NMR literature. One reason is that, in the absence of tunnelling, scalar coupling between nearly isochronous spins is typically too small to be an important relaxation mechanism. The more subtle reason is that if this calculation is attempted in the most widely used interaction representation,[9, 10] in which the average chemical shift and scalar coupling are transformed away, the matrix element analogous to equation 4.13 becomes time-dependent and is hence discarded in lowest order. The present calculation shows that such “nonsecular”[9, 10] relaxation matrix elements are most easily calculated in the usual rotating frame, where this problem does not arise.

### 4.3 Master Equation

The ensemble-averaged autocorrelation of the tunnel splitting appearing in equation 4.14 for a system of discrete levels  $n$  with energies  $E_n$  and tunnel splittings  $J_n$  may be written as

$$\langle J(0)J(t) \rangle = \sum_{i,j} J_i p_i J_j c_i^j(t), \quad (4.18)$$

where the summation extends over all the levels,  $p_i$  is the equilibrium population of level  $i$ , and  $c_i^j(t)$  is the conditional probability of finding a particle in level  $j$  at time  $t$  given that at  $t = 0$  it was in level  $i$ . The  $c_i^j(t)$  are calculated by solving the master equation for the population of the rovibrational levels with appropriate initial conditions.

The master equation is a set of differential equations that describe the evolution of a physical system with time. For a system with  $N$  discrete levels, the master equation for a level  $i$  is given as

$$\frac{d}{dt}p_i = \sum_{j \neq i}^N k_{ji}p_j - \sum_{i \neq j}^N k_{ij}p_i, \quad (4.19)$$

where  $k_{ij}$  is the rate constant for population transfer from state  $i$  to  $j$ , while  $k_{ji}$  is the rate constant for population transfer from state  $j$  to  $i$ . The forward and backward rates  $k_{ij}$  and  $k_{ji}$  are related by the principle of detailed balance, which states that

$$k_{ij}\exp(-\beta E_i) = k_{ji}\exp(-\beta E_j). \quad (4.20)$$

In a vector form, the master equation for all levels is

$$\frac{d}{dt}\mathbf{p} = \mathcal{W}\mathbf{p}, \quad (4.21)$$

where  $\mathbf{p}$  is population column vector and  $\mathcal{W}$  has the form

$$\begin{pmatrix} -(k_{01} + k_{02} + \dots + k_{0N}) & k_{10} & \dots & k_{N0} \\ k_{01} & -(k_{01} + k_{12} + \dots + k_{1N}) & \dots & k_{N1} \\ \vdots & \vdots & \ddots & \vdots \\ k_{0N} & k_{1N} & \dots & -(k_{N0} + k_{N1} + \dots + k_{N(N-1)}) \end{pmatrix}.$$

A formal solution for the master equation can be written as

$$\mathbf{p}(t) = \exp(\mathcal{W}t)\mathbf{p}(0). \quad (4.22)$$

The time dependence of the population is solved for by diagonalising the  $\mathcal{W}$  matrix which reduces the problem to computing sums of exponentials. One of the eigenvalues of  $\mathcal{W}$  is necessarily zero, since population must be conserved in a closed system. For computational convenience, the  $\mathcal{W}$  matrix is converted into a symmetric form before diagonalisation. The transformation that performs this symmetrisation is given by

$$\mathcal{W}_s = \mathcal{P}^{-\frac{1}{2}}\mathcal{W}\mathcal{P}^{\frac{1}{2}}, \quad (4.23)$$

where  $\mathcal{P}$  is the population matrix.  $\mathcal{P}$  is a diagonal matrix whose diagonal elements are the normalised populations of the states.

The conditional probabilities required for the calculation of the autocorrelation function (equation 4.18) are determined from an assumed knowledge or model of the rates in equation 4.21 connecting the various rovibrational levels. In terms of the eigenvalues of  $\mathcal{W}$  ( $\lambda_k$ ) and the unitary matrix ( $\mathcal{U}$ ) that diagonalises  $\mathcal{W}$ , these conditional probabilities are given as

$$c_i^j(t) = \sum_k \mathcal{U}_{jk}^{-1} \mathcal{U}_{ki} \exp(-\lambda_k t). \quad (4.24)$$

This result is obtained by observing that the  $N$  different initial conditions for which the master equation must be solved can be represented by the  $N \times N$  identity matrix and that the solution to the master equation can be written as

$$\mathbf{p}(t) = \mathcal{U}^{-1} \exp(\Lambda t) \mathcal{U} \mathbf{p}(0). \quad (4.25)$$

### 4.3.1 Two State Model

As an illustrative example, the calculation of the autocorrelation function for a two-level system is outlined here, since analytic solutions can be obtained for this case. Consider the case of two tunnelling states with average energies 0 and  $E_1$ , with respective tunnel splittings  $J_0$  and  $J_1$ . The average value of the measured  $J$ -coupling according to equation 3.12 is given as

$$\langle J \rangle = \frac{J_0 + J_1 b}{1 + b} \quad (4.26)$$

where

$$b = \exp(-\beta E_1)$$

and  $1 + b$  is the partition function. The master equation for the populations of the two states is

$$\frac{d}{dt} \begin{pmatrix} p_0 \\ p_1 \end{pmatrix} = \begin{pmatrix} -k_{01} & k_{10} \\ k_{01} & -k_{10} \end{pmatrix} \begin{pmatrix} p_0 \\ p_1 \end{pmatrix}. \quad (4.27)$$

Imposition of detailed balance on the two rates implies that

$$\frac{d}{dt} \begin{pmatrix} p_0 \\ p_1 \end{pmatrix} = k_{10} \begin{pmatrix} -b & 1 \\ b & -1 \end{pmatrix} \begin{pmatrix} p_0 \\ p_1 \end{pmatrix}. \quad (4.28)$$

The eigenvalues of this matrix are  $-k_{10}(1+b)$  and 0. The latter eigenvalue results from the conservation of population for a closed system. The autocorrelation is then given as

$$\begin{aligned} \langle J(0)J(t) \rangle &= \frac{J_0}{1+b} \{J_0 [1 + \exp(-k_{10}(1+b)t)] + bJ_1 [1 - \exp(-k_{10}(1+b)t)]\} \\ &\quad + \frac{bJ_1}{1+b} \{J_0 [1 - \exp(-k_{10}(1+b)t)] + J_1 [b + \exp(-k_{10}(1+b)t)]\} \end{aligned}$$

which gives the spectral density at zero-frequency, i.e., the chemical exchange rate

$$k_J = \frac{b}{k_{10}(1+b)^3} (J_0 - J_1)^2. \quad (4.29)$$

#### 4.4 Discussion

Although the transition metal trihydrides that show exchange tunnelling are known to also show temperature dependent lineshapes,[6] there is only one compound for which such data have been reported in the literature.[14] The NMR lineshapes seen in the compound  $\text{Cp}^*\text{RuH}_3[\text{P}(\text{CHMe}_2)_3]$  over a range of temperatures are presented in Figure 4.1. The observed lineshapes were fit to classical models of chemical exchange and the kinetic parameters were extracted. An Arrhenius plot of the  $\ln k_{cl}$  vs.  $1/T$  gave an activation energy for the interconversion equal to 50 kJ/mol. For the same compound, the  $J$ -couplings were determined to be exponentially activated with an energy parameter of 6.8 kJ/mol.

The spatial model used in the fit reported here was a symmetric double well which was assumed to be harmonic with frequency  $\omega_0$ . The tunnel splittings of the excited vibrational states were assumed to be linearly dependent on the tunnel splitting of the ground state and exponentially dependent on the rovibrational quantum number and is given by the expression

$$J_n = p^n J_0. \quad (4.30)$$

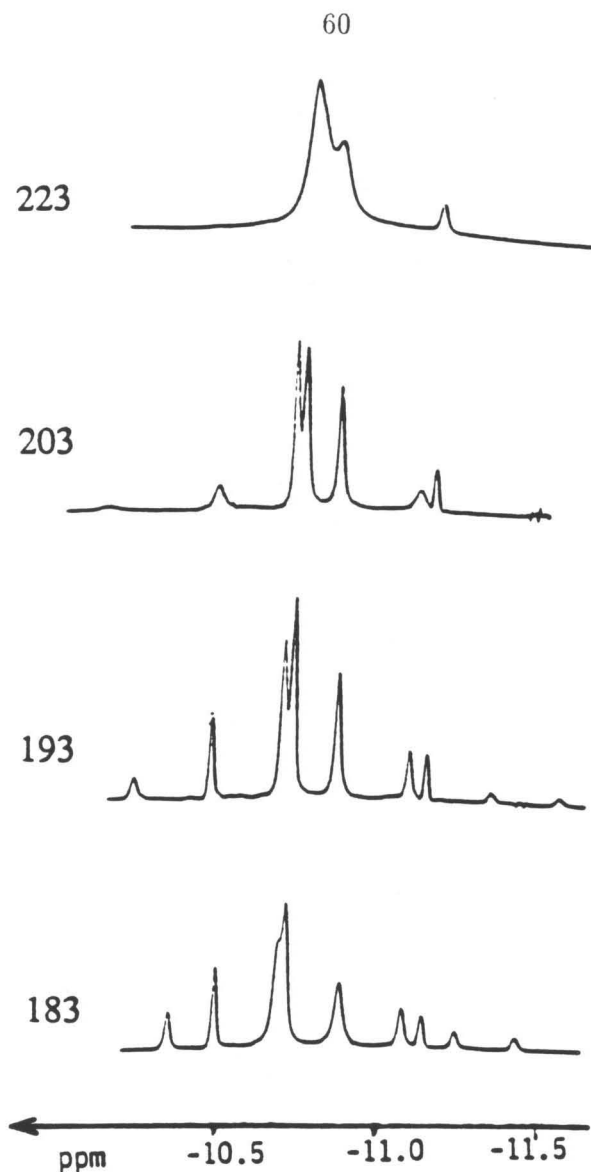


**Figure 4.1:** Temperature dependent lineshapes measured in  $\text{Cp}^*\text{RuH}_3[\text{P}(\text{CHMe}_2)_3]$  between 183–223 K. Reproduced from [14]

The tunnel splittings for states at or above the barrier were determined by the limiting case of the WKB expression

$$J_n = \frac{\omega_0}{\pi} \exp\left(-\frac{1}{\hbar} \int_{-a}^a \sqrt{2m(V(x) - E)} dx\right), \quad (4.31)$$

where  $-a$  and  $a$  are the classical turning points. A few simplifying assumptions were made in the choice of the parameters for the master equation. The large rate difference between the bath-induced transitions that induce spin-flips and those that do not allows for the former to be safely neglected in the calculations. The latter, on the other hand, are assumed to be independent of both spin and of the differences in the spatial state which are associated with the spin through the symmetrisation postulate. This is a necessary consequence of the step taken in equation 4.2 where a spatial number operator embodying different spin states was introduced. Much is gained in simplicity by making these approximations, since now there is a single rate parameter for each pair of spatial states. Due to thermal averaging on the NMR timescale the effect of rovibrational relaxation can be characterised by a single spectral density. Since nothing specific is known about the rovibrational relaxation, it is desirable to summarise it by a single parameter. A Landau-Teller [15, 16, 17] collision model for a harmonic ladder is used to characterise the relaxation rates. This implies that  $\Delta n = \pm 1$  and that

$$k_{n,n-1} = nk_{10}.$$

The upward rates are determined from the downward relaxation rates by the detailed balance condition.

The harmonic frequency and the ground-state tunnel splitting were varied by a grid-search algorithm until fits were obtained to the measured  $J$ -coupling. The  $p$  in equation 4.30 was chosen so as to approximately mimic the values of  $J_n$  observed in Chapter 3. The best fit to the  $J$ -coupling is presented in Figure 4.2. As in Chapter 3, the fitted parameter was the sum of the squares of the deviations between calculated and

experimental  $J$ -couplings at each temperature. For the potential parameters that led to a fit to the  $J$ -coupling data, the rate constants were calculated by the method discussed in the earlier sections. The only additional variable in these calculations is the relaxation time  $k_{10}$ . Best fits to the experimental data resulted when this relaxation time was 100 ps. A plot of the best fits to the rate data is also presented in Figure 4.2. The barrier height extracted from such a fit was 57 kJ/mol. For the fits obtained, there were nine states below the barrier, of which 7 states contributed 95% to the observed average scalar coupling at the highest temperature. On the other hand, the three states closest to the top of the barrier contributed 85% of the observed chemical exchange rate.

The spatial models used in this analysis were empirical and were picked to reduce the computational effort required to solve for the spatial eigenstates of one of the models discussed in Chapter 3. A more extensive analysis would require the solution of such spatial Schrödinger equations to obtain the spatial eigenvalues. The master equation treatment for the rovibrational populations must also be extended to treat the states of opposite symmetry separately and to incorporate the alternative averaging scheme discussed in Chapter 3.

It is of some historical interest that the problem of tunnelling effects on mutual chemical exchange was considered decades ago in the context of solid-state methyl groups.[18, 19, 20] These previous treatments have no theoretical basis and no resemblance to the present results, which have the familiar form of transport coefficients or rates typically derived in the context of the fluctuation-dissipation theorem.[21] The present result is intrinsically a property of a system of two or more particles and thus does not arise in the numerous theoretical studies of tunnelling effects on one particle dynamics.[1, 2]

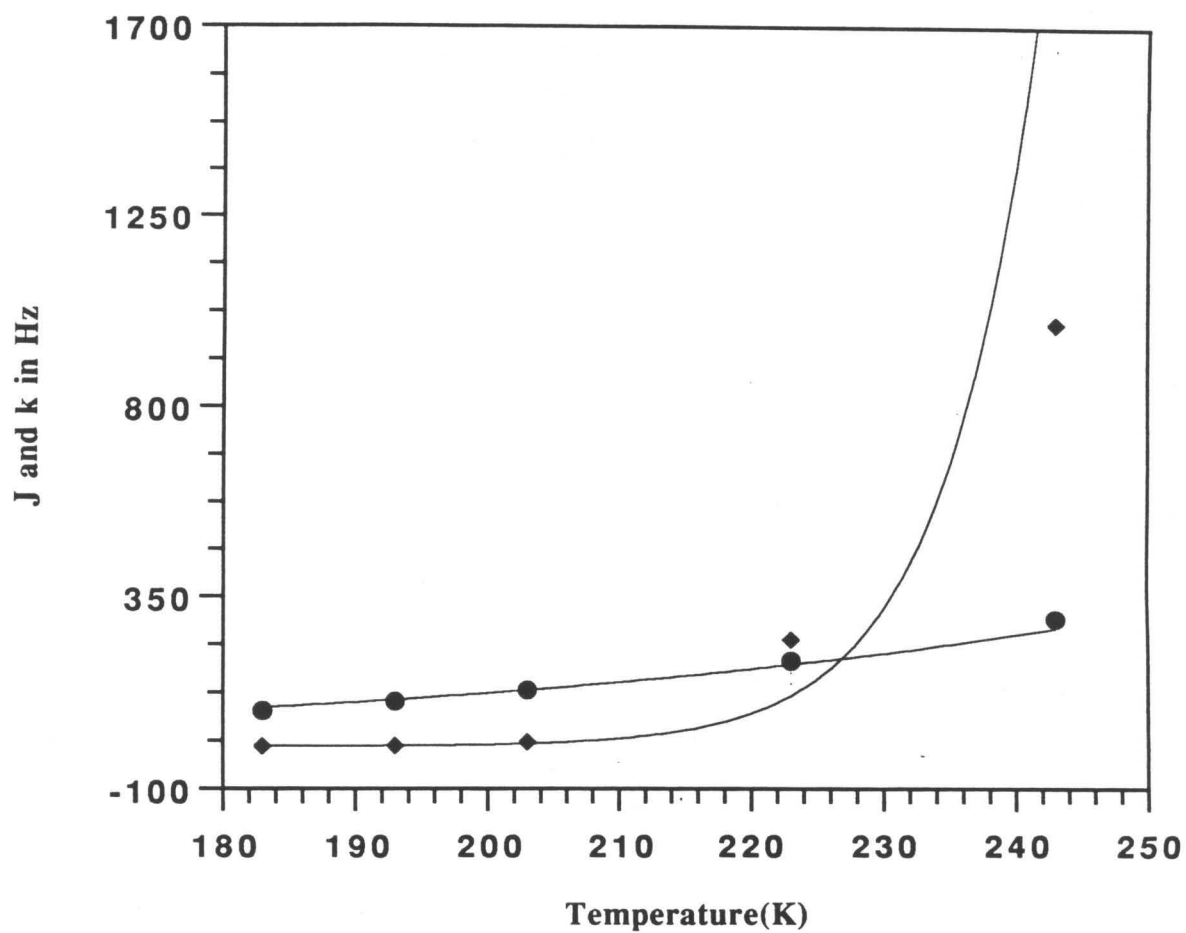


**Figure 4.2: Fit to chemical exchange rate and the  $J$ -coupling in  $\text{Cp}^*\text{RuH}_3[\text{P}(\text{CHMe}_2)_3]$ .** The chemical exchange rates fit are the rates obtained by fitting the lineshapes by classical methods (represented by  $\blacklozenge$ ). The  $J$ -coupling measured in experiments are represented by  $\bullet$ . The best fit parameters to both these data are represented by solid lines.

## 4.5 Conclusions

A method for treating systems where the NMR lineshapes reveal the presence of resolved tunnel splittings and chemical exchange has been presented. The method presented here provides a quantum-mechanical derivation of mutual chemical exchange, making no use of the concepts of transition state theory. The price paid is that, in the present form, the full complexity of the rovibrational relaxation must be modelled. It was shown via a Redfield analysis that the chemical exchange rate in this model corresponds to the low-frequency spectral density of the autocorrelation function of the fluctuating  $J$ -coupling. The fluctuation in the  $J$ -coupling was shown to arise from the fluctuation of the populations due to rovibrational relaxation, which was modelled here via a master equation. The one compound for which such experimental data are available was treated with the present model and yielded a physically reasonable barrier height but which was 14% higher than that obtained by a classical chemical exchange analysis.

The method presented here cannot be considered to have been put to a stringent test; a number of improvements still need to be made. For example, efforts are underway to incorporate the master equation approach presented here with the spatial models presented in Chapter 3.

## 4.6 References

- [1] A. J. Leggett, S. Chakravarty, A. T. Dorsey, M. P. A. Fisher, A. Garg, W. Zwerger, *Rev. Mod. Phys.*, **59**, 1 (1987)
- [2] P. E. Parris, R. Silbey, *J. Chem. Phys.*, **83**, 5619 (1985)
- [3] A. Stöckli, B. H. Meier, R. Kreis, R. Meyer, R. R. Ernst, *J. Chem. Phys.*, **93**, 1502 (1990)
- [4] R. Meyer, R. R. Ernst, *J. Chem. Phys.*, **93**, 5518 (1990)
- [5] C. R. Bowers, D. H. Jones, N. D. Kurur, M. G. Pravica, J. A. Labinger, D. P. Weitekamp, *Adv. Magn. Reson.*, **14**, 269 (1990)
- [6] K. W. Zilm, S. P. Neshyba, J. C. Duchamp, D. M. Heinekey, J. M. Millar, T. F. Koetzel, N. G. Payne, *J. Am. Chem. Soc.*, **112**, 920 (1990)
- [7] H. Dekker, *Mod. Phys. Lett. B*, **5**, 351 (1991)
- [8] A. Heuer, U. Haeberlen, *J. Chem. Phys.*, **95**, 4201 (1991)
- [9] A. G. Redfield, *IBM J. Res. Develop.*, **1**, 19 (1957)
- [10] A. G. Redfield, *Adv. Magn. Reson.*, **1**, 1 (1965)
- [11] N. D. Kurur, D. H. Jones, D. P. Weitekamp, *Proceedings of the 25th Ampere Congress on Magnetic Resonance and Related Phenomena (Stuttgart 1990)*, ed. M. Mehring, J. U. von Schutz, H. C. Wolf (New York: Springer-Verlag, 1990)
- [12] A. Abragam, *Principles of Nuclear Magnetism* (Oxford: Oxford University Press, 1961)
- [13] R. A. Hoffman, *Adv. Magn. Reson.*, **4**, 87 (1970)

- [14] T. Arliguie, C. Border, B. Chaudret, J. Devillers, R. Poilblanc, *Organometallics*, **8**, 1308 (1989)
- [15] L. D. Landau, E. Teller, *Physik. Z. Sowjetunion*, **10**, 34 (1936)
- [16] R. J. Rubin, K. E. Shuler, *J. Chem. Phys.*, **25**, 59 (1956)
- [17] E. W. Montroll, K. E. Shuler, *J. Chem. Phys.*, **26**, 454 (1957)
- [18] E. O. Stejskal, H. S. Gutowsky, *J. Chem. Phys.*, **28**, 388 (1958)
- [19] S. Clough, A. Heidemann, A. J. Horsewill, J. D. Lewis, M. N. J. Paley, *J. Phys. C*, **15**, 2495 (1982)
- [20] C. S. Johnson, C. Mottley, *Chem. Phys. Lett.*, **22**, 430 (1973)
- [21] F. Reif, *Fundamentals of Statistical and Thermal Physics* (New York: McGraw-Hill, 1965)

**Part II**

**NMR of Semiconductors**

## Chapter 5

# Introduction

Magnetic resonance, especially nuclear magnetic resonance, is one of the foremost structural tools available today and provides information on both electronic structure and nuclear positions. Magnetic resonance fails, however, in situations where low concentrations have to be detected due to its low sensitivity arising as a result of the small energy quantum that is involved. One field where the applicability of the technique has been hampered by the low sensitivity is in the identification and characterisation of defects in semiconductors. In solids, an added complication is the featureless line that is usually obtained as a result of the magnetic coupling of the nuclei through space and from which only limited structural information is available. This part of the thesis is concerned with the development of two magnetic resonance methods aimed at the characterisation of defects in semiconductors.

### 5.1 Outline

Electron nuclear double resonance (ENDOR) is a method of measuring NMR transitions by detecting the ESR signal. Since its introduction it has been extensively used to study paramagnetic impurities and defects in semiconductors and other solids. Hyperfine couplings measured by ENDOR are more accurate than those measured from ESR data due to the better resolution of the former technique. In Chapter 6 it is demonstrated that the resolution achievable with ENDOR can be improved by at least three orders of magnitude. Chapter 6 discusses a theoretical study that combines a variety of multiple-pulse

techniques to selectively switch on and off different nuclear spin interactions between different sites to measure dipolar couplings between these sites. Since dipolar couplings between nuclei are dependent on the distance between them quantitative structural information is obtainable by this method. The technique is illustrated by simulations of an experiment which would resolve a controversy regarding the site assignments of some lines seen by conventional ENDOR on crystalline silicon dilutely doped with phosphorous.

Chapter 7 describes an experimental investigation with a new optical method for high-sensitivity and high-resolution NMR of defects in GaAs semiconductors. A Fourier transform method of time-sequenced optical NMR is introduced and its advantages discussed. This technique has greater sensitivity to spins near an optically relevant defect than does an earlier continuous wave variant.

## Chapter 6

# Resolution-Enhanced Electron Nuclear Double Resonance

Since the introduction of electron nuclear double resonance (ENDOR) three decades ago,[1] it has been recognised that the resonance frequencies of the nuclei in the vicinity of a dilute localised unpaired electron provide a spectroscopic window on the structure of such sites. In almost all cases,[2, 3] the quantitatively useful information obtained from ENDOR or the related near-nucleus magnetic resonance (NNMR)[4] is a list of hyperfine couplings between the unpaired electrons and the various spectroscopically resolved, magnetically inequivalent nuclear sites, typically those within several atomic spacings from the paramagnetic centre. In a few favourable cases,[5] some additional structure due to a dipolar coupling between neighbouring nuclei is resolvable. Typically, however, the ENDOR or NNMR line within an electronic manifold is an unresolved band some kilohertz in width, from which no individual dipolar couplings can be extracted. The resolution is limited by the dipole-dipole interaction[6, 7] to the large number of neighbours around a site.

Over the years ENDOR was primarily done in a continuous-wave(CW) fashion. The situation has changed in recent years, with pulsed ENDOR[8, 9, 10, 11] becoming more popular. A few simple sequences for pulsed ENDOR have been added, and a wealth of sequences can still be “invented.” Such sequences for the measurement of individual dipolar couplings between nuclei in the vicinity of paramagnetic sites in solids are described

in this chapter. The methods proposed here extend multiple-pulse techniques used in the study of diamagnetic solids to paramagnetic systems, hence affording significant enhancement in the resolution of ENDOR spectra. The technique is called Resolution-Enhanced Electron Nuclear DOuble Resonance(RE-ENDOR).

## 6.1 Electron Nuclear Double Resonance

ENDOR is a classical double resonance technique and is performed by applying microwave and rf fields in a CW fashion. The first ENDOR experiments were applied to solids, but recently the applications have been predominantly in liquids. ENDOR has advantages over both ESR and NMR. It is more sensitive than NMR since the higher energy microwave photon is detected. On the other hand, it has better resolution and fewer lines than ESR. For example, an electron,  $S = 1/2$ , coupled to  $N$  nuclei gives  $2^N$  ESR lines as opposed to  $2N$  ENDOR lines.

A brief introduction to ENDOR is provided here for completeness. An electron ( $S = 1/2$ ) coupled to a nuclear spin ( $I = 1/2$ ) serves as the example. The four possible levels are shown in Figure 6.1. The electronic wavefunctions are denoted by  $\alpha_e$  and  $\beta_e$  while the nuclear wavefunctions are represented by  $\alpha_n$  and  $\beta_n$ . ESR transitions (indicated by dotted arrows) connect levels 1 to 3 and 2 to 4. Levels 1 and 2 are connected by an NMR transition; so are levels 3 and 4. A steady-state version of the experiment is discussed here. The experiment involves saturating the ESR transition 2-4. Application of a saturating rf field at the 3-4 NMR transition frequency leads to a change in the population of level 4 and hence to an increase of the ESR signal which had been earlier saturated. This change in intensity of the saturated ESR transition is called the ENDOR effect. A similar effect is seen when the rf corresponds to the 1-2 transition frequency. An ENDOR line is hence the NMR spectrum of a nucleus within a particular electron spin manifold.

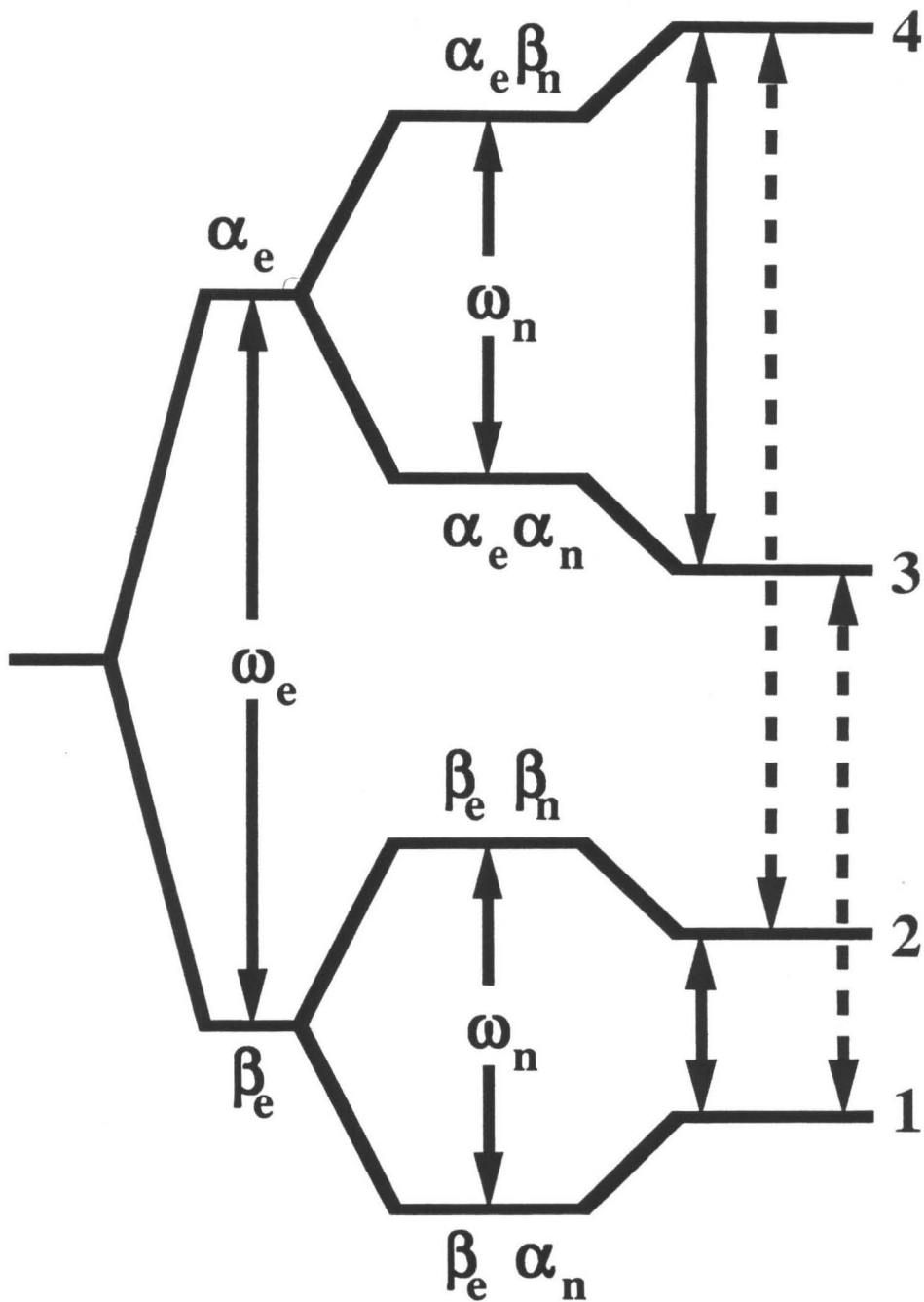


**Figure 6.1:** An electron  $S=1/2$  coupled to a nucleus  $I=1/2$ . The electron levels are  $\alpha_e$  and  $\beta_e$ , while the nuclear levels are  $\alpha_n$  and  $\beta_n$ . The NMR transitions connect levels 1-2 and 3-4. The ESR transitions connect levels 1-3 and 2-4.

The ENDOR Hamiltonian can be represented by

$$\mathcal{H}_{\text{ENDOR}} = \mathbf{B}_0 \cdot \mathbf{g} \cdot \mathbf{S} + \mathbf{I} \cdot \mathcal{A} \cdot \mathbf{S} - g_n \beta_n \mathbf{B}_0 \cdot \mathbf{I}. \quad (6.1)$$

Later in the chapter a more complete form is used for this Hamiltonian. The form 6.1 is more typical of the ENDOR literature. The first term in the Hamiltonian is the Zeeman interaction between the electronic spin  $\mathbf{S}$  and the applied magnetic field  $\mathbf{B}_0$ . The second term is the hyperfine interaction between the nuclear spin  $\mathbf{I}$  and the electron spin, and the last term represents the nuclear Zeeman interaction. The tensors  $\mathbf{g}$  and  $\mathcal{A}$  describe the Zeeman and hyperfine interactions and  $g_n$  and  $\beta_n$  are the nuclear  $g$  factor and the nuclear magneton. For a system of many nuclei coupled to the same unpaired electron, terms similar to the last two in equation 6.1 are present for each nucleus.

In an ENDOR experiment, the transitions  $\Delta m_I = \pm 1$  are induced for the various nuclear spins. In the high-field limit the various ENDOR frequencies are given by

$$\omega_{\text{ENDOR}} = |\gamma_n \mathbf{B}_0 \pm \frac{1}{2} \hat{\mathbf{n}} \cdot \mathcal{A} \cdot \hat{\mathbf{n}}|. \quad (6.2)$$

Here  $\hat{\mathbf{n}}$  is a unit vector in the direction of the magnetic field and  $\gamma_n \hbar = g_n \beta_n$  is the magnetogyric ratio of the nucleus. From equation 6.2 it is seen that the spectrum is symmetric about  $\gamma_n B_0$ .

The  $\mathcal{A}$  tensor can be decomposed into a scalar  $a$  and a traceless tensor  $\mathcal{B}$ . These quantities are defined as

$$a \equiv \frac{1}{3} \sum_{i=1}^3 A_{ii} \quad (6.3)$$

$$B_{ij} \equiv A_{ij} - a \delta_{ij}. \quad (6.4)$$

The scalar term arises from the Fermi contact interaction and is given by

$$a = \frac{8\pi}{3} g \beta g_n \beta_n |\psi(\mathbf{r})|^2,$$

where  $\psi(\mathbf{r})$  is the spatial part of the electronic wavefunction at the site of the nucleus. The  $\mathcal{B}$  tensor on the other hand arises as a result of the direct dipolar interaction between the

electron and the nucleus. Thus a wavefunction calculated theoretically must be able to reproduce the values of the hyperfine coupling determined from an ENDOR experiment.

In practice, the ENDOR spectrum is determined for various orientations of the sample with respect to the magnetic field. The angular variation of the frequencies show regular patterns arising as a result of the regular geometric arrangement of the nuclei around the paramagnetic site. The  $\mathcal{A}$  tensor, whose characterisation is the goal of ENDOR experiments, is determined from a knowledge of the angular variation of the ENDOR frequencies.

An important characteristic of ENDOR lines is their shape. Typically, an ENDOR line is an unresolved band some kilohertz in width and from which no individual dipolar coupling can be extracted. Only in a few favourable cases has some additional structure due to dipolar coupling between neighbouring nuclei been resolvable.[5, 12, 13] The linewidths are limited by dipolar couplings with the large number of neighbours around a site. For experiments performed in a CW fashion, a number of extraneous instrumental factors affect the linewidth.

## 6.2 Resolution-Enhanced ENDOR (RE-ENDOR)

The basis of the proposed method is the judicious use of multiple pulse rf sequences that average most of the interactions to zero, while leaving a small subset to give rise to a resolved spectrum. Two general classes of experiments are needed to fully characterise the various dipolar couplings between nuclei in the neighbourhood of a paramagnetic centre. The first class measures the couplings between nuclei whose transition frequencies fall within the same band, while eliminating the coupling between these nuclei and those in other bands. The other class measures the couplings within a particular electronic manifold between nuclei in two different bands, while eliminating the couplings between nuclei within each of these bands and the couplings from these nuclei to those in all other

bands. In analogy to the terminology in ordinary NMR the first class is referred to as homonuclear experiments while the second set is referred to as heteronuclear. The difference between the situation encountered in diamagnetic solids and the present situation is that nuclei with the same magnetogyric ratios may in effect be heteronuclei due to differences in the hyperfine couplings much greater than their mutual dipolar couplings.

### 6.2.1 General Timing Diagram

The general scheme of the RE-ENDOR experiment consists of five periods as shown in Figure 6.2. The first and the last periods, called pumping and detection respectively involve resonant irradiation of the electron spins. The intervening preparation, evolution and mixing periods are analogous to those that are routinely used in 2D NMR experiments[14] and involve only nuclear spin irradiation. The overall scheme is a combination of time-domain or “coherence transfer” [8, 9, 10, 11] ENDOR with various techniques of high resolution solid-state NMR.

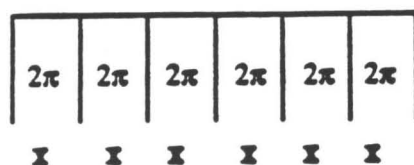
During the pumping period electron spin irradiation partially saturates some part of the spectrum. This in turn creates nonequilibrium nuclear spin populations which are then subjected to a series of rf pulses during the following three periods. Usually the preparation and mixing periods are identical or at least similar. In the simplest case, which suffices here, both of these periods are made up of a single  $\frac{\pi}{2}$  pulse. The evolution period,  $t_1$ , the point of concern here, can contain different rf pulse sequences, two of which are shown in Figure 6.2 and discussed below. The  $t_1$  modulated information of the nonequilibrium nuclear spin population created during the pumping period is monitored by its effect on the ESR signal in the detection period. Repetition with incrementation of  $t_1$  and Fourier transformation with respect to this dimension leads to the resolution-enhanced spectrum.

## a) Timing Diagram



## b) Evolution Period Sequences

### 1. Nutation



### 2. Phase shifted $\Pi$ -train

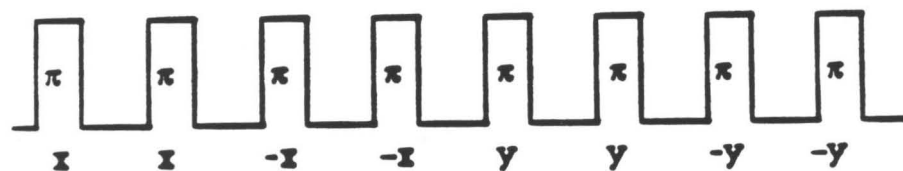


Figure 6.2: a) **Timing diagram** for resolution-enhanced ENDOR. Pumping and detection periods involve irradiation of the electron spins. The other three periods are similar to those used in routine 2D experiments. b) **Evolution period multiple-pulse sequences investigated**. The evolution period sequences for the determination of the measurement of homonuclear coupling.

### 6.2.2 The Hamiltonian and the Observables

In order to discuss the additional information available from RE-ENDOR, it is necessary to introduce additional spin interactions that are usually negligible in ENDOR analysis. To demonstrate the fact that individual dipolar couplings between nuclei close to a paramagnetic site can be measured, calculations were performed with high-field rotating-frame Hamiltonian of the form

$$\begin{aligned} \mathcal{H}^e = & \left( \sum_j \mathcal{H}_{S_j}^e + \sum_k \mathcal{H}_{I_k}^e + \right. \\ & \sum_{j < j'} \mathcal{H}_{S_j S_{j'}}^e + \sum_{k < k'} \mathcal{H}_{I_k I_{k'}}^e + \sum_{j < k} \mathcal{H}_{S_j I_k}^e + \\ & \left. \mathcal{H}_{rf} \right) |e\rangle\langle e|. \end{aligned} \quad (6.5)$$

The label  $e$  indicates those degrees of freedom that do not change during the period of nuclear irradiation. It is comprised of the electronic state, including spin, and, in some cases, certain nuclear degrees of freedom that are far from resonance and whose coupling may be treated as an “inhomogeneous” effect. When such nuclear states are included in  $|e\rangle$ , the responses are formally summed over all possible such states, since the subspectra due to each are not generally resolvable. The goal is to show that their influence can be removed as a line broadening contribution. Once this is accomplished, they are irrelevant degrees of freedom and explicit summation is unnecessary. The label  $I$  refers to spins in the irradiated band, while  $S$  refers to all other nuclei in the system not included in  $|e\rangle$ . The single spin terms particular to the individual nuclei are

$$\mathcal{H}_{I_k}^e = -(\omega_{zk}^{e,I} + a_{zk}^{e,I} + d_{zk}^{e,I}) I_{zk} \quad (6.6)$$

$$= -\Omega_{zk}^{e,I} I_{zk}, \quad (6.7)$$

where  $\omega_{zk}^{e,I}$  is the chemical shift of the  $k^{\text{th}}$   $I$  spin in electronic state  $|e\rangle$ ,  $a_{zk}^{e,I}$  is the corresponding hyperfine shift and  $d_{zk}^{e,I}$  is the shift due to the dipolar local field of the nuclear states included in  $|e\rangle$ , if any. Exactly analogous terms comprise  $\mathcal{H}_{S_j}^e$ . The

coupling terms have the form

$$\mathcal{H}_{S_j I_k}^e = -D_{S_j I_k}^e (3S_{zj}I_{zk} - \mathbf{S}_j \cdot \mathbf{I}_k) \quad (6.8)$$

and similarly for  $\mathcal{H}_{S_j S_{j'}}$  and  $\mathcal{H}_{I_k I_{k'}}$ . For the heteronuclear case, where the  $I$  and  $S$  resonances are separated by differences

$$(\Omega_{zj}^{e,S} - \Omega_{zk}^{e,I}) \gg D_{S_j I_k}^e$$

a doubly rotating frame, where the heteronuclear flip-flop terms are truncated, was employed. In the homonuclear case, this additional approximation is avoided, thus implicitly including the possibility that terms of order

$$\frac{D_{S_j I_k}^e}{(\Omega_{zj}^{e,S} - \Omega_{zk}^{e,I})}$$

contribute to the response of the  $I$  spins. Similarly, the coupling of the system to the applied radiation field is

$$\mathcal{H}_{rf} = -\omega_p \left( \sum_j S_{\phi j} + \sum_k I_{\phi k} \right) - \Delta\omega^S \sum_j S_{zj} - \Delta\omega^I \sum_k I_{zk}, \quad (6.9)$$

where  $\omega_p = \gamma B_1$  is the on-resonance nutation frequency,  $\phi$  indicates the phase of the rf and  $\Delta\omega^I = (\omega_0^I - \omega)$  and  $\Delta\omega^S = (\omega_0^S - \omega)$  is the difference between the reference Larmor frequency,  $\omega_0 = \gamma B_0$ , and the applied frequency,  $\omega$ . The possibility of interaction with the radiation field is included for all spins not explicitly included in  $|\epsilon\rangle$ , though for the homonuclear single-resonance case those labelled as  $S$  spins will in practice be only weakly affected, since their hyperfine splittings set them off-resonance. The offset  $\Delta\omega$  is chosen so that one hyperfine satellite band is near resonance in the sense  $\omega_p \gg (\Omega_{zk}^{e,I} + \Delta\omega)$ . This condition can be met for two or more spins  $I_k$  when the spins are magnetically equivalent or when they are made nearly isochronous at a particular crystal orientation by taking advantage of the anisotropy of the hyperfine couplings  $a_{zk}^{e,I}$ .

The spectra are calculated in the time domain using a numerical implementation of the unitary evolution of the density operator of the  $I$  and  $S$  spins. The program

used for these calculations is discussed in greater length in Appendix C. The rf pulses described are taken as square, so the rotating-frame Hamiltonian is piecewise constant and is diagonalised at each step for the rf field strength at that time. The complex signal is assumed to be of the form

$$S^e(t) = \text{Tr}[(U_e(t)\rho(0)U_e^\dagger(t) | e\rangle\langle e | (I_+ + S_+)]. \quad (6.10)$$

where  $(I_+ + S_+) = (I_x + S_x) + i(I_y + S_y)$  is the observable for the two transverse components of the spin angular momenta contributing to the hyperfine satellites of interest and  $U_e(t)$  is the propagator derived from the Hamiltonian (equation 6.5). The initial condition is

$$\rho(0) = b | e\rangle\langle e | (S_z + I_z) \quad (6.11)$$

and the trace operation is performed over the space spanned by the  $I$  and  $S$  spins. The inclusion of  $S$  spins in the initial conditions and in the observable is for the homonuclear experiments actually only a precaution; it allows for the numerical confirmation that only slight evolution occurs in this subspace as a result of pulse sequences centred at the  $I$  resonances. In the heteronuclear case the  $S$  operators are absent in the detection; i. e., detection is only at the  $I$  frequency. In a coherence transfer ENDOR experiment, the nuclear spin evolution period stands between two periods of irradiation at electron spin transitions and ends with a pulse to store the nuclear spin coherence as population differences. In this way one component of the transverse nuclear magnetisation within an electronic state is detected indirectly as changes in the ESR signal. Since all the spectra calculated here are symmetric about their centres, only one observable is necessary and the formalism will equally well describe the ENDOR or NNMR signals. Initial conditions other than that of equation 6.11 (multipolar order) could occur in either case depending on the details of the preparation. This would effect relative line intensities, but not the resolution of primary interest here. Thus these less common initial conditions are set aside.

## 6.3 Isolating Couplings

### 6.3.1 Homonuclear Case

This spectroscopic situation is closely analogous to the situation encountered in the solid-state NMR of small clusters of one nuclear species coupled to many nuclei of another species. The straightforward approach is decoupling the heteronuclei by irradiation at their transition frequency.[5] This is of little use in the present context, since the diverse hyperfine couplings of the heteronuclei will typically spread their transitions over many different bands making intense irradiation of all neighbours impractical. A more applicable approach is nutation spectroscopy,[15] which has been demonstrated, for example, on  $^{13}\text{C}$ - $^{13}\text{C}$  pairs in protonated molecules.[16] Recently,[17] transient nutations within the nuclear sublevels in an electron-nuclear system was indirectly detected through the polarisation of the electron spins. The method was shown to be useful for counting the number of equivalent nuclear spins in ENDOR spectroscopy. However, in that study dipolar couplings between nuclear spins were neglected.

Nutation of the spin magnetisation by intense resonant irradiation has the effect of eliminating heteronuclear couplings and chemical shifts, while retaining the homonuclear coupling scaled by a factor of  $-1/2$ . Two drawbacks of nutation spectroscopy are that it requires high peak power, if it is to be used without additional irradiation at the nuclei to be decoupled. The rf homogeneity requirements are stringent if sufficiently high resolution is to be achieved. These requirements are more stringent in single crystals than in powders, since the continuous distribution of orientations in the latter samples reduces the attainable resolution in any case.

An alternative to the single-phase nutation experiment is to give a train of phase-shifted  $\pi$  pulses to the spins of interest. The  $\pi$  train reduces both the power and the rf homogeneity requirements needed for a given resolution. If the duty ratio is low, the resolution achievable with the  $\pi$  train is better than for the nutation experiment. This is

because the average Hamiltonian for the  $\pi$  train is not scaled down during the windows and is scaled by  $1/4$  on average over the pulses, while in the nutation case the Hamiltonian is scaled by a factor of a  $1/2$ .

### 6.3.2 Heteronuclear Case

For a system of  $N$  spins coupled to one  $S$  spin, there are  $N$  heteronuclear couplings, but  $N(N-1)/2$  homonuclear ones. This implies that the heteronuclear spectra are greatly simplified and consequently have less total information. However, this lost information is reobtainable if the  $S$  spins are randomly distributed. Pulse sequences to extract the heteronuclear coupling constants in solids,[18, 19, 20] while observing either  $I$  or  $S$  spins, are known. All these sequences eliminate the homonuclear terms to increase the resolution or measurement of the Zeeman and heteronuclear terms. The SHRIMP sequence [20] was employed in this study and involves irradiating both the  $I$  and  $S$  spins with the same sequence of  $\pi/2$  pulses. This method has the advantage over other sequences for dipolar measurements in that Zeeman terms are completely removed and dipolar scaling is minimised. The  $I$  spin spectrum of an  $IS_N$  system for the SHRIMP sequence is  $N$  pairs of lines, the separation between each pair being  $4D/3$ . On the other hand, the separation for the other sequences is only  $2D/\sqrt{3}$ . This implies greater resolution with SHRIMP than with the other sequences.

## 6.4 Results and Discussion

### 6.4.1 Phosphorous Donor in Silicon

The original ENDOR[1] experiments were performed on the  $^{31}\text{P}$  resonances of dilutely doped phosphorous in crystalline silicon and subsequently the  $^{29}\text{Si}$  ENDOR of this site was intensively studied by CW techniques.[3]

Silicon crystallises in a face-centred cubic lattice with lattice constant  $5.4307 \text{ \AA}$ (Figure

6.3). From previous ENDOR studies it is known that phosphorous is a substitutional impurity. Without loss of generality, its position is chosen as the origin (cross hatched in Figure 6.3). The  $^{29}\text{Si}$  nuclei around the donor form a series of neighbour shells. The large number of shells fall into four distinct classes as a result of  $T_d$  symmetry around the impurity. From a detailed analysis of ENDOR data, previous workers have determined hyperfine coupling constants and also made site assignments for a large number of lines. Many of the assignments are, however, controversial.[21] It is demonstrated here that line-narrowing sequences will allow the measurement of individual dipolar couplings of less than 100 Hz from ENDOR lines which are 2–3 kHz wide in ordinary ENDOR. This allows unambiguous assignment of the hyperfine couplings and measurement of the lattice distortion around the dopant.

The numerical calculations were performed on a typical  $^{29}\text{Si}$  ENDOR line, in this case the D line. Onffroy[21] has assigned this line to the (2,2,4) shell while Ivey and Mieher[22] claim that it arises from the (3,3, $\bar{7}$ ) shell. Both of these shells belong to the [110] plane class and hence there are 12 equivalent sites in each shell. The 12 sites form two magnetically inequivalent sets of 4 (solid atom in Figure 6.3) and 8 (hatched atoms in Figure 6.3) respectively, when the magnetic field is along the [001] or crystallographic  $c$  axis. All computations were done on the high frequency D line for the above mentioned field orientation. The line was chosen for two reasons: there exists a controversy in the literature regarding the site assignment and, for the chosen magnetic field orientation, it is well-resolved.

#### 6.4.2 Linewidths

The second moment for a system composed of two magnetic species is given by the Van Vleck formula[23, 24]

$$M_2^I = \frac{1}{3} \gamma_I^4 \hbar^2 f \sum_{j < k} b_{jk}^2 + \frac{1}{3} \gamma_I^2 \gamma_S^2 \hbar^2 f' \sum_{j < k'} c_{jk'}^2 \quad (6.12)$$

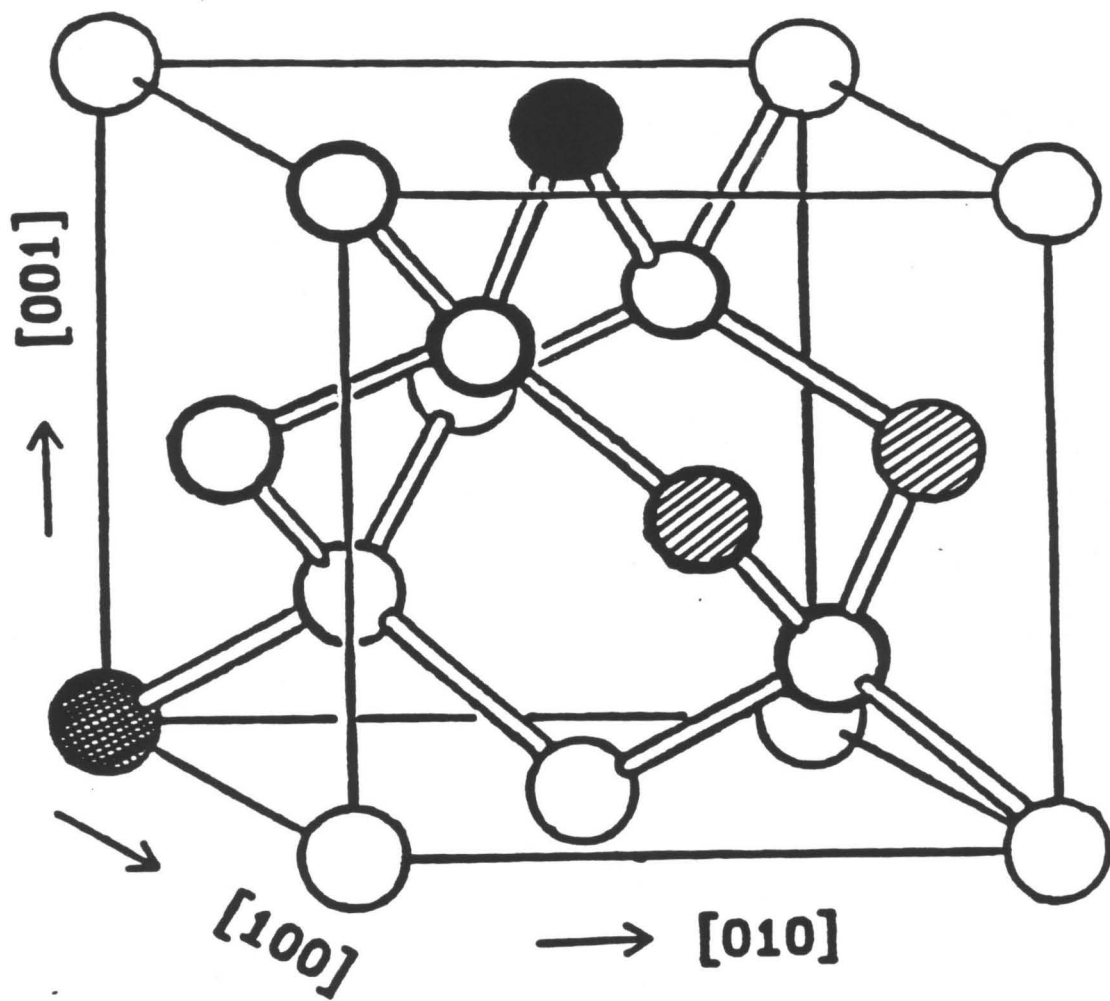


**Figure 6.3: Unit cell of silicon.** The cross-hatched atom at the origin is the substitutional impurity phosphorous. The magnetically inequivalent sets of nuclei in the [110] plane class are labelled. There are 8 equivalent hatched atoms and 4 equivalent solid atoms.

where  $b_{jk}$  and  $c_{jk'}$  have the form

$$b_{jk} = \frac{3(1 - 3\cos^2\theta_{jk})}{2r_{jk}^3} \quad (6.13)$$

$$c_{jk'} = J_{jk'} + \frac{(1 - 3\cos^2\theta_{jk'})}{r_{jk'}^3}. \quad (6.14)$$

The first term in the second moment is the homonuclear contribution for the spin  $I$  with magnetogyric ratio  $\gamma_I$  while the second term is the heteronuclear contribution. The magnetogyric ratio of the  $S$  spins is  $\gamma_S$ . The angles  $\theta_{jk}$  and  $\theta_{jk'}$  are between the vectors  $\mathbf{r}_{jk}$  and  $\mathbf{r}_{jk'}$  and the applied magnetic field. The pure exchange term  $J_{jk'}$  contributes to the second moment only in the heteronuclear case. The summation with respect to  $k'$  is over all the heteronuclei, and in this particular case will include the P and the hyperfine shifted Si. The natural abundances of the magnetically active nuclei are represented by  $f$  and  $f'$ .

The square root of the second moment for the D line was found to be 40 Hz. As already mentioned, the observed lines are 2–3 kHz wide, demonstrating that other sources of linebroadening dominate. In metals, linewidths much bigger than can be accounted for purely by dipole interactions have been seen and rationalised[25, 26] as arising from indirect exchange between the nuclei, mediated by the conduction electrons. No estimate of indirect exchange in Si semiconductors exists in the literature. The  $J$  coupling between directly bonded silicon atoms in isolated molecules may be a reasonable model for this indirect exchange, since at low temperatures, the conduction band is unoccupied. Inclusion of indirect exchange in the form of a  $J$  coupling only changed the calculated linewidth by about 10%.

The linewidth calculated on the basis of nuclear spin interactions is thus orders of magnitude smaller than what is observed in practice. The observed linewidths must be due to other factors. Line broadening could arise as a result of inhomogeneity in the wavefunction of different donor centres as a result of strain.[27, 28] In imperfect crystals, another potential source of broadening is the anisotropic part of the wavefunction. In

either case such effects will be eliminated from the RE-ENDOR linewidth just as Zeeman terms are. In the CW version, artifacts of the experimental technique such as power broadening and sweep rate could also contribute to the observed linewidth, but are irrelevant to the time-domain RE-ENDOR method. In summary, the sequences delivered during the RE-ENDOR evolution period should eliminate any plausible source of the ENDOR linewidth.

## 6.5 Numerical Calculations

The fact that the natural abundance of  $^{29}\text{Si}$  is only 4.67% makes the calculations easier in that the possibility of large clusters of coupled spins can be neglected. Thus computing time is practical with straightforward matrix mechanics. However, a summation is needed over many such calculations weighted by the statistical probability of different configurations of  $^{28}\text{Si}$  and  $^{29}\text{Si}$  nuclei.

The calculations for the measurement of the homonuclear dipolar couplings that follow were performed for the  $\pi$  train at a nutation frequency of 100 kHz. At this rf power the  $S$  spin is effectively decoupled, as established by worst case sample calculations, thus allowing the omission of the  $S$  spins from the bulk of the calculations. The number of  $I$  spins involved in the calculations varied from one to five. Calculations with three or more spins were found to be unnecessary since the statistical summation of such spectra showed measurable contributions only from one and two spins. The spectra from higher spin numbers do not significantly contribute to the summed spectra since the intensity is spread out over many lines and the probability of occurrence at natural abundance of large numbers of  $^{29}\text{Si}$  is very low. The weighting factor,  $w$ , in the statistical summation is given by

$$w = \sum_{i=0}^{s-n} \binom{s}{i} (0.0467)^{i+n} (0.9533)^{s-(i+n)}. \quad (6.15)$$

Here  $n$  is the number of  $I$  spins in the calculation and  $i$  the number of  $S$  spins. The first

term represents the combinatorial term that determines the number of ways  $i$  spins of the  $S$  type can be picked out of a possible  $s$  sites. The other numerical factors are the natural abundance of  $^{29}\text{Si}$  and  $^{28}\text{Si}$  respectively. Any  $S$  spin with a dipolar coupling  $\geq 20$  Hz was initially included in fixing the number of sites  $s$ . It was found that the statistically summed spectra did not change appreciably when  $s$  varied from 0 to 100 demonstrating that all heteronuclear sites were in fact decoupled. For larger values of  $s$  the probability of occurrence of large numbers of  $^{29}\text{Si}$  is higher and calculations cannot be restricted to 5 or fewer spins, but calculation of worst case systems with up to 5 spins showed that decoupling was adequate given the 10 Hz linewidth associated with apodising the time domain data. This value is a conservative estimate of that linewidth expected from various pulse errors in multipulse NMR experiments.

The summed spectrum for the (2,2,4) assignment of the D line is shown in Figure 6.4 a). As mentioned earlier, the major contribution to the signal is from single  $I$  spins. The only other significant contribution is from pairs of  $I$  spins, which give rise to the familiar Pake doublet. The ratio of the peak heights arising from the single spin to that due to two spins is rigorously correct for NMR, but approximate for ENDOR. This is because electron spin irradiation during the pumping period creates other than Zeeman order.[17] With the pulse sequence proposed these terms in the initial condition contribute to the line at the single spin frequency.

The key feature of the summed spectrum is that by eliminating inhomogeneity terms and heteronuclear couplings, resolved homonuclear features may be observed at 10 Hz resolution. This is comparable to that obtained in multiple-pulse line narrowing on diamagnetic solids and is at least two orders of magnitude better than the observed ENDOR linewidths, and provides an entirely different level of information.

The spectrum for the (3,3, $\bar{7}$ ) assignment for the D line is shown in Figure 6.4 b). Site assignments can be made from the fact that the separation of the doublet is dependent

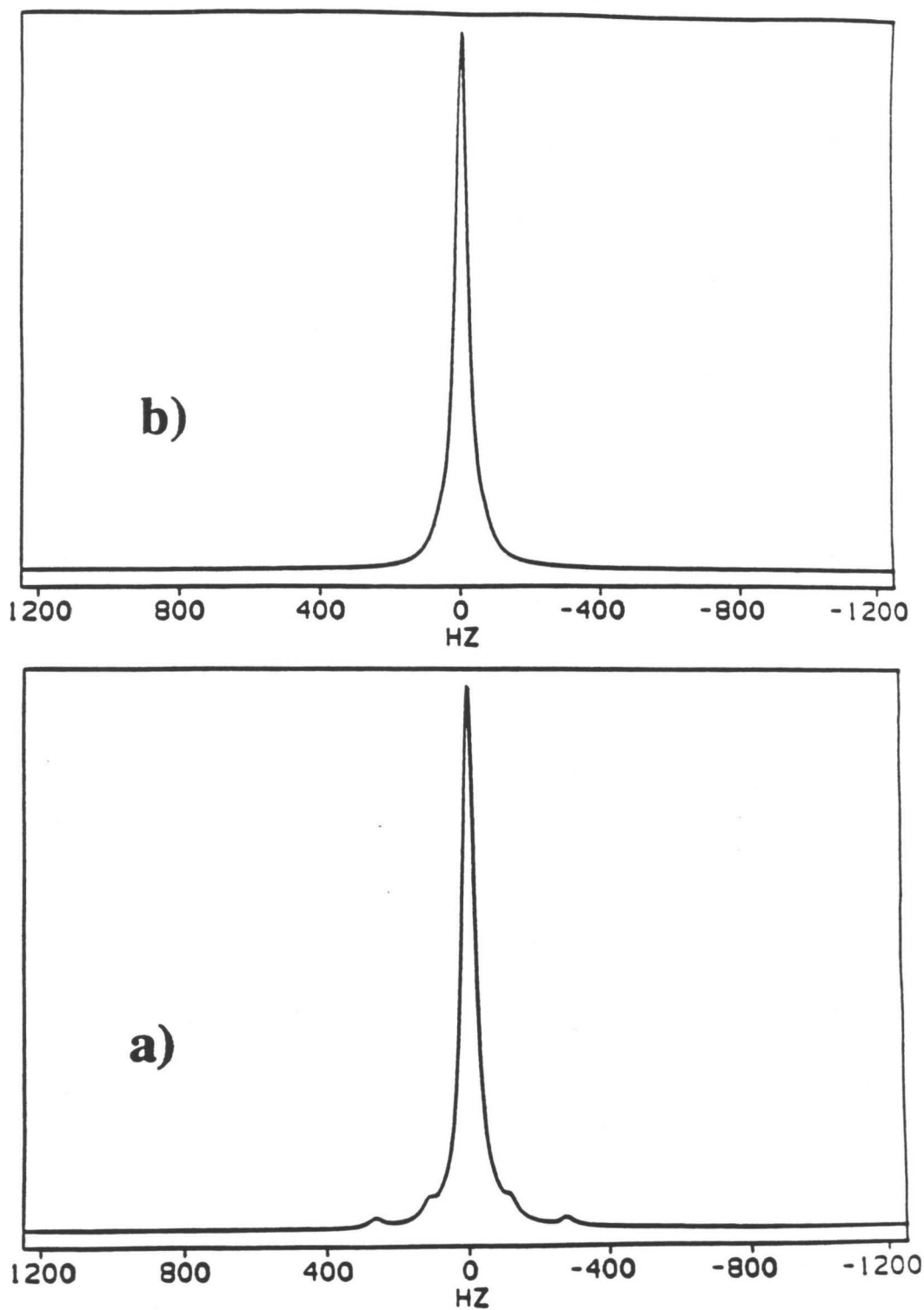


**Figure 6.4:** RE-ENDOR spectrum of the D line in silicon. a) Site assignment (2,2,4) b) Site assignment (3,3, $\bar{7}$ ). No homonuclear couplings are resolved for the former assignment. The structure in the spectrum a) is due to two spins which results in the Pake doublet.

on the magnitude of the homonuclear couplings. In this case the couplings ( $\leq 5.3$  Hz) are not big enough to be resolved.

An important issue for experimental design is the rf power required. A stacked plot of the effect of rf pulse power on the spectrum of a three-spin system made up of 2  $I$  and one  $S$  spin is shown in Figure 6.5 for both the nutation (top) and the  $\pi$  train (bottom). For the nutation sequence with increasing pulse lengths or smaller rf powers, the spectra start to become distorted. These distortions are anticipated from the usual correction terms to the average Hamiltonian for long cycles.

Calculations with the train of phase shifted  $\pi$  pulses gave similar results. The sequence, however, fails at a somewhat higher rf power than the nutation sequence. From an experimental point of view, since the rf homogeneity requirements are high for the nutation experiment, it may be easier to use the phase shifted  $\pi$  train. In addition, the  $\pi$  train gives superior line narrowing off resonance, which will be important if hyperfine inhomogeneity turns out to be the dominant source of the CW ENDOR linewidths.

## 6.6 Conclusions

It has been shown from numerical calculations that the linewidths observed in ENDOR cannot be accounted for by unresolved dipolar couplings and that multiple-pulse line narrowing schemes can be employed to narrow the linewidths by at least two orders of magnitude. More specifically, it has been shown that the nutation sequence or a train of phase-shifted  $\pi$  pulses can be used to extract homonuclear couplings. Heteronuclear couplings can similarly be measured using the SHRIMP sequence. This technique is likely to aid in site assignments and a specific example of a controversial assignment in P-doped Si was considered. Lattice distortions introduced by the presence of paramagnetic impurities could also be measured by sorting out the direct dipole and pseudodipole contributions to the line splittings as discussed in Appendix A. The method developed is

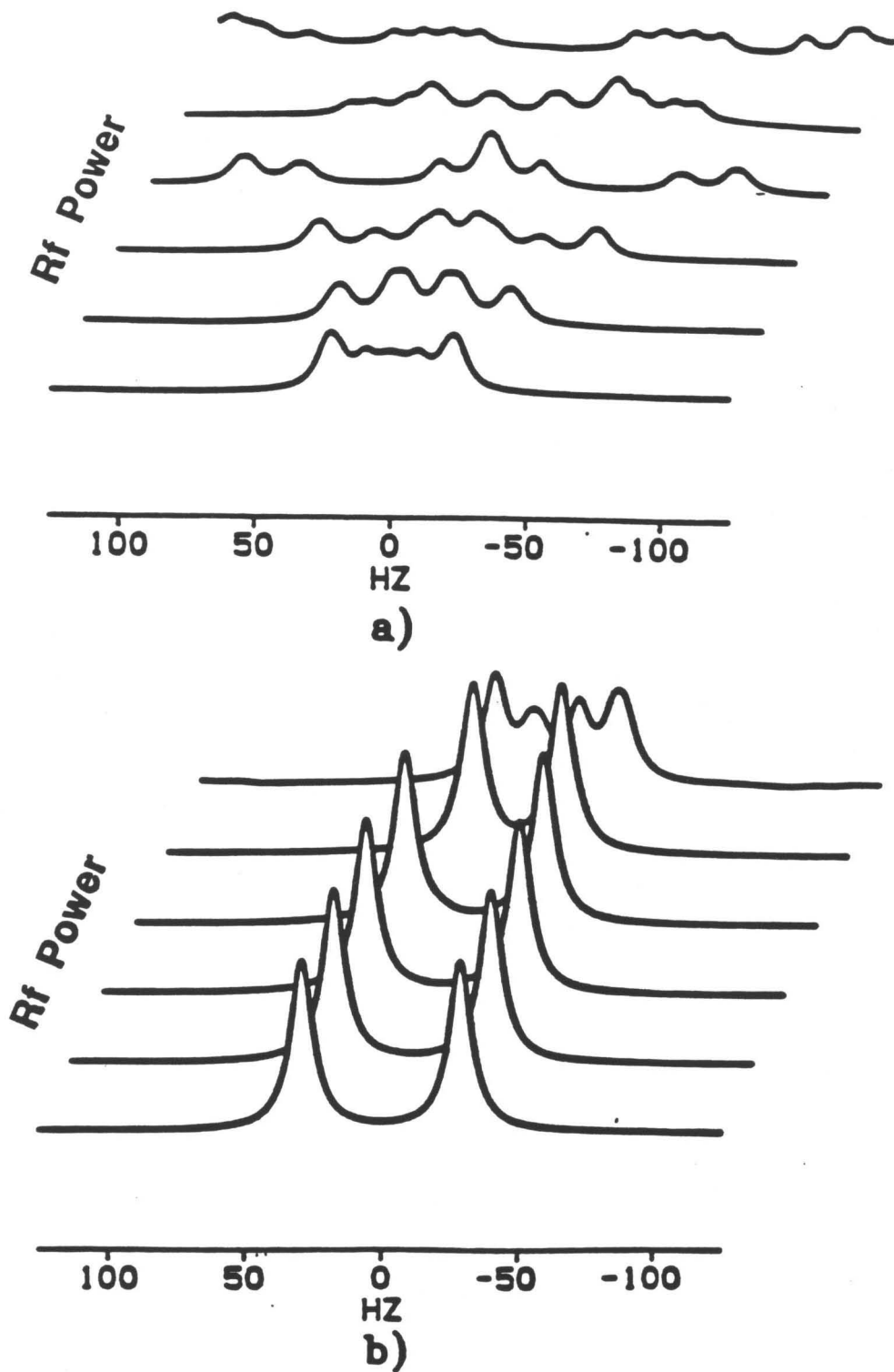


Figure 6.5: Dependence of decoupling efficiency of a) nutation and b)  $\pi$  train on pulse strength. Pulse strength decreases from front to back in both cases. Decoupling efficiency decreases with decreasing pulse strength in both cases.

completely general and is applicable to systems where low temperature ENDOR or near nuclei magnetic resonance spectra have been obtained. The only restriction is that electron spin lifetime effects do not prevent resolution enhancement. Thus 1-He temperatures will usually be necessary.

## 6.7 References

- [1] G. Feher, *Phys. Rev.*, **103**, 834 (1956)
- [2] G. Feher, *Phys. Rev.*, **114**, 1219 (1959)
- [3] E. B. Hale, R. L. Mieher, *Phys. Rev.*, **184**, 739 (1969)
- [4] J. P. Wolfe, *Phys. Rev. B*, **16**, 128 (1977)
- [5] A. Schweiger, M. Rudin, Hs. H. Gunthard, *Mol. Phys.*, **41**, 63 (1980)
- [6] A. Abragam, B. Bleaney, *Electron Paramagnetic Resonance of Transition Ions* (London: Oxford University Press, 1970)
- [7] L. D. Kispert in *Multiple Electron Resonance Spectroscopy*, ed. M. M. Dorio, J. H. Freed (New York: Plenum Press, 1979)
- [8] M. Mehring, P. Hofer, A. Grupp, *Ber. Bunsenges. Phys. Chem.*, **91**, 1132 (1987)
- [9] P. Höfer, A. Grupp, M. Mehring in *Electronic Magnetic Resonance of the Solid State*, ed. J. A. Weil, M. K. Bowman, J. R. Morton, K. F. Preston (Ottawa: Canada Society for Chemistry, 1987)
- [10] K. P. Dinse in *Advanced EPR: Applications in Biology and Biochemistry*, ed. A. J. Hoff (Amsterdam: Elsevier, 1989)
- [11] A. Grupp, M. Mehring in *Modern Pulsed and Continuous-Wave Electron Spin Resonance* ed. L. Kevan, M. K. Bowman (New York: Wiley, 1990)
- [12] C. A. Hutchinson, D. B. McKoy, *J. Chem. Phys.*, **66**, 3311 (1977)
- [13] M. Fujimoto, C. A. McDowell, T. Takui, *J. Chem. Phys.*, **70**, 3694 (1979)
- [14] R. R. Ernst, G. Bodenhausen, A. Wokaun, *Principles of Nuclear Magnetic Resonance in One and Two Dimensions* (Clarendon: Oxford University Press, 1987)

- [15] C. S. Yannoni, R. D. Kendrick, *J. Chem. Phys.*, **74**, 747 (1981)
- [16] D. Horne, R. D. Kendrick, C. S. Yannoni, *J. Magn. Reson.*, **52**, 299 (1983)
- [17] C. Gemperle, A. Schweiger, R. R. Ernst, *Chem. Phys. Lett.*, **145**, 1 (1988)
- [18] R. W. Vaughan, *Annu. Rev. Phys. Chem.*, **29**, 397 (1978)
- [19] J. A. Reimer, R. W. Vaughan, *J. Magn. Reson.*, **41**, 483 (1980)
- [20] D. P. Weitekamp, J. R. Garbow, A. Pines, *J. Chem. Phys.*, **77**, 2870 (1982); **80**, 1372 (1984)
- [21] J. R. Onffroy, *Phys. Rev. B*, **17**, 822 (1975)
- [22] J. L. Ivey, R. L. Mieher, *Phys. Rev. B*, **11**, 822 (1975)
- [23] J. H. Van Vleck, *Phys. Rev.*, **74**, 1168 (1948)
- [24] C. Kittel, E. Abrahams, *Phys. Rev.*, **90**, 238 (1953)
- [25] M. A. Ruderman, C. Kittel, *Phys. Rev.*, **96**, 99 (1954)
- [26] N. Bloembergen, T. J. Rowland, *Phys. Rev.*, **97**, 1679 (1955)
- [27] W. R. Hagen, *J. Magn. Reson.*, **44**, 447 (1981)
- [28] W. R. Hagen in *Advanced EPR: Applications in Biology and Biochemistry*, ed. A. J. Hoff (Amsterdam: Elsevier, 1989)

## Chapter 7

# Fourier Transform Time Sequenced Optical Nuclear Magnetic Resonance: Preliminary Studies

Magnetic resonance is among the most widely used spectroscopic tools for obtaining both static and dynamic structural information. The applicability of magnetic resonance, especially NMR, would be even more far-reaching if not for its inherently low sensitivity which is a result of the small energy of the radiofrequency quantum. The smallness of the quantum involved affects the sensitivity in two distinct ways. First, only small fractional population differences, manifested as spin polarisation, exist between states with opposite magnetic moment. The other limitation arises from having to discriminate these low-frequency signals from the appreciable thermal noise present at such frequencies. Since the early days of NMR, methods aimed at circumventing one or both of the limitations have been proposed.

Of the ways to increase the nuclear polarisation, the most obvious is to work at low temperatures. One disadvantage of this method is that the improvement in nuclear polarisation is quickly offset by the increase in the spin-lattice relaxation time, the time required to achieve equilibrium polarisation. A more attractive and practical way, is to couple the nuclear spin to other degrees of freedom. Dynamic[1] and optical[2] nuclear polarisation are two such common methods. In the former, the nuclear spin is coupled to the electron spin while in the latter it is coupled to the electronic wave function.

Another route that is taken, although only infrequently, is to detect resonant changes in the polarisation by a more sensitive method than rf detection. This principle is called “trigger” detection and can provide significant enhancement in the sensitivity. One of the earliest such methods was the Stern-Gerlach effect[3] while more recent examples include magnetic circular dichroism[4] and Raman heterodyne detected electron nuclear double resonance.[5]

The method discussed in this chapter combines both of these general principles to the study of III-V semiconductors. Significant improvements of existing techniques were made in this laboratory recently, affording a possibility of the study of low concentration defects in such semiconductors. In this chapter a time-domain extension [6] of the technique developed in this laboratory,[7] time-sequenced optical NMR (TSONMR), is discussed.

## 7.1 Optically Detected NMR in III-V Semiconductors

### 7.1.1 Optical Pumping

The band structure of GaAs is shown in Figure 7.1. The three bands are the light hole, heavy hole and the split-off band. At  $k = 0$  the spin-orbit coupling,  $\Delta$ , determines the energy separation between the split-off band and the degenerate light and heavy holes. The band gap at liquid nitrogen temperatures (77 K) is 1.50 eV. Band gap excitation

$$\epsilon < h\nu < \epsilon + \Delta \quad (7.1)$$

causes the electrons to be excited from the light and heavy hole bands to the conduction band. The selection rules for this transition are similar to atomic the transition ( $2P^{3/2} \rightarrow 2S^{1/2}$ ) and arise from the conservation of angular momentum with the angular momentum of the photon being transferred to the electron. For excitation from the split-off band, the selection rules are opposite to those from the degenerate light and heavy hole bands. Thus, left-hand circularly polarised radiation causes transitions with the selection rule  $\Delta m = +1$  while light of the opposite handedness induces  $\Delta m = -1$  transitions. The

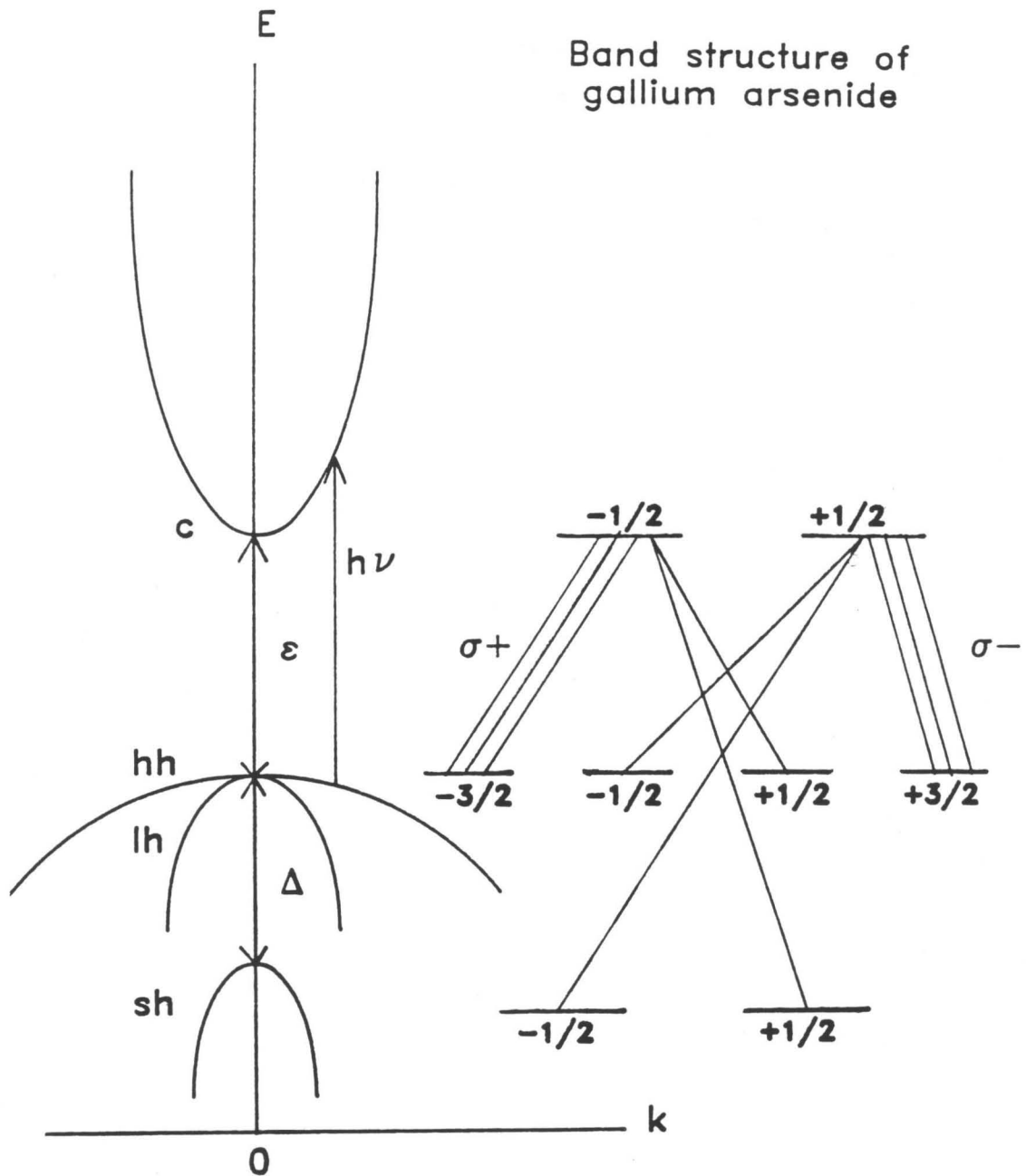


**Figure 7.1: GaAs band structure and selection rules for optical transitions.** *Left:* Band structure of GaAs. In this figure, hh, lh, and sh signify heavy hole, light hole, and split-off band respectively.  $\epsilon$  is the band gap energy,  $\Delta$  is the spin-orbit coupling and  $h\nu$  is the optical pumping laser energy. *Right:* Selection rules for optical transitions for left ( $\sigma^+$ ) and right ( $\sigma^-$ ) circularly polarised light.

probabilities of the transitions for right-hand polarised light, shown in Figure 7.1, are in the ratio of 3:1 for creation of electrons with spin up to that with spin down.

The average electron polarisation,  $P_e$ , in the conduction band is

$$P_e = 2\langle S_z \rangle = \frac{n_+ - n_-}{n_+ + n_-}, \quad (7.2)$$

where  $n_+$  and  $n_-$  are the number of electrons with spin projections  $+1/2$  and  $-1/2$  respectively and the direction of quantisation,  $z$ , is the direction of propagation of the light. With the selection rules of Figure 7.1 and tuning such that transitions from the split-off band are negligible  $\langle S_z \rangle$  can have a maximum of 0.25. For the steady-state optical pumping of concern here,  $\langle S_z \rangle$  is diminished from that at the time of photocarrier creation due to spin-lattice relaxation  $\tau_s$  during the lifetime  $\tau$  ( $10^{-9} - 10^{-10}$  s) of the electron in the conduction band and is given by

$$\langle S_z \rangle = 0.25 \frac{\tau_s}{\tau + \tau_s}. \quad (7.3)$$

The 0.25 in the above equation is the maximum electron spin expectation value achievable at the time of creation. Since angular momentum is conserved between the electron and photon during this process the luminescence is polarised. The degree of circular polarisation is defined operationally as

$$\rho = \frac{I_+ - I_-}{I_+ + I_-}. \quad (7.4)$$

Here  $I_+$  and  $I_-$  are the intensities of the  $\sigma_+$  and  $\sigma_-$  polarised radiation respectively. This is the observable in the experiments reported in this chapter. The polarisation of the radiation is related to the average electron spin in the conduction band by

$$\rho = -\langle S_z \rangle. \quad (7.5)$$

Optical pumping is usually performed in the presence of a magnetic field (in all the experiments reported here this magnetic field was 150 G) since  $\tau_s$  is longer in a magnetic

field which implies that larger electron polarisations can be achieved. The magnetic field is, for all practical purposes, parallel to the direction of the optical pumping radiation. Figure 7.2 is a view of the experimental setup and makes clear the orientation of the different fields. A more detailed description of the experimental setup is given in 7.4.1.

### 7.1.2 Optical Nuclear Polarisation

The spin-polarised photoelectrons created by optical pumping interact with the nuclei by the hyperfine interaction. The isotropic part of this interaction for the  $k$ th nucleus located at  $\mathbf{r}_k$  is given by

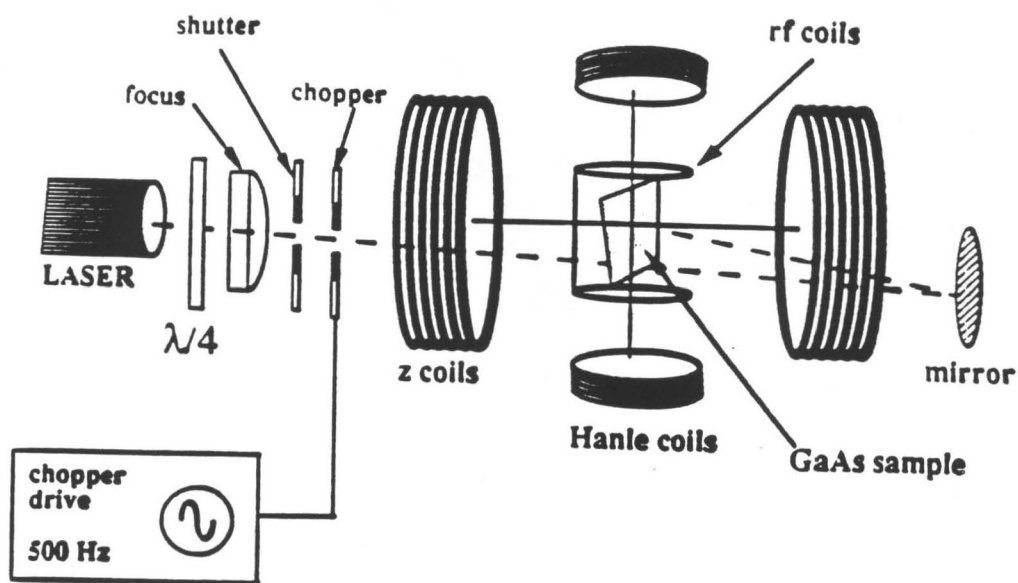
$$\mathcal{H}_{\text{hf}}^k = \frac{8\pi}{3} g\beta g_n \beta_n \mathbf{I} \cdot \mathbf{S} |\psi(\mathbf{r}_k)|^2. \quad (7.6)$$

The coupling is dependent on the magnetic moments of the electron ( $g\beta\mathbf{S} = \gamma\hbar\mathbf{S}$ ) and nucleus ( $g_n\beta_n\mathbf{I} = \gamma_n\hbar\mathbf{I}$ ) and the probability density of the electron at the nucleus,  $|\psi(\mathbf{r}_k)|^2$ . The hyperfine interaction has terms of the form  $I_+S_-$  and  $I_-S_+$  which cause simultaneous electron-nuclear flip-flop. Fluctuations in this term are the mechanism for the transfer of the electron polarisation to the nuclei[8, 9, 10, 11], with a time constant  $T_{1\text{on}}$  which varies from seconds to minutes. The polarisation exchanging flip-flop transitions are distance dependent (through the electron density term in the hyperfine interaction) and occur more efficiently if the excited electron is localised. This happens readily at donor sites in the host lattice which are referred to as the optically relevant defects (ORD). Nuclei within typically 100 Å (the effective Bohr radius around the donor) of an ORD are polarised directly and transfer of polarisation to the nuclei outside the effective Bohr radius occurs by spin diffusion. The degree of nuclear polarisation is determined by

$$\langle \mathbf{I} \rangle = f \frac{I(I+1)}{S(S+1)} \langle S_z \rangle. \quad (7.7)$$

In this expression  $f$  is a leakage factor and includes all other nuclear spin-lattice relaxation mechanisms that reduce the observed nuclear polarisation. An enhancement of at least  $10^5$  over that obtained by normal means is achievable with this method.

## Excitation Optics



## Detection Optics

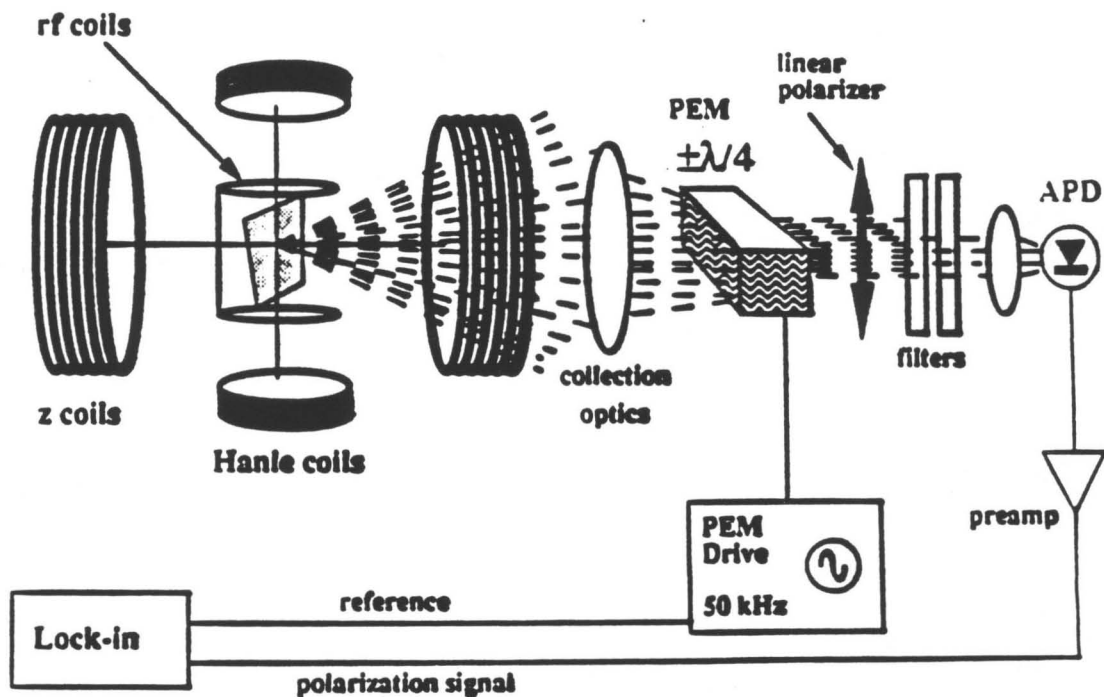


Figure 7.2: Experimental setup for optically detected NMR. The orientation of the different magnetic fields is shown in detail. The sample resides in a cryostat which is not shown. The circularly polarised luminescence emitted is converted to linearly polarised radiation by the PEM.

The presence of the applied magnetic field is important for the creation of Zeeman order (which corresponds to nuclear polarisation). In the absence of such a field of at least several gauss; the nuclei have no preferred axis of quantisation and the Zeeman order cannot serve as a reservoir.

### 7.1.3 Optical Detection

The nuclear polarisation created optically can, in principle, be detected by conventional means but never has been in GaAs. This is because significant advantages are achieved by optical detection.[12, 13] There are two mechanisms by which the nuclear polarisation affects the luminescence polarisation. Both of these mechanisms can be understood in terms of the local hyperfine field of the polarised nuclei,  $\mathbf{B}_n$ , which is proportional to  $\langle \mathbf{I} \rangle$ . The nuclear field has contributions from all the NMR active nuclei. For example, in GaAs,  $^{69}\text{Ga}$  (spin = 3/2, natural abundance = 60.4%),  $^{71}\text{Ga}$  (spin = 3/2, natural abundance = 39.6%), and  $^{75}\text{As}$  (spin = 3/2 and natural abundance = 100%) contribute to the nuclear field. In the experiments reported, the nuclear field is oriented antiparallel to the applied magnetic field at the end of nuclear polarisation.

The dependence of  $\tau_s$  on the total field  $\mathbf{B}_t = \mathbf{B}_0 + \mathbf{B}_n$  constitutes the first mechanism for depolarisation. The contribution from this mechanism is insignificant compared to the second, which is the luminescence depolarisation as a result of the precession of the optically pumped electron spins about the total field. In analogy with the depolarisation of fluorescence seen in fluorescing atoms in a transverse magnetic field this luminescence depolarisation is termed the Hanle effect.

## 7.2 Steady-State ODNMR

The steady-state version of an optically-detected NMR experiment proceeds as follows. In the presence of band gap irradiation which leads to ONP, the rf is continuously

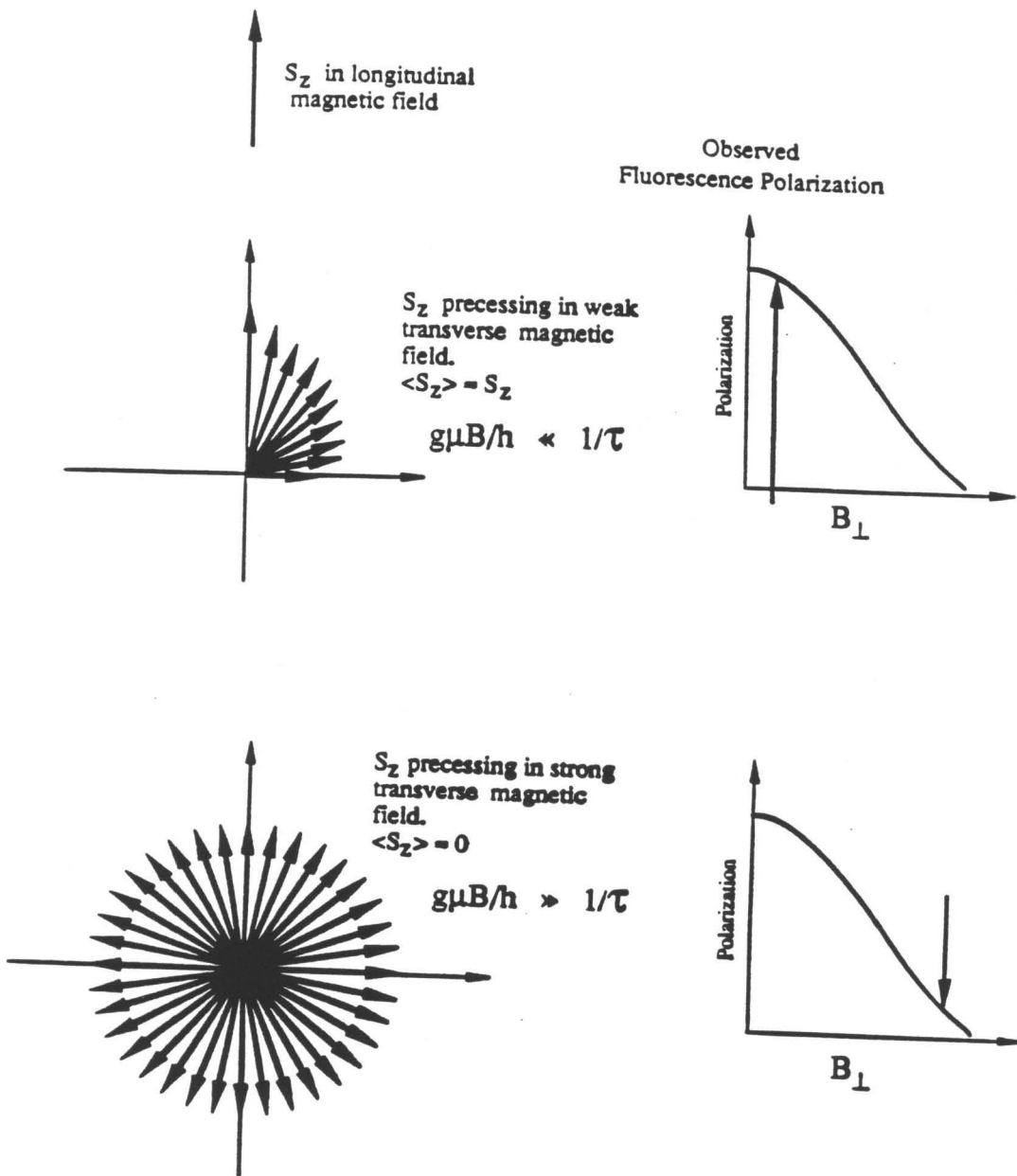


**Figure 7.3: Schematic of Hanle effect detection.** *Top:* Incomplete luminescence depolarisation in the presence of a transverse field not orthogonal to the average electron spin. *Bottom:* Complete depolarisation in an orthogonal transverse field.

swept. At or near resonance the nuclear field is tilted by the rf and a transverse component is created resulting in a tilted total field. The luminescence is depolarised since the average electron spin is no longer aligned with the total field. A vector picture of the processes occurring during the detection process is represented in Figure 7.3. As might be expected, maximum depolarisation is achieved when the total field is orthogonal to the electron spin direction (complete Hanle effect), but this is achieved in the steady-state experiments only by an unlikely cancellation between the applied field and those contributions to the nuclear field which remain antiparallel to it.

In previous optically detected NMR<sup>1</sup> (ODNMR) experiments in GaAs [12, 14, 15, 16, 17, 18] the optical pumping, rf irradiation and Hanle effect detection occurred simultaneously in a static magnetic field parallel to the pumping light. When the rf is far from resonance, the nuclei are polarised along the static magnetic field. As the rf is swept through a nuclear resonance, the nuclei precess about the rf field. This produces a component of  $\mathbf{B}_n$  perpendicular to the static field direction, and to the average electron spin  $\langle S \rangle$ . The electron spins precess in this oblique total magnetic field, and a Hanle-effect reduction in  $\rho$  is observed. This is called steady-state ODNMR.

The experimental situation of simultaneous optical pumping, rf irradiation and Hanle effect detection adversely affects both the resolution and the sensitivity of the optically detected NMR experiment. Sensitivity is compromised by the fact that the detection process is carried out with the total field at an oblique angle to the  $z$ -axis instead of the optimal orthogonal arrangement of the Hanle field and the exciting optical radiation.

An even bigger disadvantage is the effect of simultaneous optical pumping and rf irradiation on the resolution of the NMR spectrum. During the acquisition of the NMR spectrum, the electrons are continuously pumped to the excited state and the nuclei see an average over those electronic states which are occupied in the presence of the

---

<sup>1</sup>this is a misnomer since the method involves both optical nuclear polarisation *and* optical detection

light. This manifests itself as a line shift and broadening due to the Knight shifts from the photocarriers, which vary with distance from the ORD. Also the NMR spectrum is dominated by those nuclear sites with the largest hyperfine couplings. These two disadvantages limit the applicability of steady-state ODNMR as an analytical tool.

### 7.3 Time-Sequenced Optical NMR Experiment

Recent experiments[6, 7, 19] performed in this laboratory in a time-sequenced fashion have achieved significant sensitivity and resolution enhancement relative to steady-state ODNMR.

The resolution disadvantage of steady-state ODNMR is circumvented in time sequenced optical NMR by performing the NMR part of the experiment in the absence of optical pumping. The second improvement is in the detection process which employs an additional applied field perpendicular to the optical axis.[20]

Experimentally, the first advantage is easily realised by shuttering off the laser during rf irradiation by a mechanical device. The advantage in the detection (the complete Hanle effect) is achieved as follows. If, after rf irradiation, the applied magnetic field, which is parallel (this is only approximately true since geometric constraints do not permit a perfect parallel arrangement) to the direction of the optical pumping radiation and along which the nuclei are quantised, is ramped down with a simultaneous ramping up of a field orthogonal to the light (Hanle field) then the residual nuclear field adiabatically follows the total field and eventually is perpendicular to the light and the electron spin. From the vector picture depicting the Hanle effect in Figure 7.3 it is obvious that complete luminescence depolarisation is possible for this case. In practice the experiment is performed in the region where  $\rho$  depends steeply and linearly on the total field. Extensive sensitivity analysis of this method has already been published.[7] Figure 7.4 shows a timing diagram for the TSONMR experiment.

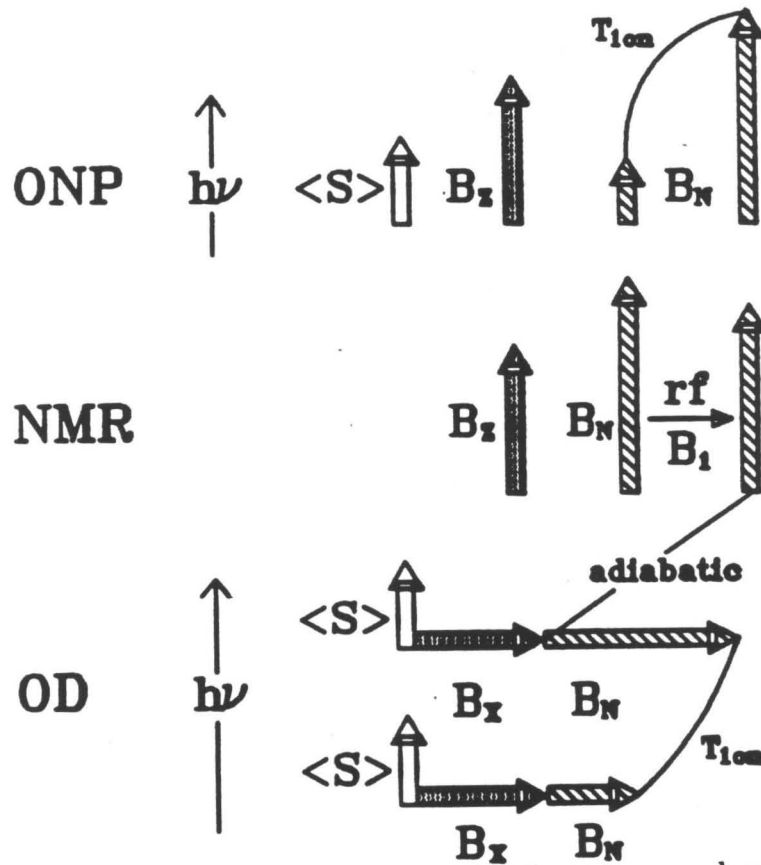
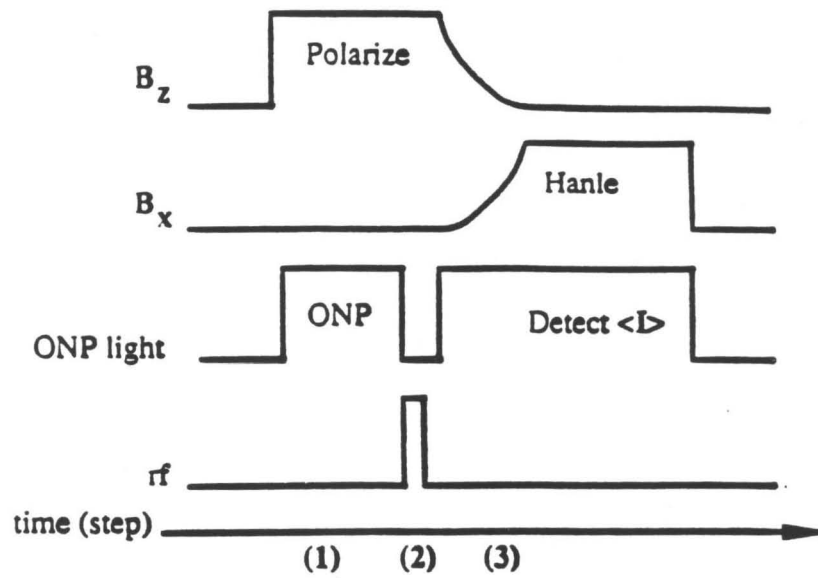


**Figure 7.4:** Timing diagram and vector picture for time-sequenced optical NMR. During the ONP period in the presence of the magnetic field  $B_z$  the nuclei are polarised in the direction of the laser irradiation. After the NMR period in the absence of the laser, the fields are adiabatically switched from  $B_z$  to  $B_x$  producing a magnetic field orthogonal to the electron spin and hence a sensitivity advantage.

## 7.4 Time-Domain TSONMR

In CW-TSONMR the NMR part of the experiment is performed in a continuous wave fashion; the weak 100 ms pulse is long enough to destroy magnetisation in proportion to the linear response NMR absorption curve. As is now well known, significant advantages are possible by performing the same experiment in the time-domain. In CW-TSONMR, as in all CW experiments, there is a crucial interplay between signal-to-noise ratio and the power of the rf irradiation. Increasing rf power to improve sensitivity leads first to power broadening of the lines and later to second-order effects such as the excitation of multiple-quantum transitions. If care is not taken, these effects are seen routinely in steady-state ODNMR and TSONMR experiments.[19, 21] These artifacts, however, do not plague time-domain experiments. More importantly, time-domain methods allow the various experiments associated with the concepts of selective averaging and multidimensional spectroscopy to be done by TSONMR.

### 7.4.1 Experimental Details

The experimental setup used for the time-domain experiment is identical to that used for the time-sequenced instrument. A brief description of the experimental setup used in the experiments is presented here. A more extensive description of the instrument can be found in a detailed report to be published from this laboratory.[22]

A schematic of the experiment used for TSONMR is presented in Figure 7.2. The excitation optics consist of a multimode semiconductor diode laser at 790 nm. The laser output is linearly polarised but is converted to circular polarisation by a quarter-wave plate after collimation. The laser is chopped at 500 Hz and strikes the sample at 15° with respect to the magnetic field. The sample is p-GaAs with  $4 \times 10^{17}$  /cc of Zn atoms as the impurity and is maintained at 77 K in a liquid N<sub>2</sub> cryostat made of glass.

The static and Hanle fields are provided by electromagnets arranged around the tail

of the glass cryostat as shown in Figure 7.2. The radiofrequency coils were placed inside the cryostat as part of the sample holder. The static and Hanle fields were regulated using home-built shunt current regulators and were ramped using externally supplied modulation voltages. The rise/fall time is 50 msec. The maximum field of the longitudinal coil was  $\approx 200$  G while that for the Hanle field was  $\approx 100$  G and in both cases was limited by resistive heating.

The radiofrequency portion of the spectrometer consists of a Hewlett-Packard frequency synthesiser whose output is amplified with an ENI broad-band power amplifier. The rf pulses are controlled by an Interface Technology digital word generator with an IBM PS/2 Model 80 computer serving as the master control.

The detection path utilizes a collection lens which collimates the luminescence. A photoelastic modulator (PEM) oscillating between  $\pm\lambda/4$  retardation at 50 kHz functions as a quarter-wave polariser alternately turning left or right circularly polarised light into linearly polarised light which is passed by the linear polariser. The signal that is modulated at both the PEM and the chopper frequencies is detected by an RCA avalanche photodiode. The signal is digitised by two lock-in amplifiers locked to the PEM and chopper frequency respectively. These correspond to the numerator and denominator, respectively, in the expression for  $\rho$  (equation 7.4). During the course of these experiments the noise characteristics of the detection system were measured and these are reported in Appendix B.

#### 7.4.2 Nutation

Transient nutation phenomena, also known as Torrey oscillations,[23, 24] occur when rf radiation is suddenly turned on at or near resonance. It can be visualised in the rotating frame as the precession of the magnetisation around the effective field with frequency

$$\omega_e = (\Delta\omega + \omega_1^2)^{1/2},$$

where  $\omega_1 = \gamma B_1$  is the strength of the driving field and  $\Delta\omega = \omega - \omega_0$  is the frequency offset of the driving field from the resonance frequency. The nutation pulse sequence consists of a single pulse of length  $t_1$  that is incremented for each point in the spectrum. An optically detected transient nutation in GaAs is presented in Figure 7.5. The Fourier transform of this data is provided as an inset. An interesting point to note is that due to the relatively small longitudinal field of 0.015 T (150 Gauss), the resonance has a Bloch-Siegert shift[27] of  $\omega_1^2/4\omega_0 = 840$  Hz from the CW experiment.

In NMR experiments performed in this laboratory on GaAs but detected by conventional methods (the impurity concentrations were much higher in these samples) the nutation spectrum showed a frequency component which was twice the nutation frequency.[25] This effect is seen in quadrupolar nuclei of half-integer spin  $I$ , for  $\omega_Q$  (quadrupole coupling constant)  $\gg \omega_1$  and is a means of separating the quadrupolar perturbed sites from the unperturbed ones. This effect results from the fact that the nutation frequency of the central transition ( $-1/2 \rightarrow 1/2$ ) is  $(I + \frac{1}{2})\omega_1$ . [26] This effect was not observed in the nutation experiments reported here but has very recently been seen in identical TSONMR experiments on different p-GaAs samples.

### 7.4.3 FT-TSONMR

A Fourier transform TSONMR experiment consists of a simple two-pulse experiment using the sequence

$$\theta_x - t_1 - \theta_x.$$

The initial  $\theta_x$  pulse rotates the nuclear magnetisation in the  $yz$  plane of the rotating frame by an angle  $\theta_x = \gamma B_1 t_1 = \omega_1 t_1$  and initiates a period of free evolution, just as in a conventional NMR experiment. The evolution period is continued for an interval  $t_1$ , then a second  $\theta_x$  pulse returns the remaining magnetisation to the  $z$ -axis for measurement by Hanle detection following the field cycling step. The signal  $S(t_1)$  is analogous to an FID

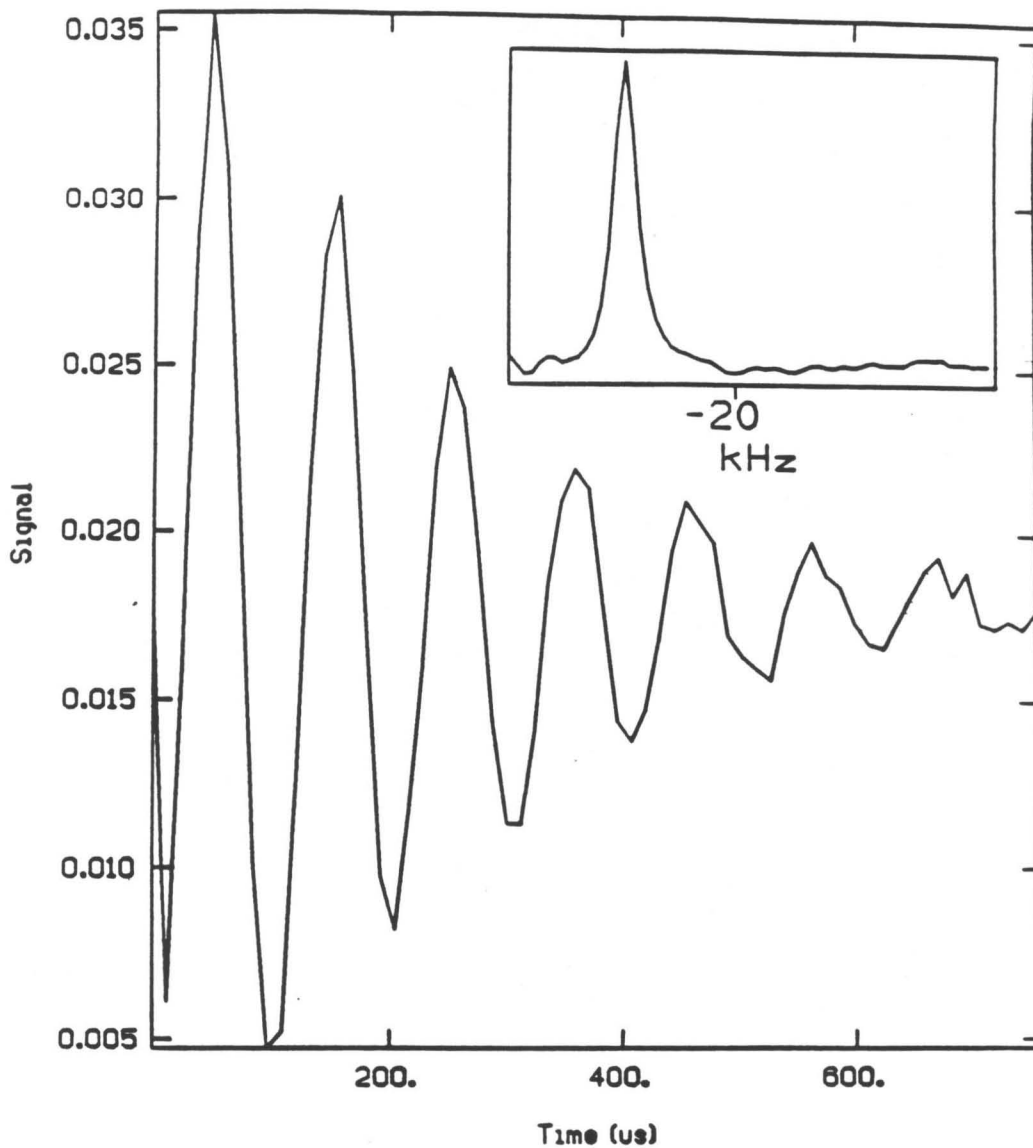


**Figure 7.5: Optically detected transient nutations.** *Inset:* Fourier transform of transient nutation. The pulse sequence is given at the bottom. Notice the absence of a frequency component at twice the nutation frequency.

as observed in conventional NMR experiments, except that it is observed using a sample that is  $10^6$  times smaller.

Figure 7.6 shows an FID of  $^{71}\text{Ga}$  nuclei obtained by FT-TSONMR. The rf pulse frequency was offset from the resonance frequency by 10 kHz and both pulse lengths were set to  $9.0 \mu\text{s}$  for a  $\theta_x = \pi/2$  pulse angle. The inset in the figure shows the Fourier transform of the FID. The resonance line was fitted to a Lorentzian (gives a nominally better fit than a Gaussian in all cases) curve with a linewidth of 3.7 kHz. This linewidth is 1.6 times larger than that observed for the CW-TSONMR and conventional NMR experiments, which indicates that the FT-TSONMR experiment probes different sites from its CW counterpart. This is discussed in Section 7.4.5. Experiments performed to investigate this difference are discussed in detail in section 7.4.5.

An important advantage of the FT experiment over steady-state optically detected NMR methods is increased sensitivity. The time-domain methods permit 100% of a given species of nuclear spins to be affected by an NMR experiment without the disadvantages of power broadening inherent in steady-state experiments. This advantage is evident in Figure 7.7 where the results of steady-state ODNMR and FT-TSONMR of  $^{71}\text{Ga}$  performed under identical conditions are compared. The resolution and sensitivity of the time-domain experiment are better by factors of 3 and 8, respectively.

#### 7.4.4 Relaxation Parameters From FT-TSONMR

In addition to the NMR spectral information which can be found from FT-TSONMR and TSONMR nutation experiments, the time-sequenced technique can measure NMR relaxation times.

Both CW and FT-TSONMR are capable of measuring NMR spin-lattice relaxation times,  $T_1$ . For the CW experiment the spin-lattice relaxation time is measured by waiting a time  $t_1$  after the rf irradiation and then cycling the field for detection. The magnetisation is monitored using TSONMR as it diminishes along the  $z$  axis toward the small

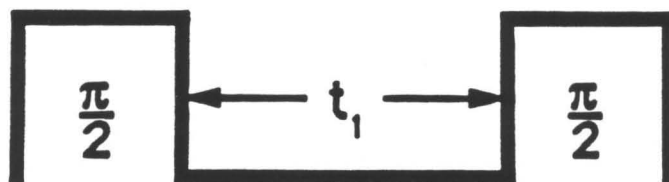
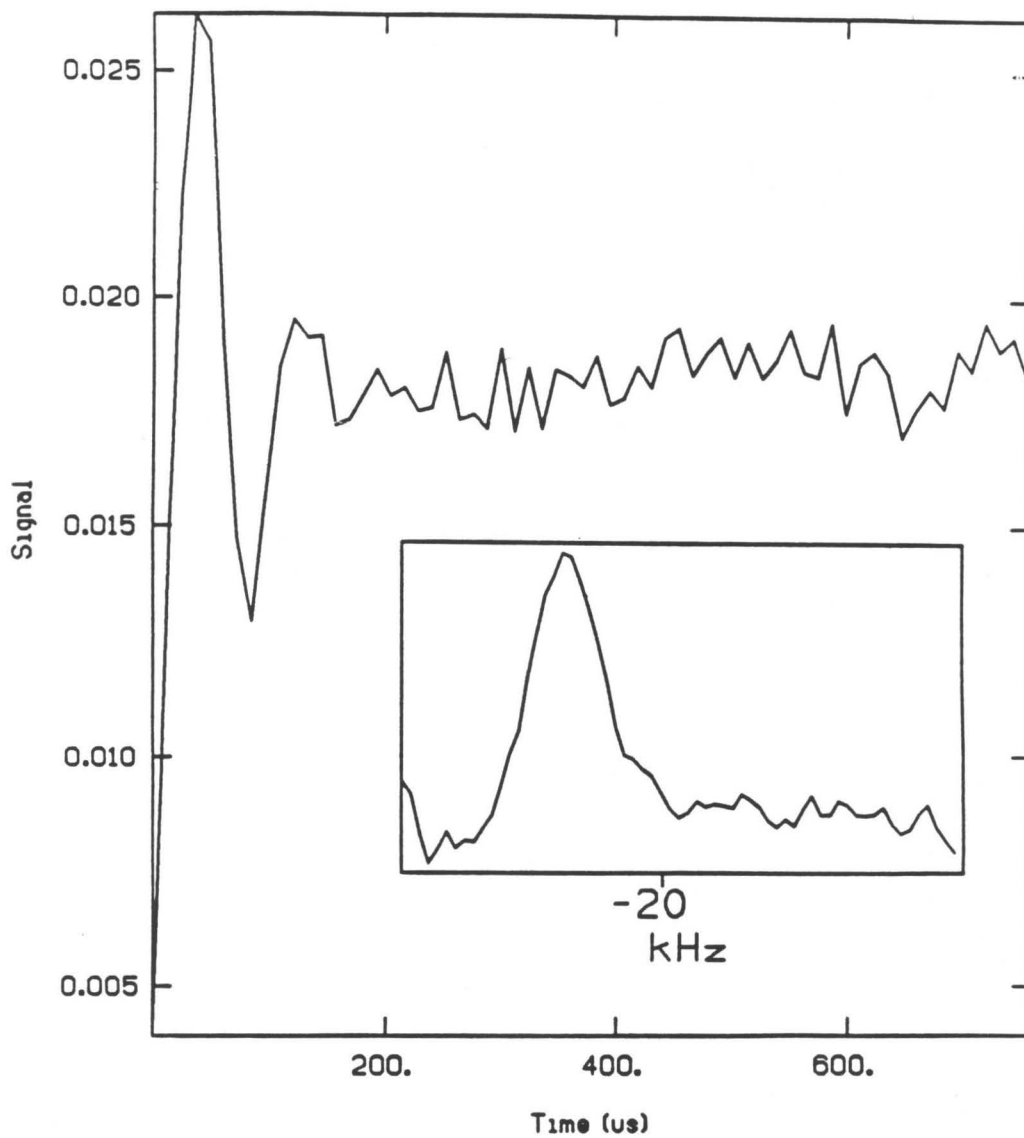


**Figure 7.6: Optically detected two-pulse FID.** *Inset: Fourier-Transform of two-pulse FID.*  
The pulse sequence is given at the bottom.

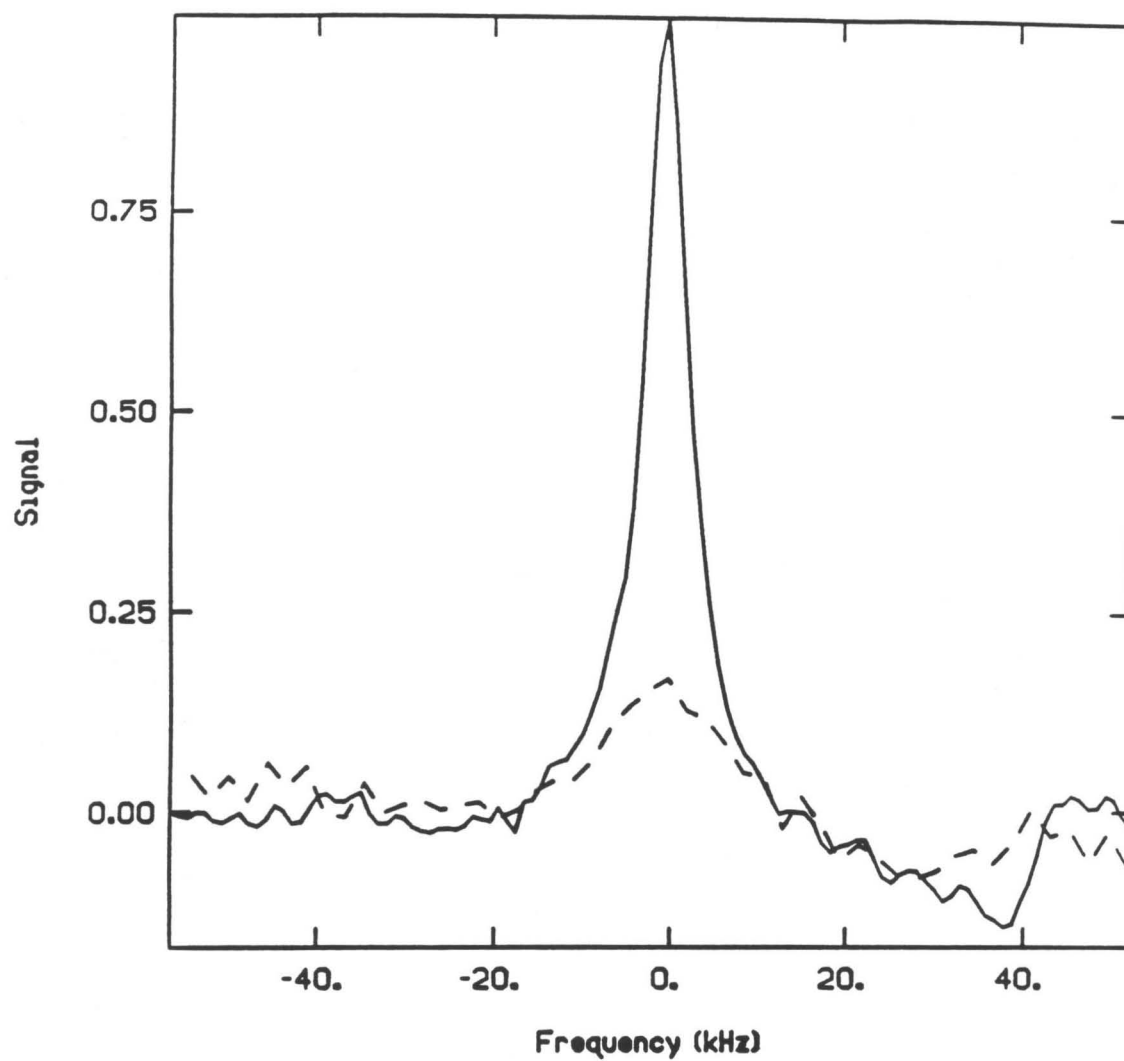


**Figure 7.7:** Comparison of steady-state ODNMR (dashed line) and Fourier Transform (solid line) TSONMR. FT-TSONMR provides 8 times more sensitivity and 3 times better resolution than steady-state ODNMR.

equilibrium value as a function of the delay  $t_1$ . The  $T_1$  measurement by FT-TSONMR is done with a suitable adaptation of the inversion-recovery experiment. The spins are inverted by a  $\theta_x = \pi$  pulse followed by a recovery delay  $t_1$  which is incremented for each point on the decay curve. The CW and FT versions of the  $T_1$  experiment yield very different results. The spin-lattice relaxation curve from the FT experiment is a simple decay which can be fit to a  $T_1$  of 5.7 seconds. The CW experiment, however, shows an initial rise due to spin diffusion from the bulk nuclei outside the optically detected volume, as will be discussed below. The CW  $T_1$  data is shown in Figure 7.8.

The spin-spin relaxation time  $T_2$  or more precisely, the echo decay time is measured using a spin-echo pulse sequence with FT-TSONMR. The NMR part of the spin-echo[28] experiment consists of the pulse sequence

$$\left(\frac{\pi}{2}\right)_x - t_1 - \pi_x - t_1 - \left(\frac{\pi}{2}\right)_x$$

which is similar to the Hahn spin-echo experiment. The  $\pi/2$  pulse starts a free evolution period. After a period  $t_1$  a pulse with flip angle  $\pi$  reverses the sense of precession from the first  $t_1$  period. Another  $t_1$  time period later the magnetisation rephases, producing an echo. The decay of the echo amplitude is plotted against the interpulse delay  $t_1$ , and the spin-spin relaxation time  $T_2$  is determined by fitting the data to an exponential function.

#### 7.4.5 Linewidths and Spin Diffusion

In previous ODNMR experiments spin diffusion has been shown to be the link between the bulk nuclear spins and the nuclear spins which are optically polarised and detected (in a sphere of 100 Å about the ORD).[13] These more distant nuclei influence the optically detected NMR signal by coupling to the near nuclei through nuclear dipole-dipole interactions. The diffusion constant and the diffusion radius for  $^{75}\text{As}$  in high-purity GaAs have been previously determined experimentally.[29] In the time-sequenced experiments the detection period was 6 s, which should be ample time for spin diffusion processes

to influence the signal. These effects must be considered in interpreting the  $T_1$  data of  $^{71}\text{Ga}$  obtained from measurements using CW-TSONMR and FT-TSONMR, as well as the different linewidths seen in these two methods (section 7.4.3).

The CW  $T_1$  data show an unexpected rise during the first few points which can be explained qualitatively as spin diffusion. In order to illustrate this point more clearly it is useful to employ spin temperature arguments. At the end of the ONP period of the experiment the nuclear spin system in the irradiated volume has reached a steady-state with each nuclear species at a separate spin temperature. Since the nuclei are strongly polarised by ONP the spin temperature is cold compared to the lattice temperature. Resonant rf irradiation reduces the nuclear polarisation which in spin-temperature parlance corresponds to heating of the spins. The simplest model divides the resonant spins into two groups: those near enough to the ORD to be quadrupolar perturbed (have quadrupolar satellites outside the linewidth attributed to spin-spin interactions) and those whose valence band (light-off) spectrum is not measurably perturbed. If these near spins were to dominate the CW-TSONMR signal then the signal versus  $t_1$  would decay with the  $T_1$  of the near nuclei. That they in fact make a negligible contribution is already clear from the observation that the CW-TSONMR linewidth is identical to that of pure GaAs by ordinary NMR. Rather the CW-TSONMR spectrum is dominated by unperturbed spins, including bulk spins, those which are distant ( $\geq 100 \text{ \AA}$ ) from the ORD that their influence on the optically detected spins occurs by spin diffusion with time-constants, typically, of the order of seconds. The data in Figure 7.8 indicate that spins outside the optically detected volume do contribute to the CW-TSONMR signal since for early time points there is an increase in the measured signal. This rise is attributed to the response of the bulk spins to resonant irradiation measured as a time-delayed effect on the nuclei in the optically detected volume. A maximum in the signal intensity is seen after an 800 ms delay in the dark after irradiation with rf. At times greater than 800 ms the  $T_1$  of

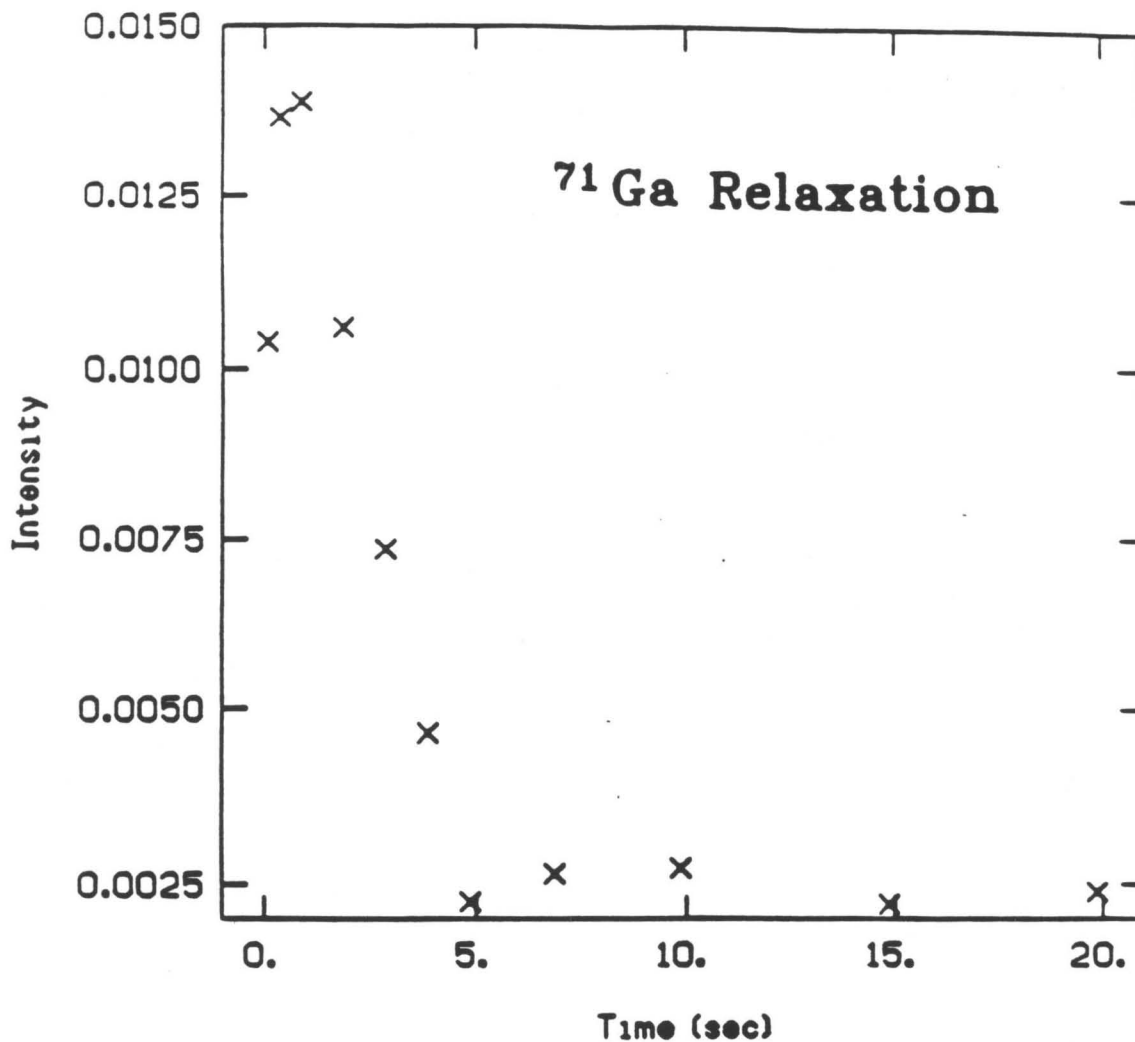


Figure 7.8: Spin-lattice relaxation in  $^{71}\text{Ga}$  measured by CW experiments. The experiments are performed by rf irradiation followed by a variable delay. The  $z$ -magnetisation as a function of the variable delay is plotted. The non-exponential behaviour is noteworthy. The initial rise in the data is due to spin diffusion from the bulk.

these spins becomes the dominant relaxation process.

The data from the FT-TSONMR experiment do not exhibit an initial rise in the signal intensity. The reason for this difference from the CW variant is that the  $\pi$ -pulse used for the inversion-recovery experiment inverts the spins near the ORD as well as the far away spins and no spin temperature gradient between these sites is achieved. The thermal contact with the more distant spins leads to transient behaviour, since they start with similar temperature. The resulting signal is a simple decay with a time constant,  $T_1$ , of 5.7 seconds.

The results of the spin-lattice relaxation experiments seem to indicate that the CW and FT experiments probe different sites. The CW variant of the experiment is sensitive to sites  $\geq 100 \text{ \AA}$  away from the ORD whereas the FT experiment is additionally sensitive to the less numerous spins at distances  $\leq 100 \text{ \AA}$  away from the ORD. This is consistent with the difference in the linewidths of the two experiments. The line broadening seen in the FT-TSONMR experiment is interpreted as unresolved quadrupole satellites. These perturbed sites can be seen in the FT experiment because they are ineffectively heated or cooled by the more abundant distant spins in the short time available. They are invisible in the CW experiment, because heating by weak irradiation at their resonance frequencies is incapable of competing with cooling by spin diffusion from the cold and more abundant distant spins.

In order to sharpen this model of two spin populations, a time-domain experiment which detects the sites responsible for the CW-TSONMR signal was devised. The premise behind this experiment is that the distant spins responsible for the CW signal will dominate whenever the spin temperature in the optically detected volume is not modulated by the nearby spins. This modulation was suppressed by an extra period of ONP and spin diffusion subsequent to the NMR. The time sequencing for this experiment is: (1) ONP period for 6 s; (2) a  $\theta_x - t_1 - \theta_x$  sequence with the pumping light off; (3) reillumination.

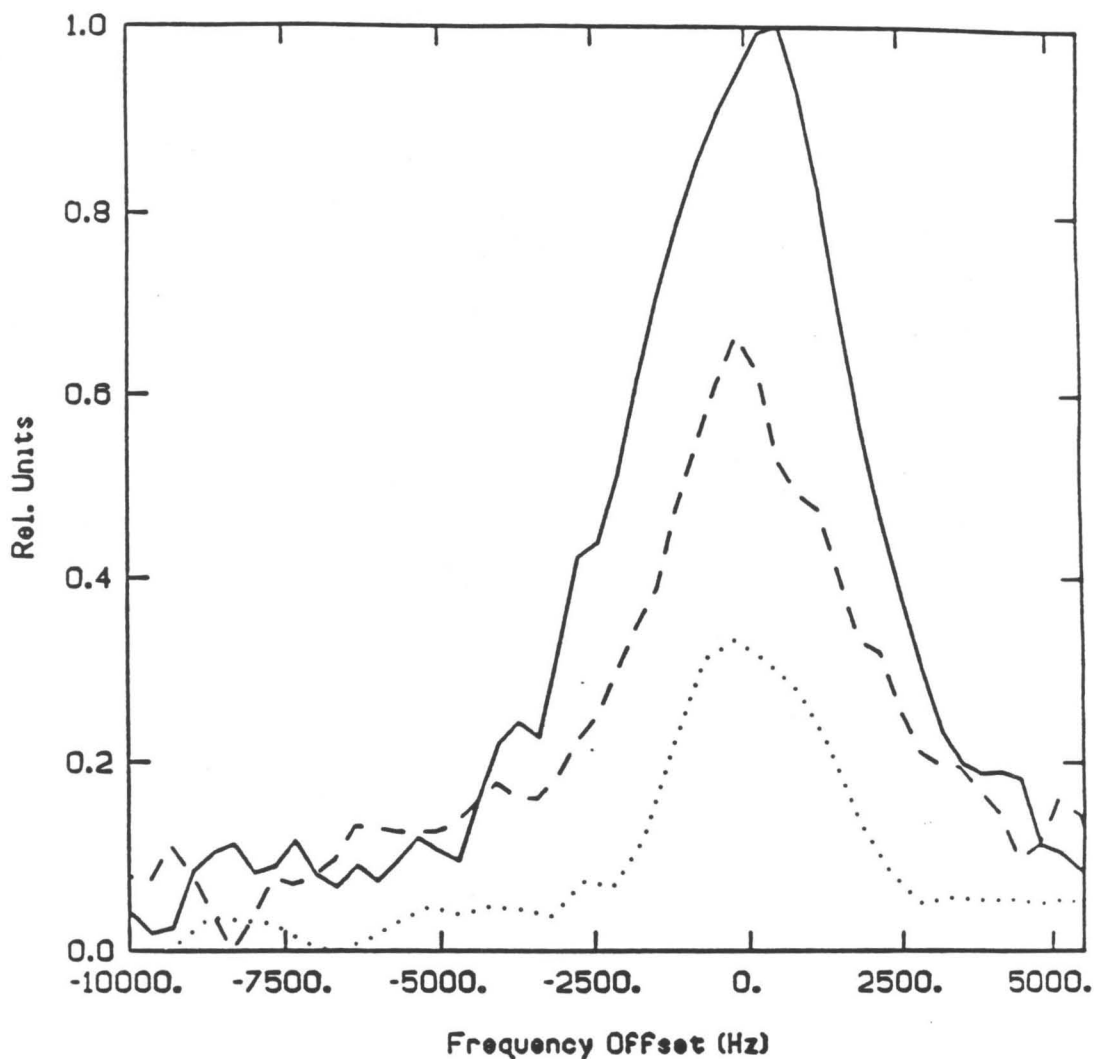


Figure 7.9: Linewidth for the CW (dotted line), FT (solid line), and FT with 2 s nuclear polarisation and a 1 s spin diffusion periods (dashed line). The last experiment involving rf irradiation followed by nuclear polarisation and spin diffusion periods probes the same sites as the CW-TSONMR experiment.

mination with the pumping light for 2 s; (4) a spin diffusion delay in the dark for 1 s; (5) field cycling and optical detection for 6 s. Steps 1 and 2 of this experiment are no different from a regular FT-TSONMR experiment. The extra ONP of the modulation preferentially repolarises the nearby spins while the penultimate delay allows the distant spins to determine the temperature of the optical volume. The result of this experiment compared with the FT-TSONMR and CW-TSONMR experiments is shown in Figure 7.9. The FT-TSONMR experiment with extra ONP followed by spin diffusion (extra ONP/SD) results in a linewidth of 2.9 kHz which is the linewidth associated with bulk spins.

The second experiment performed was a Hahn spin-echo. The results for spin-echo experiments done with and without extra ONP/SD are shown in Figure 7.10. The decay of the echo amplitude is significantly different for the two experiments. For the experiment without extra ONP/SD the fast decay of the echo amplitude is due to the quadrupole couplings which are not refocused by the  $\pi$ -pulse. The decay corresponding to 2 s extra ONP/1 s SD is much slower. The sites responsible for this signal do not have appreciable quadrupole couplings and the linewidth is due to homonuclear spin-spin couplings. The spin-echo is able to refocus the heteronuclear couplings, and thereby increase  $T_2$ , resulting in a slower decay of the spin-echo amplitude.

## 7.5 Conclusions

A time-domain extension of the time-sequenced optical NMR experiment has been applied to the study of III-V semiconductors. FT-TSONMR affords the sensitivity and resolution advantages offered by CW-TSONMR which in combination with the modern pulse NMR methods can prove to be a useful tool for the identification and characterisation of defects in semiconductors.

Nutation spectroscopy of GaAs performed by FT-TSONMR did not reveal a line

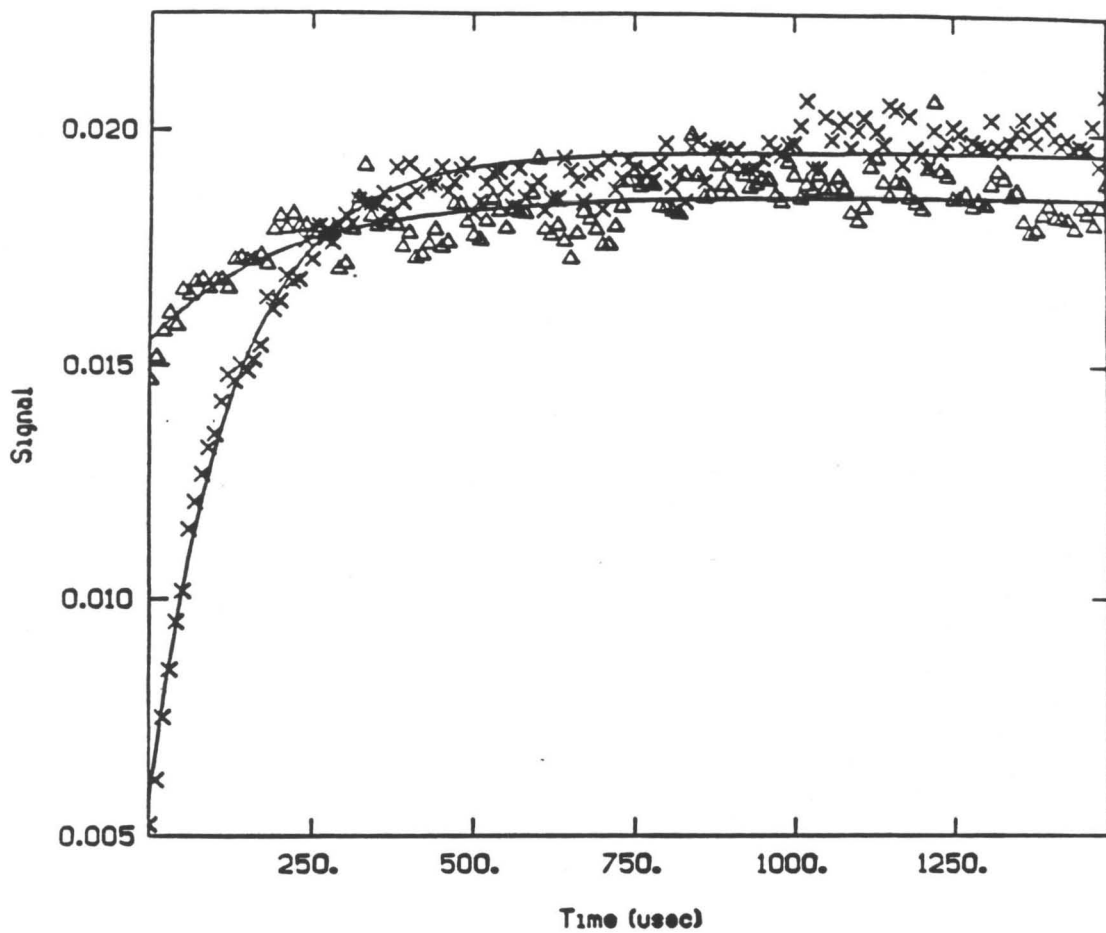


**Figure 7.10: Spin-echo amplitudes for  $^{71}\text{Ga}$ .**  $\times$ : Regular spin echo sequence and  $\Delta$ : 1 s extra ONP and 2 s spin diffusion time. Quadrupole couplings that are not refocussed account for the fast decay of the echo amplitude in the former case. The latter experiment probes sites that are further away from the ORD with smaller quadrupole couplings. Linewidth is determined by homonuclear spin-spin couplings.

at twice the nutation frequency in this sample. This implies that the contribution to the signal from the first few atomic shells is too small relative to the noise. The NMR spectrum determined by FT-TSONMR revealed a different line-width from that measured earlier in CW-TSONMR experiments. The reason for the difference in the line-widths measured in the FT and CW experiments was investigated in detail and determined to be due to the different sites that are probed by the two methods. While the FT method is relatively more sensitive to nuclei close to the optically relevant defect the CW method is dominated by the more abundant spins further away from such defects. Experiments also revealed that spin diffusion contributes to the transfer of nuclear polarisation from the nuclei close to the optically relevant defect to those in the bulk.

Experiments are underway in this laboratory to extend the technique to liquid-helium temperatures. The applicability of these techniques to the study of semiconductor heterostructures and epitaxial layers are also being investigated. NMR pulse techniques, similar to those outlined in Chapter 6, for the quantitative characterisation of defect structure is another avenue for research that is being pursued.

## 7.6 References

- [1] A. Abragam, M. Goldman, Rep. Prog. Phys., **41**, 395 (1978)
- [2] D. Stehlik, in *Excited States*, Vol. 3, ed. E. C. Lim (1977)
- [3] A. Abragam, *Principles of Nuclear Magnetism*, (Clarendon: Oxford University Press, 1961)
- [4] D. M. Hoffman, B. K. Meyer, F. Lohse, J. -M. Spaeth, Phys. Rev. Lett., **53**, 1187 (1984)
- [5] N. B. Manson, X. F. He, P. T. H. Fisk, Opt. Lett., **15**, 1094 (1990)
- [6] S. K. Buratto, N. D. Kurur, D. N. Shykind, D. P. Weitekamp, Bull. Am. Phys. Soc., **37**, 253 (1992)
- [7] S. K. Buratto, D. N. Shykind, D. P. Weitekamp, Phys. Rev. B, **44**, 9035 (1991)
- [8] M. I. D'yakanov, V. I. Perel, Zh. Eksp. Teor. Fiz., **60**, 1954 (1971) [Sov. Phys. JETP, **33**, 1053 (1971)]
- [9] M. I. D'yakanov, V. I. Perel, Zh. Eksp. Teor. Fiz., **63**, 1883 (1972) [Sov. Phys. JETP, **36**, 995 (1973)]
- [10] M. I. D'yakanov, V. I. Perel, Zh. Eksp. Teor. Fiz., **65**, 362 (1973) [Sov. Phys. JETP, **38**, 177 (1974)]
- [11] Reviews of this field can be found in *Optical Orientation*, eds. F. Meier, B. P. Zakharchenya (Amsterdam: North-Holland, 1984)
- [12] M. I. D'yakanov, V. I. Perel, V. L. Berkovits, V. I. Safarov, Zh. Eksp. Teor. Fiz., **67**, 1912 (1974) [Sov. Phys. JETP, **40**, 950 (1975)]
- [13] D. Paget, G. Lampel, B. Sapoval, V. I. Safarov, Phys. Rev. B, **15**, 5870 (1977)

- [14] A. I. Ekimov V. I. Safarov, ZhETF Pis. Red., **15**, 453 (1972) [Sov. Phys. JETP Lett., **15**, 319 (1972)]
- [15] V. L. Berkovits, A. I. Ekimov, V. I. Safarov, Zh. Eksp. Teor. Fiz., **65**, 346 (1973) [Sov. Phys. JETP, **38**, 169 (1974)]
- [16] D. Paget, Phys. Rev. B, **24**, 3776 (1981)
- [17] G. P. Flinn, R. T. Harley, M. J. Snelling, A. C. Tropper, T. M. Kerr, Semicond. Sci. Technol., **5**, 533 (1990)
- [18] M. Krapf, C. Denninger, H. Pascher, G. Weimann, W. Schlapp, Solid State Comm., **78**, 459 (1991)
- [19] C. R. Bowers, S. K. Buratto, P. J. Carson, H. M. Cho, J. Y. Hwang, L. J. Mueller, P. J. Pizarro, D. N. Shykind, D. P. Weitekamp, SPIE Proc. **1435**, 36 (1991)
- [20] V. K. Kalevich, V. D. Kul'kov, I. A. Merkulov, V. G. Fleisher, Fiz. Tverd. Tela., **24**, 2094 (1982) [Sov. Phys. Solid State, **24**, 1195 (1982)]
- [21] V. K. Kalevich, V. D. Kul'kov, V. G. Fleisher, Pisma Zh. Eksp. Teor. Fiz., **35**, 17 (1982) [JETP Lett., **35**, 20 (1982)]
- [22] S. K. Buratto, Ph. D. Thesis, California Institute of Technology, Pasadena (To be Published)
- [23] H. C. Torrey, Phys. Rev., **76**, 1059 (1949)
- [24] C. S. Yannoni, R. D. Kendrick, J. Chem. Phys., **74**, 747 (1981)
- [25] J. Y. Hwang, H. M. Cho, D. P. Weitekamp (Manuscript in Preparation)
- [26] A. Samoson, E. Lippmaa, Chem. Phys. Lett., **100**, 205 (1983)
- [27] F. Bloch, A. Siegert, Phys. Rev., **57**, 522 (1940)

[28] E. L. Hahn, Phys. Rev., **80**, 580 (1950)

[29] D. Paget, Phys. Rev. B, **25**, 4444 (1982)

## Appendix A

# Second-Order Effects in Electron Nuclear Double Resonance

In electron nuclear double resonance second-order effects lead to more lines or different frequencies than predicted by first-order perturbation theory. This may be viewed as a result of quantisation of the nuclei about the local hyperfine field of the electrons rather than solely the applied magnetic field. These effects have been known for some time and are usually analysed using standard higher order time-independent perturbation theory. One of the disadvantages of such perturbation theories is that an effective operator form for the Hamiltonian causing the splitting to a certain order does not directly result. One exception is a calculation performed by Feuchtwang[1] using a procedure outlined by Pryce.[2] A method prevalent in NMR for treating time-dependent problems, called coherent averaging theory, provides an attractive alternative way of arriving at effective time-independent Hamiltonians in such cases. This is because the result is obtained in the same rotating frame that is necessary to remove the time dependence at the Larmor carrier frequencies of the ENDOR experiment. In this appendix coherent averaging theory is used to obtain operator expressions for the second-order splitting in ENDOR. The calculations reported here are conceptually similar to the calculation of the Bloch-Siegert shifts[3, 4] by this theory, a single spin effect. Here the results are three spin effects. The calculations are straightforward, but lengthy and only the outline of the method is presented here. The significant result is that pseudo dipolar interactions are predicted

to occur between nuclei even when they are inequivalent, in contrast to the generally accepted claim[1] that these are seen only between equivalent spins.

### A.1 Essentials of Coherent Averaging Theory

The calculation of time-dependent expectation values depends on a knowledge of the propagator which takes the quantum state (or the operators in the Heisenberg picture) forward in time:

$$|a(t)\rangle = U(t, 0) |a(0)\rangle \quad (\text{A.1})$$

From the time-dependent Schrödinger equation one finds that  $U$  obeys

$$\frac{\partial}{\partial t} U = \lambda U; \quad \lambda = -\frac{i}{\hbar}. \quad (\text{A.2})$$

The usual time-dependent perturbation theory expresses

$$U = 1 + \lambda \int_0^t \mathcal{H}(t') dt' + \lambda^2 \int_0^t dt' \int_0^{t'} \mathcal{H}(t') \mathcal{H}(t'') + \dots \quad (\text{A.3})$$

where the  $\mathcal{H}$  could show explicit time-dependence. The principle of coherent averaging theory is to instead determine an average time-independent Hamiltonian that could cause the same transformation of  $|a(0)\rangle \rightarrow |a(t)\rangle$ . If such an average Hamiltonian exists, the form of the propagator  $U$  can be written as

$$U = \exp(\lambda \overline{\mathcal{H}} t). \quad (\text{A.4})$$

Perturbatively expanding of  $\overline{\mathcal{H}}$

$$\overline{\mathcal{H}} = \overline{\mathcal{H}}^{(0)} + \lambda \overline{\mathcal{H}}^{(1)} + \lambda^2 \overline{\mathcal{H}}^{(2)} + \dots \quad (\text{A.5})$$

and expanding  $U$  in equation A.4 in powers of  $\lambda$  followed by a comparison with the  $U$  of equation A.3 provides the following expressions[3]

$$\overline{\mathcal{H}}^{(0)} = \frac{1}{t} \int_0^t \mathcal{H}(t') dt' \quad (\text{A.6})$$

$$\overline{\mathcal{H}}^{(1)} = -\frac{i}{2t\hbar} \int_0^t dt' \int_0^{t'} [\mathcal{H}(t'), \mathcal{H}(t'')] dt'' \quad (\text{A.7})$$

Thus far this procedure is only an alternative form of perturbation theory. If however  $\mathcal{H}(t)$  is periodic and  $t$  is chosen to be its period,  $t_c$ , then the average Hamiltonian computed for one period suffices to describe the time development of the system for long time. The name coherent averaging arises from the above requirement that the system be observed coherently with the periodic forces of  $\mathcal{H}(t)$ . It should be noted that two powers of the Hamiltonian appear in the first order correction to the average Hamiltonian. In perturbation theory, on the other hand, it is the second order correction that contains two powers of the Hamiltonian. In this appendix the first order correction to the average Hamiltonian is hence calculated since a second order effect in perturbation theory is required.

## A.2 Outline of the Calculation

The system considered consists of two spin 1/2 nuclei, 1 and 2, with the same Larmor frequency interacting with an electron through the hyperfine coupling. The Hamiltonian for this system is

$$\mathcal{H} = \omega_e S_z + \omega_n(I_{z1} + I_{z2}) + \mathbf{I}_1 \cdot \mathcal{A}_1 \cdot \mathbf{S} + \mathbf{I}_2 \cdot \mathcal{A}_2 \cdot \mathbf{S}. \quad (\text{A.8})$$

There are 9 bilinear terms (of the form  $a_{pq}I_p S_q$ ) from each hyperfine coupling term making a total of 18. This is a generalisation of the case considered previously[1] where  $\mathcal{A}_1 = \mathcal{A}_2$  was assumed.

In coherent averaging theory the first step is usually to transform into a frame that removes the time dependence. In this case there is no time dependence and by transforming into a rotating frame one introduces time dependence to the Hamiltonian. A doubly resonant rotating frame given by

$$\mathcal{T} = \exp(-i\omega_e S_z t) \exp(-i\omega_n(I_{z1} + I_{z2})t) \quad (\text{A.9})$$

is employed. This transformation would be needed in any case to treat the magnetic

dipole irradiation terms, so the present procedure is an alternative to doing perturbation theory in the laboratory frame and then transforming the result to the rotating frame. A transformation into this frame removes the Zeeman terms in the Hamiltonian and introduces a time dependence into the hyperfine terms. For example, the bilinear term  $I_{1x}S_y$  is transformed into

$$\begin{aligned} \mathcal{T}I_{1x}S_y\mathcal{T}^{-1} &= (I_{1x}\cos(\omega_n t) + I_{1y}\sin(\omega_n t)) \\ &\times (S_y\cos(\omega_e t) - S_x\sin(\omega_e t)). \end{aligned} \quad (\text{A.10})$$

Each bilinear term (except the ones that involve only  $z$ ) on transformation to this doubly rotating frame provides four time dependent terms rotating at some combination of the frequencies  $\omega_e$ ,  $\omega_n$ ,  $(\omega_e \pm \omega_n)$ .

The next step in the calculation of the first order correction of the average Hamiltonian involves calculating the commutators of the time-dependent bilinear operators at two different times appearing in the integrand of equation A.7. This procedure is straightforward, but laborious. Double integration of these expressions then provides the first order correction to the Hamiltonian. There is one subtlety involved in picking the cycle times of the two rotating frames and which Haeberlen[3] discusses at great length. The key is to pick the cycle times such that they satisfy the relationship

$$\frac{m}{\omega_e} = \frac{n}{\omega_n}.$$

The last two operations, evaluation of the commutators and double integration, were performed on a MICROVAX using the symbolic manipulation program SMP.

Finally (after many pages of algebra) it can be shown that the first order correction to the average Hamiltonian is

$$\begin{aligned} \overline{\mathcal{H}}^{(1)} &= S_z\alpha + S_y\beta + S_x\gamma \\ &+ I_{z1}\delta_1 + I_{y1}\epsilon_1 + I_{x1}\zeta_1 \end{aligned}$$

$$\begin{aligned}
& +I_{z2}\delta_2 + I_{y2}\epsilon_2 + I_{x2}\zeta_2 \\
& +S_z[I_{z1}I_{z2}\eta + (I_{x1}I_{x2} + I_{y1}I_{y2})\theta] \\
& +S_z[I_{x1}I_{y2} - I_{y1}I_{x2}]\iota \\
& +S_yI_{z1}I_{z2}\kappa \\
& +S_xI_{z1}I_{z2}\lambda \\
& +S_y[I_{z1}I_{x2}\mu + I_{z1}I_{y2}\nu + I_{x1}I_{z2}\xi + I_{y1}I_{z2}\omicron] \\
& +S_x[I_{z1}I_{x2}\pi + I_{z1}I_{y2}\rho + I_{x1}I_{z2}\sigma + I_{y1}I_{z2}\tau]
\end{aligned} \tag{A.11}$$

where the coefficients multiplying the operators are given by

$$\begin{aligned}
\alpha &= \sum_{i=1}^2 \frac{1}{16(\omega_e - \omega_n)} [(a_{ixx} - a_{iyy})^2 + (a_{ixy} + a_{iyx})^2] \\
&+ \sum_{i=1}^2 \frac{1}{16(\omega_e + \omega_n)} [(a_{ixx} + a_{iyy})^2 + (a_{ixy} - a_{iyx})^2] \\
&+ \sum_{i=1}^2 \frac{1}{8\omega_e} (a_{izx}^2 + a_{izy}^2) \\
\beta &= \frac{1}{4\omega_e} \sum_{i=1}^2 a_{izy} a_{izz} \\
\gamma &= \frac{1}{4\omega_e} \sum_{i=1}^2 a_{izx} a_{izz} \\
\delta_i &= \frac{1}{16(\omega_e - \omega_n)} [(a_{ixx} - a_{iyy})^2 + (a_{ixy} + a_{iyx})^2] \\
&- \frac{1}{16(\omega_e + \omega_n)} [(a_{ixx} + a_{iyy})^2 + (a_{ixy} - a_{iyx})^2] \\
&- \frac{1}{8\omega_n} (a_{izx}^2 + a_{izy}^2) \\
\epsilon_i &= -\frac{1}{4\omega_n} a_{iyz} a_{izz} \\
\zeta_i &= -\frac{1}{4\omega_n} a_{ixz} a_{izz} \\
\eta &= \frac{1}{\omega_e} (a_{1zx} a_{2zx} + a_{1zy} a_{2zy}) \\
\theta &= \frac{1}{(\omega_e - \omega_n)} [(a_{1xx} - a_{1yy})(a_{2xx} - a_{2yy}) + (a_{1xy} + a_{1yx})(a_{2xy} + a_{2yx})] \\
&+ \frac{1}{(\omega_e + \omega_n)} [(a_{1xx} + a_{1yy})(a_{2xx} + a_{2yy}) + (a_{1xy} - a_{1yx})(a_{2xy} - a_{2yx})]
\end{aligned}$$

$$\begin{aligned}
\iota &= \frac{1}{(\omega_e - \omega_n)} [(a_{1xx} - a_{1yy})(a_{2xy} + a_{2yx}) - (a_{1xy} + a_{1yx})(a_{2xx} - a_{2yy})] \\
&\quad + \frac{1}{(\omega_e + \omega_n)} [-(a_{1xx} + a_{1yy})(a_{2xy} - a_{2yx}) + (a_{1xy} - a_{1yx})(a_{2xx} + a_{2yy})] \\
\kappa &= \frac{1}{\omega_e} (a_{1zy}a_{2zz} + a_{1zz}a_{2zy}) \\
\lambda &= \frac{1}{\omega_e} (a_{1zx}a_{2zz} + a_{1zz}a_{2zx}) \\
\mu &= \frac{1}{2(\omega_e - \omega_n)} (a_{1zz}a_{2xy} + a_{1zz}a_{2yx}) \\
&\quad + \frac{1}{2(\omega_e + \omega_n)} (a_{1zz}a_{2xy} - a_{1zz}a_{2yx}) \\
\nu &= \frac{1}{2(\omega_e - \omega_n)} (-a_{1zz}a_{2xx} + a_{1zz}a_{2yy}) \\
&\quad + \frac{1}{2(\omega_e + \omega_n)} (a_{1zz}a_{2xx} + a_{1zz}a_{2yy}) \\
\xi &= \frac{1}{2(\omega_e - \omega_n)} (a_{1xy}a_{2zz} + a_{1yx}a_{2zz}) \\
&\quad + \frac{1}{2(\omega_e + \omega_n)} (a_{1xy}a_{2zz} - a_{1yx}a_{2zz}) \\
o &= \frac{1}{2(\omega_e - \omega_n)} (-a_{1xx}a_{2zz} + a_{1yy}a_{2zz}) \\
&\quad + \frac{1}{2(\omega_e + \omega_n)} (a_{1xx}a_{2zz} + a_{1yy}a_{2zz}) \\
\pi &= \frac{1}{2(\omega_e - \omega_n)} (a_{1zz}a_{2xx} - a_{1zz}a_{2yy}) \\
&\quad + \frac{1}{2(\omega_e + \omega_n)} (a_{1zz}a_{2xx} + a_{1zz}a_{2yy}) \\
\rho &= \frac{1}{2(\omega_e - \omega_n)} (a_{1zz}a_{2xy} + a_{1zz}a_{2yx}) \\
&\quad + \frac{1}{2(\omega_e + \omega_n)} (-a_{1zz}a_{2xy} + a_{1zz}a_{2yx}) \\
\sigma &= \frac{1}{2(\omega_e - \omega_n)} (a_{1xx}a_{2zz} - a_{1yy}a_{2zz}) \\
&\quad + \frac{1}{2(\omega_e + \omega_n)} (a_{1xx}a_{2zz} + a_{1yy}a_{2zz}) \\
\tau &= \frac{1}{2(\omega_e - \omega_n)} (a_{1xy}a_{2zz} + a_{1yx}a_{2zz}) \\
&\quad + \frac{1}{2(\omega_e + \omega_n)} (-a_{1xy}a_{2zz} + a_{1yx}a_{2zz})
\end{aligned}$$

A number of terms in the Hamiltonian (those that involve operators like  $I_x$ ,  $I_y$ ,  $S_x$ ,  $S_y$ , and trilinear operators of the form  $I_{z1}I_{x2}S_y$ ) arise as a result of picking the lower limit

in the double integration to be zero. This can be mathematically seen by considering an integral that leads to such terms

$$\int_{\chi}^{\chi+t_c} dt'' \int_{\chi}^{t''} \sin(at'') dt' = \cos(a\chi).$$

If  $\chi$  is chosen to be zero, as was done in deriving the correction term given above, then this term is finite and does not oscillate. However, there is no experimental synchronisation that gives the time origin a special significance, so the observable terms are only those which survive averaging over  $\chi$ . A physical picture of this phenomenon with regard to Bloch-Siegert shifts is discussed by Haeberlen.[3] After performing this operation the first order correction to the average Hamiltonian has the form

$$\begin{aligned} \overline{\mathcal{H}}^{(1)} &= S_z \alpha + \\ &+ I_{z1} \delta_1 + I_{z1} \delta_2 + \\ &+ S_z [I_{z1} I_{z2} \eta + (I_{x1} I_{x2} + I_{y1} I_{y2}) \theta]. \end{aligned} \quad (\text{A.12})$$

In the expression for the Hamiltonian all terms except the last are similar to those seen in Bloch-Siegert shifts. The terms in equation A.12 that are bilinear in nuclear spin operators cause the splitting of the lines. The connection to a dipolar splitting is more obvious when written in a form involving irreducible tensor operators

$$I_{z1} I_{z2} = \frac{1}{3} (3I_{z1} I_{z2} - \mathbf{I}_1 \cdot \mathbf{I}_2) + \frac{1}{3} \mathbf{I}_1 \cdot \mathbf{I}_2 \quad (\text{A.13})$$

$$\begin{aligned} I_{x1} I_{x2} + I_{y1} I_{y2} &= (\mathbf{I}_1 \cdot \mathbf{I}_2 - I_{z1} I_{z2}) \\ &= \frac{1}{3} (3I_{z1} I_{z2} - \mathbf{I}_1 \cdot \mathbf{I}_2) + \frac{2}{3} \mathbf{I}_1 \cdot \mathbf{I}_2. \end{aligned} \quad (\text{A.14})$$

Thus within each electron spin manifold specified by setting  $S_z = \pm 1/2$ , there are pseudo-dipolar and pseudo-scalar couplings that add or subtract from the hyperfine terms. These terms are all of order  $a^2/\omega_e$  implying that for large hyperfine couplings they will, using the multiple-pulse methods of Chapter 6, be observable in single crystal studies even at the highest available magnetic field. It is generally believed that these terms arise only

if the two nuclei are equivalent, perhaps because this is the only case for which they had previously been derived.[1] The above analysis seems to indicate that this not the case, since the hyperfine tensor for the two spins were assumed to be different, i. e.,  $\mathcal{A}_1 \neq \mathcal{A}_2$ . In the limit that  $\mathcal{A}_1 = \mathcal{A}_2$  and  $\omega_e \pm \omega_n \approx \omega_e$  the Hamiltonian agrees with that of Feuchtwang.[1]

Because the resolution of ordinary ENDOR is rarely adequate to resolve nuclear spin-spin couplings, existing experiments apparently do not resolve the issue. In the only cases where second-order couplings of this sort have been invoked [5, 6, 7, 8] the sites have been magnetically equivalent. Heteronuclear resolution-enhanced ENDOR, as proposed in Chapter 6, would settle this issue. The sign difference between the spectra within the manifolds with opposite projection of  $S_z$  would be apparent for any bonded or nearby heteronuclear pair, since then a direct dipolar coupling or a scalar coupling with fixed sign would add to the terms of A.12 and subtract in the other.

### A.3 References

- [1] T. E. Feuchtwang, Phys. Rev., **126**, 1628 (1962)
- [2] M. H. L. Pryce, Proc. Phys. Soc. (London), **63**, 25 (1950)
- [3] U. Haeberlen, *High Resolution NMR in Solids: Selective Averaging*, Adv. Magn. Reson., Suppl. 1 (New York: Academic Press, 1976)
- [4] M. Mehring, *Principles of High Resolution NMR in Solids* (Berlin: Springer-Verlag, 1983)
- [5] A. Schweiger, G. Rist, Hs. H. Günthard, Chem. Phys. Lett., **31**, 48 (1975)
- [6] M. Fujimoto, C. A. McDowell, T. Takui, J. Chem. Phys., **70**, 3694 (1979)
- [7] G. Heder, J. R. Niklas, J. M. Spaeth, Phys. Stat. Solidi B, **100**, 567 (1980)
- [8] T. G. Brown, B. M. Hoffman, Mol. Phys., **39**, 1073 (1980)

## Appendix B

# Noise in the Optical NMR Instrument

## Detection Circuit

During the course of the time-domain time-sequenced optical NMR experiments discussed in Chapter 7 the noise characteristics of the detection circuit in the instrument were determined. This measurement was motivated by the need to know if quantum noise-limited detection is realisable with the present setup. The procedure employed is outlined in this appendix.

### B.1 The Equivalent Circuit

The detection system consists of an RCA C39021E avalanche photodiode (APD) back biased at 240 V. This photodiode converts the light energy into detectable electrical signal. A home-built transconductance amplifier of standard design [1] with a 1.54 k $\Omega$  resistance is used to provide enough current to drive the 50  $\Omega$  coaxial cable. This signal is amplified in a Stanford Research System (SRS) SR552 preamplifier with a gain,  $G$ , of 100 after which the signal is split and fed into two SRS lock-in amplifiers. The luminescence polarisation,  $\rho$ , is

$$\rho = \frac{I_+ - I_-}{I_+ + I_-}, \quad (\text{B.1})$$

where  $I_+$  and  $I_-$  are the number of left and right circularly polarised photons. One of the two lock-in amplifiers is locked at the frequency of the photoelastic modulator (50 kHz) and measures the numerator of equation B.1 while the other measures the denominator

by locking on to the frequency at which the exciting laser light is chopped (500 Hz).

## B.2 Noise Measurements

The noise of the above mentioned equivalent circuit was initially measured in ambient light and involves mimicking the experimental conditions exactly with the exception that the laser is shuttered off so that no luminescence reaches the detector. A lock-in time constant of 30 ms is used and 500 data points are acquired in all the measurements. Three different measurements were made to determine the noise contributions from the different components of the setup. These measurements are compiled in Table B.1. The

**Table B.1: Noise Measurements at 500 Hz**

	SR530 Noise	SR510 Noise
	(Volts/ $\sqrt{\text{Hz}}$ ) $\times 10^8$	
Preamp/lock-in	0.1213	0.1246
No detector	1.770	3.097
Total Circuit	2.738	4.038

two columns in the table represent the same measurements performed with two different lock-in amplifiers. The first experiment was with only the preamplifier + lock-in arrangement. This measurement confirmed the noise specifications for the lock-in amplifiers ( $\approx 1 \text{ nV}/\sqrt{\text{Hz}}$ ). Next, the noise of the transconductance amplifier + preamp assembly was measured (“no detector”) and finally that of the complete equivalent circuit. Not surprisingly, the noise of the equivalent circuit ( $\approx 40 \text{ nV}/\sqrt{\text{Hz}}$ ) is dominated by the noise of the transconductance amplifier ( $\approx 30 \text{ nV}/\sqrt{\text{Hz}}$ ).

Table B.2 lists the noise of the detection system in the presence of luminescence for a number of bias voltages. The bias voltage changes the gain of the APD,  $M$ , which is distinct from the gain of the preamplifier. The optical NMR experiments are typically

performed at 240V bias and the rest of the calculation reported here is for this bias voltage. The experimentally measured error standard deviation  $\sigma_\rho$  in  $\rho$  is reported in the last column of the Table B.2. In the region around 240 V bias voltage  $\sigma_\rho$  is essentially independent of the bias voltage.

**Table B.2: Signal + Noise Measurements**

Bias Voltage (Volts)	$(I_+ + I_-)$ Volts $\times 10^4$	$\sigma_\rho$ $\times 10^3$
242	3.390	1.404
240	2.437	1.379
238	1.838	1.468
235	0.1350	1.647
220	0.4788	3.878

The measured error in  $\rho$  has to be compared with the shot noise or photon quantum noise contribution at this light level. The calculation of the shot noise is straightforward and outlined below. If an observable,  $x$ , is measured as the ratio of two uncorrelated numbers  $u$  and  $v$

$$x = \frac{u}{v} \quad (\text{B.2})$$

as is the case with  $\rho$  then the variance in  $x$  is given by

$$\frac{\sigma_x^2}{x^2} = \frac{\sigma_u^2}{u^2} + \frac{\sigma_v^2}{v^2}.$$

This expression can be be rewritten as

$$\sigma_x^2 = \frac{\sigma_u^2}{v^2} + \sigma_v^2 \frac{u^2}{v^4}. \quad (\text{B.3})$$

If  $u$  is much smaller than  $v$  (implied by the small measured  $\rho$  value) the variance in the measured value of  $x$  can be approximated to be

$$\sigma_x^2 \approx \frac{\sigma_u^2}{v^2}.$$

The counting statistics follow a Poisson distribution for which the standard deviation is given by the square root of the number of counts. In this case the calculated shot noise is  $\approx 4.2 \times 10^{-5}$  (requires conversion of the signal measured in volts to number of photons). This has to be contrasted with the experimentally measured noise of  $1.38 \times 10^{-3}$  implying that the photon shot-noise contribution is insignificant.

### B.3 Calculated Noise

The measured  $\sigma_\rho$  can also be compared with the theoretical estimate of the noise of the detection device which sets an experimental lower bound on the uncertainty. This can be calculated from the device characteristics.

The noise of an avalanche photodiode,  $i_n$ , is given by [2]

$$i_n^2 = 2q[I_{ds} + (P_0 R_0 F_s + I_{db} F_d) M^2] B_w + i_{na}^2. \quad (\text{B.4})$$

The parameters in the above equation are

$I_{ds}$  = dark current of the avalanche photodiode surface

$I_{db}$  = bulk dark current

$P_0$  = photoluminescence power

$R_0$  = unity-gain responsivity of the APD

$M$  = gain of the APD

$q$  = electron charge

$B_w$  = detection bandwidth

$i_{na}$  = Johnson noise of the equivalent circuit

$F_d$  = excess noise factor of the dark current

$F_s$  = excess noise factor for the photocurrent

The parameters required in the formula are either available in the literature or can be easily calculated. The parameters in equation B.4 that require calculation were determined as follows:

1. The excess noise factor for the dark current and the photocurrent are often the same implying  $F = F_d = F_s$ . A simple formula relates this to the gain of the APD

$$F = 0.98\left(2 - \frac{1}{M}\right) + 0.02M.$$

For the bias voltage used in these measurements  $F$  is 4.9535.

2. The unity-gain responsivity is given by

$$R_0 = \frac{q\eta\lambda}{hc},$$

where  $\eta$  is the quantum efficiency of the photodiode (0.70 at the detection frequency 870 nm).

3. The photocurrent is calculated from

$$P_0 R_0 M = \text{photocurrent} = \frac{I_+ + I_-}{1.54\text{k}\Omega}.$$

For the measurements reported here the photocurrent is  $1.582 \times 10^{-7}$  A.

**Table B.3: Reference Data**

Parameter	Value	Source
$\eta$	0.70	Ref. [4]
$M$	150	Ref. [4]
$F$	4.9535	calculated
$R_0$	0.4912 A/W	calculated
$I_{ds}$	$6 \times 10^{-10}$ A	Ref. [3]
$I_{db}$	$6 \times 10^{-12}$ A	Ref. [3]
photocurrent	$1.682 \times 10^{-7}$ A	calculated

With the information presented in Table B.3 the noise equation B.4 associated with the luminescence

$$i_p^2 = 2qP_0R_0FM^2B_w$$

is found to be  $2.53 \times 10^{-22} \text{A}^2$ . Similarly the noise due to the dark current

$$i_{\text{d}}^2 = 2q(I_{\text{ds}} + I_{\text{db}}FM^2)B_{\text{w}}$$

is  $7.077 \times 10^{-24} \text{A}^2$ . The Johnson noise of the equivalent circuit  $i_{\text{na}}^2$  is

$$i_{\text{na}}^2 = \frac{4kTB_{\text{w}}}{R}, \quad (\text{B.5})$$

where  $k$  is the Boltzmann constant.  $i_{\text{na}}^2$  is determined from this expression to be  $3.58 \times 10^{-22} \text{A}^2$ .

The lower bound on the noise  $\sigma_{\rho}$  of the detection can be estimated from the theoretical estimate of the noise of the detection device through the expression

$$\sigma_{\rho}^{\text{theory}} = \frac{\sqrt{i_{\text{na}}^2 + i_{\text{p}}^2 R}}{I_{+} + I_{-}}, \quad (\text{B.6})$$

where  $R$  is the resistance of the transconductance amplifier. For the light flux involved in the present case  $\sigma_{\rho}^{\text{theory}}$  is found to be  $1.5 \times 10^{-4}$ . The experimentally measured noise in  $\rho$  (from Table B.2) is  $1.379 \times 10^{-3}$ , which is a factor of 10 bigger than that predicted by the noise equivalent power of the detection circuit and a factor of  $\approx 30$  away from achieving shot-noise detection.

This realisation has led to replacement of the transconductance amplifier so that in recent experiments the noise is within a factor of 2 of the shot-noise limit.[5]

## B.4 References

- [1] P. Horowitz, W. Hill (Cambridge: Cambridge University Press, 1989)
- [2] A. Yariv, *Optical Electronics* (New York: Holt, Rinehart, and Winston, 1985)
- [3] P. P. Webb, R. J. McIntyre, J. Conradi, *RCA Review*, **35**, 234 (1974)
- [4] RCA Solid State Detectors C309021E and C309021S Applications Notes
- [5] S. K. Buratto, Personal Communication (1992)

## Appendix C

# Simulation of Multiple Pulse NMR Experiments

Modern pulse NMR techniques have evolved considerably in the past few years. Simulation programs have played an important part in the development and understanding of new NMR methods. They often allow for easy optimisation of different parameters prior to experimentation. The method discussed in Chapter 6, for example, made use of such simulations extensively. The program that was used in those and for a number of other simulations in the Weitekamp group is discussed in this appendix. This program descends from one written in the Pines group at the University of California, Berkeley, and has evolved considerably over a number of years. Several people have contributed significantly towards the improvement and testing of this program. This writeup is motivated by a lack of documentation of the many changes that the program has undergone since arriving at Caltech. A 1982 report discusses the Berkeley version of the program.[1] The Caltech version as of 1988 was deposited with the WISCWARE program library of the University of Wisconsin.

A number of programs with wide ranging capabilities exist in the literature for the simulation of NMR experiments. The methodology used in these programs is also diverse. Some of these programs involve numerical density matrix calculations in the frequency domain,[2] while in others the computation is performed in the time domain.[3, 4, 5, 6] Recently, programs that use symbolic formula manipulation [7, 8, 9] have also become available.

## C.1 Introduction

The essence of all simulation programs is to determine the time evolution of the density matrix numerically. The dynamics of the density matrix,  $\sigma$ , are governed by the Liouville-von Neumann equation

$$\frac{d}{dt}\sigma = -i[\mathcal{H}, \sigma]. \quad (\text{C.1})$$

For time-independent Hamiltonians  $\mathcal{H}$  (the only kind that is involved in this appendix) the solution of this equation is given by a unitary transformation of the type

$$\sigma(t) = \mathcal{U}\sigma(0)\mathcal{U}^\dagger \quad (\text{C.2})$$

where  $\mathcal{U}$  has the form

$$\mathcal{U} = \exp(-i\mathcal{H}t).$$

The Hamiltonians which can be handled by the programs in question are piecewise constant in the rotating frame. If the time  $t$  can be broken up into a number of steps of lengths  $t_1, \dots, t_n$  with the Hamiltonian in each step given by  $\mathcal{H}_1, \dots, \mathcal{H}_n$  then the time evolved density matrix is

$$\sigma(t_1 + \dots + t_n) = (\mathcal{U}_n \dots \mathcal{U}_1)\sigma(0)(\mathcal{U}_1^\dagger \dots \mathcal{U}_n^\dagger) \quad (\text{C.3})$$

with  $\mathcal{U}_i$  being given by

$$\mathcal{U}_i = \exp(-i\mathcal{H}_i t_i).$$

The signal at time  $t$ ,  $S(t)$ , is obtained from the density matrix at time  $t$  by

$$S(t) = \text{Tr}(\sigma(t)I_+) \quad (\text{C.4})$$

where  $I_+ = I_x + iI_y$  is the detection operator whose expectation value corresponds to oscillating magnetisation in the plane transverse to the applied magnetic field, and  $\text{Tr}$  indicates the trace operation.

Thus the time evolution of the density matrix is an initial value problem where the initial density matrix and the Hamiltonians at each time step must be specified.

## C.2 Program Specifics

Most modern NMR experiments can be viewed as containing four time periods: preparation, evolution, mixing and detection. The evolution period is the  $t_1$  dimension in a two-dimensional (2D) experiment while the detection period forms the second or  $t_2$  dimension. In keeping with the nomenclature of coherent averaging theory the various periods are subdivided into cycles in the present program. The signal, with dissipation effects ignored, is stroboscopically observed at the end of each detection cycle. Fourier transformation of the time-domain signal either in one or two dimensions, as the case may be, provides the familiar NMR spectrum.

Each of the cycles of the four time periods mentioned above may be repeated any number of times. The repetitions may be phase shifted by  $\frac{2\pi}{n}$ . Each cycle is in turn subdivided into a number of time steps (the program presently has an upper limit of  $\approx 2000$ ). During each time step the Hamiltonian is time independent and has the general form

$$\mathcal{H}_{\text{total}} = \mathcal{H}_{\text{system}} + \mathcal{H}_{\text{rf}}. \quad (\text{C.5})$$

The time independence of the rf Hamiltonian is achieved by working in a frame rotating at the radiofrequency about the applied magnetic field direction. The latter term in the expression for the total Hamiltonian is only present when an rf pulse is applied. A time step where the rf is present is called a pulse while that without it is called a delay. The rf pulses are restricted to be square, but can have arbitrary strength (input as the pulse length and pulse angle) and phase. The rf Hamiltonian has the form

$$\mathcal{H}_{\text{rf}} = \gamma B_1 I_\phi.$$

The value  $\gamma B_1$  dictates the strength of the pulse while the phase is governed by the  $\phi$  term.

The system Hamiltonian is made up of three parts

$$\mathcal{H}_{\text{system}} = \mathcal{H}_z + \mathcal{H}_J + \mathcal{H}_D \quad (\text{C.6})$$

with  $\mathcal{H}_z$ ,  $\mathcal{H}_J$ , and  $\mathcal{H}_D$  being the Zeeman, scalar coupling, and dipolar Hamiltonians in their usual forms. For heteronuclear experiments only the the scalar and dipolar coupling Hamiltonian have the form

$$\mathcal{H}_J = JI_zS_z \quad (\text{C.7})$$

$$\mathcal{H}_D = DI_zS_z. \quad (\text{C.8})$$

The system Hamiltonian does not contain a quadupolar coupling term since the program cannot at present treat spin  $> 1/2$ . A maximum of 5 spins can be treated by the program. The spins may optionally be divided into two groups  $I$  and  $S$  in which case separate pulse strengths at two Larmor frequencies can be specified. Such calculations are done in the doubly-rotating frame approximation.

The program supports a number of options for the initial density matrix. Within the high-field approximation, the traceless part of the equilibrium density matrix has the form

$$\rho(0) = bI_z, \quad (\text{C.9})$$

where  $b$  depends on the Larmor frequency and the temperature. The initial condition most often used is  $I_z$ , i. e.  $b = 1$ . More exotic initial conditions where all the population is in the lowest state or with an N-quantum operator are also provided for. Initial conditions of particular interest to the Weitekamp group, for example that created in a PASADENA experiment, can also be handled. An option useful for the quantitative determination of the line intensities also exists. In this case, the constant  $b$  is evaluated from a knowledge of the temperature and the Larmor frequency.

Two different kinds of bases are used in the program. The first is the simple-product basis. This basis is useful in determining the matrix elements of the different spin opera-

tors. Another advantage of the simple-product basis is that there are no matrix elements between states in different  $m_z$  manifolds. This implies that the Hamiltonian block diagonalises with each  $m_z$  manifold forming a block. The matrices that are involved are often sparse and by using the block factoring feature significant reduction in the storage is possible. Some of the programs in the literature do not use block factoring but use sparse-matrix routines for the computations. The other basis that is often used is the eigenbasis of the Hamiltonian. This is especially useful for time evolution steps since in this basis the propagator has the form

$$\mathcal{U}_{l,m}(t_i) = \exp(-i\omega_l t_i)\delta_{l,m}, \quad (\text{C.10})$$

where  $\omega_l$  is an eigenvalue of the Hamiltonian in time step  $i$ . This basis is used for all the time evolution, implying that matrices have to be transformed from one basis to another. This involves matrix multiplications and these are probably the more time consuming steps in the program. Most modern NMR experiments involve pulse sequences with a number of delays where the density matrix evolves under the action of the system Hamiltonian. Typically, the system Hamiltonian is not time dependent, which implies that a significant time saving is achievable if repetitive diagonalisation of the system Hamiltonian is avoided. A diagonalised copy of the system Hamiltonian is stored for this reason.

The signal is calculated at the end of every cycle in the simple-product basis. This requires that the density matrix be transformed from the eigenbasis to the simple-product basis for detection. For the case of detection during free evolution or constant tickling, this repeated transformation from one basis to the other is one of the more inefficient steps. For detection in the windows of multiple-pulse sequences, such transformation is inevitable. The signal is output in one of two forms. The more common procedure is to store the signal in a file that forms the input to some other data analysis program. A significant reduction in storage is achieved by using an unformatted binary file to store

the data. In the case of a 2D experiment each  $t_1$  point produces a separate file. A second output option is to display the density matrix form of the signal either in the simple-product or in the eigenbasis of the system Hamiltonian.

The input to the simulation program requires a number of parameters regarding the system Hamiltonian, pulse sequence, initial conditions, output format etc. These parameters are contained in a file that is created by a user friendly interactive setup program. The setup program is called SETCOMP.FOR, while the simulation program is called SIMCOMP.FOR.

### C.3 References

- [1] J. B. Murdoch, Ph. D. Thesis, University of California, Berkeley (1982) (published as Lawrence Berkeley Report LBL-15254)
- [2] H. Widmer, K. Wüthrich, *J. Magn. Reson.*, **70**, 270 (1986)
- [3] L. E. Kay, J. N. Scarsdale, D. R. Hare, J. H. Prestegard, *J. Magn. Reson.*, **68**, 515 (1986)
- [4] D. Piveteau, M. A. Delsuc, J. -J. Lallemand, *J. Magn. Reson.*, **70**, 29 (1986)
- [5] W. Studer, *J. Magn. Reson.*, **77**, 424 (1988)
- [6] S. A. Smith, T. Levante, B. H. Meier, R. R. Ernst, Poster Abstracts 31<sup>st</sup> Experimental Nuclear Magnetic Resonance Spectroscopy Conference (1991)
- [7] J. M. Bernassau, F. Boissiere, J. F. Thomas, *Comput. Chem.*, **10**, 253 (1986)
- [8] T. T. Nakashima, R. E. D. McClung, *J. Magn. Reson.*, **70**, 187 (1986)
- [9] J. W. Shriver, *J. Magn. Reson.*, **94**, 612 (1991)

## Appendix D

# Solution of One-Dimensional Schrödinger Equations

In Part I of this dissertation there arose the need to solve for the eigenvalues, and in some cases the eigenfunctions, of various one-dimensional Schrödinger equations. This appendix discusses the algorithm that was employed for this purpose.

The one-dimensional Schrödinger equation for a particle of mass  $m$  has the familiar form

$$\left(-\frac{\hbar^2}{2m} \frac{d^2}{dx^2} + V(x)\right) \Psi(x) = E\Psi(x), \quad (\text{D.1})$$

where the first term is the kinetic energy, and  $V(x)$  is the potential energy. The goal is to determine the eigenfunctions  $\Psi(x)$  and the eigenvalues  $E$ . The numerical methods for obtaining the solutions of the 1D Schrödinger equation can be broadly classified into two types; numerical integration (shooting methods)[1, 2, 3, 4] or matrix methods.[5, 6, 7, 8, 9, 10] The algorithm used in this thesis falls into the matrix method category.

The general methodology for matrix solutions of the Schrödinger equation involves two steps. In the first step, the Hamiltonian,  $\mathcal{H}$ , is expressed in a convenient basis,  $\{\phi_j\}$ . This assumes that the eigenfunctions of the Hamiltonian,  $\Psi_i$ , are linear combinations of the basis functions

$$\Psi_i = \sum_{j=1}^N c_j \phi_j. \quad (\text{D.2})$$

Here  $N$  is the dimension of the basis. In the second step, the Hamiltonian in the  $\phi_j$  basis

is diagonalised by a transformation of the type

$$\mathcal{H}_{\text{diag}} = \mathcal{U}\mathcal{H}\mathcal{U}^\dagger. \quad (\text{D.3})$$

The diagonal elements of  $\mathcal{H}_{\text{diag}}$  provide the eigenvalues of the Schrödinger equation while the eigenfunctions are obtained from the transformation matrix  $\mathcal{U}$ .

### D.1 Algorithm for the Linear Case

The algorithm used[5] can be broken up into the following steps:

- Step 1. Determine the matrix elements of the operators  $\hat{x}$  and  $\hat{p}^2$  in the basis chosen.
- Step 2. Determine and store both the eigenvalues of  $\hat{x}$  and the transformation matrix,  $\mathcal{U}$ , that performs the diagonalisation of  $\hat{x}$ .
- Step 3. Transform  $\hat{p}^2$  into the  $x$  basis (the basis in which  $\hat{x}$  is diagonal).
- Step 4. Determine the matrix elements of the Hamiltonian in the  $x$  basis:

$$\frac{1}{2m}\mathcal{P}_x^2 + V(x_i)$$

- Step 5. Diagonalise the Hamiltonian from step 4.

The above algorithm implemented for a harmonic oscillator basis was used in all the calculations for linear potentials reported in Part I of this thesis. The reason for the choice of this basis for the calculation was primarily that the potentials were perturbed harmonic oscillators. The algorithm is outlined here for this choice of basis but can be extended to other cases.

The Hamiltonian for a harmonic oscillator is

$$\mathcal{H}_{\text{ho}} = \frac{\hat{p}^2}{2m} + \frac{1}{2}k\hat{x}^2 \quad (\text{D.4})$$

with eigenfunctions of the form

$$|n\rangle = \sqrt{\frac{\alpha}{\sqrt{\pi}2^n n!}} H_n(\alpha x) \exp(-\alpha^2 x^2/2),$$

where  $H_n$  are Hermite polynomials. The position and the momentum operator in terms of the annihilation,  $\hat{a}$ , and creation,  $\hat{a}^\dagger$ , operators are

$$\hat{x} = \sqrt{\frac{\hbar}{2m\omega}}(\hat{a} + \hat{a}^\dagger) \quad (\text{D.5})$$

$$\hat{p} = i\sqrt{\frac{m\hbar\omega}{2}}(\hat{a} - \hat{a}^\dagger). \quad (\text{D.6})$$

Using the fact that

$$\hat{a} |n\rangle = \sqrt{n} |n-1\rangle \quad (\text{D.7})$$

$$\hat{a}^\dagger |n\rangle = \sqrt{n+1} |n+1\rangle \quad (\text{D.8})$$

the matrix form of the  $\hat{x}$  operator and  $\hat{p}$  operator in the harmonic oscillator basis can be readily determined. This forms the first step of the algorithm. The eigenvalues of  $\hat{x}$  are determined by a similarity transform

$$x_{\text{diag}} = \mathcal{U}\hat{x}\mathcal{U}^{-1}. \quad (\text{D.9})$$

In step 3, the momentum operator is transformed to the eigenbasis of the  $\hat{x}$  by application of the same transform that diagonalises  $\hat{x}$ . In the penultimate step the Hamiltonian is computed in the  $x$  basis as

$$\mathcal{H} = \frac{1}{2m}\mathcal{U}\hat{p}^2\mathcal{U}^{-1} + V(\mathcal{U}\hat{x}\mathcal{U}^{-1}). \quad (\text{D.10})$$

In the eigenbasis of  $\hat{x}$  a potential  $V(x)$  has only diagonal terms. The potential is evaluated at the eigenvalues of  $\hat{x}$ . Diagonalisation of  $\mathcal{H}$  provides the eigenvalues of the Schrödinger equation.

Considerable simplification in the algorithm is possible for symmetric potentials. The harmonic oscillator states have either odd or even symmetry depending on the vibrational quantum number. This implies that for symmetric potentials two separate calculations can be performed for the states of opposite symmetry reducing both the computer memory requirement as well as the time involved. One other practical point that is noteworthy

is that steps 1 through 3 need only be done once if the results are stored after the first run. This is due to the fact that all matrix elements of the position operator depend on the oscillator parameter through the same multiplicative factor. The matrix elements of the momentum operator also show a similar behaviour. This implies that the dependence of the matrix elements of the position and momentum operator on the oscillator parameter can be introduced before step 4. of the oscillator.

The only matter left to discuss is the choice of the oscillator parameter  $\alpha$ . As was mentioned earlier, the potentials were all perturbed oscillators. Hence, in almost all cases the oscillator parameter used was that of the unperturbed oscillator centred at  $x = 0$ . For the double well anharmonic oscillator, the oscillator parameter was determined by a method suggested by Quick and Miller.[11] In this method the oscillator parameter for the odd ( $\alpha_o$ ) and even ( $\alpha_e$ ) states are different and are obtained by separately minimising the manifold energies of the first  $N$  odd and even parity states. Mathematically this can be represented as

$$\frac{\partial}{\partial(\alpha_o^2)} \left( \sum_1^N \langle 2n-1 | \mathcal{H} | 2n-1 \rangle \right) = 0 \quad (\text{D.11})$$

$$\frac{\partial}{\partial(\alpha_e^2)} \left( \sum_0^N \langle 2n | \mathcal{H} | 2n \rangle \right) = 0. \quad (\text{D.12})$$

When one requires eigenvalues of a number of low lying states this choice is more democratic than one which minimises the energy of one state. For large barrier heights a more appropriate basis is two harmonic oscillators centred at the two wells. This method, however, would require the calculation of overlap matrix elements between the functions in the two wells. Rather than use this approach a brute force method was employed here. This involves increasing the dimension of the basis used until the energy of the lowest few eigenstates were constant to better than 1 part in  $10^{15}$ . This required up to 200 basis sets of each parity. For some data sets of  $J(T)$ , convergence was not reached, and these were set aside as outside the present computing ability (MICROVAX 2000). This is not

of much physical interest as the trends in  $J(T)$  are very similar to the curves successfully fit in Chapter 3.

The program for the determination of the matrix elements of the position and momentum operator is called HEGMATSET.FOR, while that which determines the eigenvalues is H3\_DW.FOR.

## D.2 Periodic Potential

The Mathieu equation (see Chapter 3) was also solved by a matrix method.[6] The rigid-rotor states  $\exp(im\phi)$  were used as basis states. The Hamiltonian in this basis has the form

$$\langle n | \mathcal{H} | m \rangle = -\frac{n^2}{2I} \delta_{n,m} + \frac{V_0}{2} \delta_{n,m\pm 2}, \quad (\text{D.13})$$

where  $I$  is the moment of inertia of the system. Diagonalisation of this matrix provides the eigenvalues.

In this case, over and above the factorisation achieved by separating the odd and even states, another simplification is possible by choosing even and odd functions of  $\phi$  as the basis sets, but this was not employed.

The program for the solution of the Mathieu equation is called H3\_RTR.FOR.

Diagonalisations form an important part of both these algorithms. All diagonalisations in both programs were performed with the well-tested EISPACK routines.[12]

### D.3 References

- [1] J. W. Cooley, *Math. Comp.*, **15**, 363 (1961)
- [2] B. R. Johnson, *J. Chem. Phys.*, **67**, 4086 (1977)
- [3] B. R. Johnson, *J. Chem. Phys.*, **69**, 4678 (1978)
- [4] B. Lindberg, *J. Chem. Phys.*, **88**, 3805 (1988)
- [5] D. O. Harris, G. G. Engerholm and W. D. Gwinn, *J. Chem. Phys.*, **43**, 1515 (1965)
- [6] C. S. Ewig, D. O. Harris, *J. Comp. Phys.*, **11**, 606 (1973)
- [7] D. G. Truhlar, *J. Comp. Phys.*, **10**, 123 (1972)
- [8] V. Fach, G. V. Berghe, *Comput. Phys. Commun.*, **39**, 187 (1986)
- [9] Z. Bačić, *J. C. Light, Annu. Rev. Phys. Chem.*, **40**, 469 (1989)
- [10] G. C. Groenenboom, H. M. Buck, *J. Chem. Phys.*, **92**, 4374 (1990)
- [11] R. M. Quick, H. G. Miller, *Phys. Rev. D*, **31**, 2682 (1985)
- [12] B. T. Smith, J. M. Boyle, J. J. Dongarra, B. S. Garbow, Y. Ikebe, V. C. Klema, C. B. Moler, *Matrix Eigensystem Routines—EISPACK Guide*, Lectures in Computer Science 6, ed. G. Goos, J. Hartmanis (Berlin: Springer-Verlag, 1976)